UNIVERSITA' DEGLI STUDI DI VERONA

DEPARTMENT OF

NEUROSCIENCES, BIOMEDICINE AND MOVIMENT SCIENCES

PHD SCHOOL

DIAGNOSTICS AND PUBLIC HEALTH

DOCTORAL PROGRAM IN

NANOSCIENCE AND ADVANCED TECHNOLOGIES

Cycle / year: XXXVI / 2020

THE REGENERATIVE POTENTIAL OF STROMAL VASCULAR FRACTION DELIVERY VIA HYALURONIC ACID IN AN ISCHEMIA-REPERFUSION INJURY MODEL

S.S.D. BIO /16

Coordinator: Prof. Adolfo Speghini

Tutor: Prof. Andrea Sbarbati

PhD candidate: Dott. Anita Conti

ABSTRACT

Tissue engineering, in recent years, has shown interesting applications, particularly in regenerative medicine with the aim of improving the renewal and repair of damaged tissues. In this context, the use of stromal vascular fraction (SVF) from adipose tissue, combined with biomaterials has demonstrated remarkable potential in promoting tissue recovery. SVF, due to its multipotency and immunomodulatory properties, provides interesting evidences of high therapeutic potential. In addition, hyaluronic acid (HyA) has emerged as a versatile biomaterial renowned for its biodegradable, biocompatible, and bioactive properties.

The aim of this study was to assess the regenerative potential of SVF with an HyA in a model of muscular ischemia-reperfusion (I/R) injury. The first part of the study focused on *in vitro* and *in vivo* characterization of SVF obtained through mechanical fragmentation of adipose tissue and its with HyA. Subsequently, the regenerative potential of SVF combined with HyA was assessed in a model of skeletal muscle I/R injury. Multiparametric MRI evaluations, motor function tests, quantitative analyses, and immunohistochemical examinations demonstrated that the SVF combined with HyA treatment induced significant improvements in the experimental model. In particular, we observed a reduction of edema, a positive impact on motor function impairment, and myofibril organization compared to individual SVF or HyA treatments. Overall, the results showed that the synergistic effect of SVF and HyA could represent an efficient treatment for skeletal muscle ischemia-reperfusion injury with high translational potential for future clinical studies.

1 INTRODUCTION

1.1 ADIPOSE-DERIVED MESENCHYMAL STEM CELLS AND STROMAL VASCULAR FRACTION

Mesenchymal stem cells (MSCs) are multipotent stem cells with properties of multilineage differentiation, high proliferation potential, and self-renewal, with a secretion of paracrine factors[1, 2]. Thanks to their proprieties, MSCs have increasingly been used as a therapeutic regenerative therapy.

Different tissues can serve as a source of adult MSCs, but bone marrow (BM-MSC) and adipose tissue (AD-MSC) are the most common. Immunophenotypization and differentiation capability assay have established differences and similarities between BM-MSC and AD-MSC. Nevertheless, the significant differences in regenerative potential between BM-MSC and AD-MSC remain uncertain.

The extraction of MSCs from adipose tissue compared to bone marrow presents numerous advantages. First, it has been demonstrated that adipose tissue contains 100-1000-fold more MSCs than bone marrow[3, 4]. Additionally, the extraction procedure is less invasive, less painful, and with fewer risks of complications compared to a bone marrow harvest[5].

Stromal vascular fraction (SVF) represents a freshly isolated heterogeneous cell mixture present in the adipose tissue. It comprises smooth muscle cells, preadipocytes, endothelial cells, and several multipotent stem cell[6]. All the cell subtypes are linked together with stromal connective tissue. With all the components, the SVF contributes to the regulation of the stemness of MSCs within the perivascular niche[6, 7].

1.1.1 Differences between SVF and AD-MSC

Key differences can be identified between SVF and expanded AD-MSC, as the former encompasses the niche where AD-MSC live and maintain their stemness[7]. Firstly, the SVF has a short time preparation, unlike the stem cells

extracted from it, which may require a long expansion time. Otherwise, to obtain a large initial quantity of AD-MSCs, it would be necessary to harvest a large amount of adipose tissue, which could cause difficulties during the surgical procedure. Differently, SVF can be prepared at the point of care from a relatively small volume of lipoaspirate, with minimal training, using manual protocols or automatic devices. Furthermore, compared to the use of AD-MSCs, SVF offers more benefits, reducing the risks and inconveniences associated with cell cultures and multiple passages.

For these reasons, SVF can be a potential regenerative candidate to bypass the issues associated with using AD-MSCs.

1.1.2 SVF formulations and extraction

SVF composition varies depending on the processing protocol[8, 9]. SVF represents a freshly isolated cell mixture present in the adipose tissue. It's composed of smooth muscle cells, preadipocytes, endothelial cells, immune system cells (like anti-inflammatory M2 macrophages and regulatory T cells), fibroblasts, and several multipotent stem cells, such as hematopoietic progenitor cells, pericytes, and AD-MSC. All these cell components are kept together by ECM elements, such as collagen, elastin, and glycoprotein, and form the stromal connective tissue.

There are two methodologies to obtain the SVF from lipoaspirates or excised fat: chemical or physical methodologies. The chemical is based on enzymatic digestion of the adipose tissue and is commonly performed with collagenase. SVF was traditionally isolated with this enzymatic methodology, but from 2007, this procedure was forbidden for clinical use because the product obtained is considered substantially manipulated (disagreement with Good Manufacturing Practice regulations of the European Parliament and Council, EC regulation no. 13394/2007). For this reason, in recent years was developed physical methodologies based on the mechanical treatment of adipose tissue (microfragmentation, shaking, vortexing, and sonification etc.) have been developed[10, 11]. The two techniques have essential differences: the physical

methodologies are faster, easier, and cheaper than the enzymatic digestion, but the efficiency of cell extraction is lower than collagenase. Indeed, also the products obtained from the two methodologies have some differences[6]. SVF extracted with enzymatic digestion is a suspension of different stromal cell phenotypes, while the SVF extracted with physical methodology preserves cell-matrix and cell-cell interaction inside of the fragments of the extracellular matrix[12]. Regardless of the procedure for SVF preparation, the goal is to maintain the viability of the stem cells along with the stromal cell niche, all of which account for the potential therapeutic benefits of distinct SVF products[7].

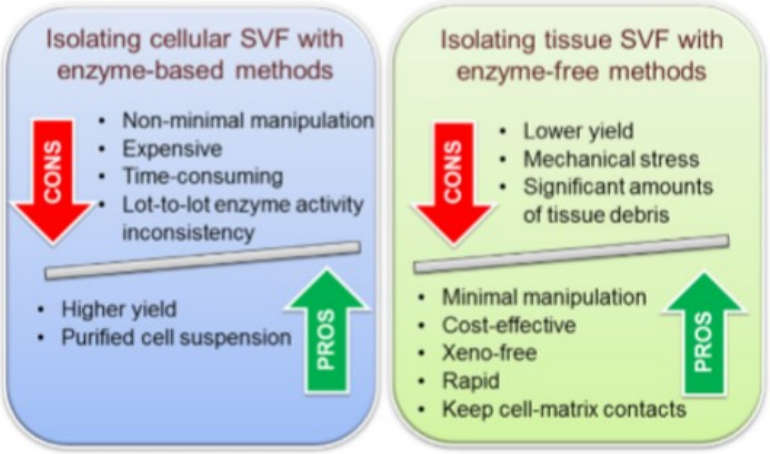

Figure 1. Pros and Cons of chemical and physical treatment of adipose tissue.

1.1.3 Mechanisms of action of SVF

The regenerative capacity of SVF is likely derived from the heterogeneity of its constituents that provide numerous mechanisms for regeneration to occur[13]. The mechanism of the therapeutic effect of SVF is poorly understood, and potential tissue or organ-specific action.

The SVF interacts and triggers a range of pro-regenerative pathways. The main SVF biological actions are proangiogenetic, antiapoptotic, antifibrotic, immune regulatory, anti-inflammatory, and trophic.

Some of these effects may be attributable to the presence of AD-MSC (2-10%), while others are associated with the vascular niche and, alternatively, to the interaction and crosstalk between cell subtypes present in SVF.

1.1.3.1 Angiogenesis

The pro-angiogenic activity can be attributed to the crosstalk between endothelial progenitor cells (EPCs) and AD-MSC[14]. Indeed, coculture between AD-MSC and EPC results in the formation of an enhanced vascular network during 14 days of incubation[15]. The growth factors released by ECPs, such as vascular endothelial factor (VEGF) and insulin-like growth factor-1 (IGF-1), have the capacity to induce angiogenesis[16]. Its *in vivo* application has successfully resulted in neovascular formation when applied to acute myocardial infarction, cosmetic procedures, burn wounds, diabetic foot ulcers, and ischemic muscle[17].

1.1.3.2 Immunomodulatory effects

The immunological and anti-inflammatory properties are due to the diverse cell components. AD-MSC have anti-inflammatory and anti-apoptotic proprieties, and in the health adipose tissue are present anti-inflammatory M2 macrophages[18]. SVF also contains T regulatory cells (Treg) that express high levels of immune suppressive cytokines, that maintain macrophages in the M2 phenotype[18].

Several therapeutic investigations have reported an initial reduction in inflammation and immune response following SVF injection[19]. This immunomodulatory effect of SVF is attributed to its varied cellular components. AD-MSC and progenitors are recognized for their anti-inflammatory and anti-apoptotic characteristics, that contribute to regeneration of host tissue. For example, in an experimental autoimmune encephalitis model for multiple sclerosis, SVF demonstrated greater efficacy than AD-MSCs in reducing inflammation and delaying the onset of disease with a lower clinical disease score[19].

1.1.3.3 Extracellular matrix (ECM) components

The ECM is composed of structural proteins such as collagen, laminin, fibronectin, and elastin, which are commonly secreted by fibroblasts. ECM is an essential component to ensure cross-talking interactions among all cellular

components. Additionally, it recreates the autologous microenvironment as similar as possible to an original tissue. The ability of the ECM to act as a robust scaffold, keeping nearby cellular elements close and dynamically interacting with them, initiates a series of pathways that accelerate regenerative functions[20]. The ECM also facilitates cellular recruitment and migration, as the cell uses integrin-cytoskeleton attachments to put itself forward[21] . Furthermore, ECM contributes to the angiogenetic process, mediating the growth and formation of vascular networks[22].

1.1.3.4 Paracrine activities

While SVF cells contribute to tissue formation by differentiation of their individual components, there is also evidence of regeneration occurring through paracrine signaling involving cross-talking between the different cell population of SVF and their host environment[23]. SVF cell components secrete factors such as growth factors, cytokines, and extracellular vesicles (EVs) that are responsible for chemoattraction, angiogenic, anti-inflammatory, and prosurvival effects required for tissue regeneration[24].

1.1.3.5 Extracellular vesicles

The extracellular vesicles (EVs) are a heterogeneous group of cell-derived membranous structures produced for intracellular communication. They are located in different types of tissues or biological fluids, including blood, urine, saliva, cerebrospinal fluid, breast milk, lymph, synovial, and seminal fluid[25, 26]. EVs expressed in physiological and pathological conditions exchange components between cells, such as proteins, nucleic acids, lipids, and enzymes[27].

Based on their size, morphology, and biogenesis, EVs can be divided into two main categories: exosomes and microvesicles.

The exosomes refer to membrane vesicles with a size ranging from 30 to 100/150 nm realized by reticulocytes during differentiation[28]. Exosomes are intraluminal vesicles (ILVs) formed by the inward budding of the endosomal membrane during the maturation of multivesicular body (MVBs), which are

intermediates within the endosomal system, and secreted upon fusion with exocytosis with the cell surface[29].

Microvesicles or ectosomes range in size from 50nm to 1000nm, assembled and realized from the plasma membrane. Indeed, they are generated by the outward budding and fission of the plasma membrane and the subsequent release of vesicles into the extracellular space, taking within some of the cytosolic content and membrane receptors of the paternal cell[30].

Although both exosomes and microvesicles have the function of intercellular communication and signaling, they differ in the expression of specific biomarkers due to their distinct origin, and molecular content due to their biological function. Exoxoses display several cell membrane proteins on their surfaces, and the most common biomarkers are tetraspanins (CD63, CD81, CD82, CD9, and CD37), heat-shock proteins (Hsp60, Hsp70, Hsp90, and Hsp20), tumor susceptibility gene (TSG101), annexin, flotillin, and apoptosis-linked gene 2-interacting protein X (ALIX)[31]. In addition, specific transmembrane proteins are present on the surface, such as epithelial cell adhesion molecule (EpCAM), epidermal growth factor receptors (EGFRs), lymphocyte function-associated antigen 1 (LFA-1), and endoglin (CD105). Exosomes may contain and transport DNA, mRNAs, pre-mRNAs, and other noncoding RNAs that are transferred to the recipient cells or tissue[32] after the interaction and attachment with the above molecules[26].

Microvesicles (MVs) express numerous features of the donor cell including specific surface antigens and receptors[33]. MVs express the specific protein CD144 on their external leaflet, platelet-derived microvesicles (PMVs) released from activated platelets express specific protein CD41, and leukocyte-derived microvesicles (LMVs) express as a specific marker CD18[34]. All MVs have phosphatidylserine (PS) on the outer face of plasmalemma, a common specific marker. MVs are also in the surface marker CD40, as well as cholesterol, sphingomyelin, and ceramides[35]. Furthermore, MVs carry the origin cell-specific membrane proteins on the surface, such as macrophage integrin-1 (Mac-1), tissue factor (TF), P-selectin, E-selectin, CCL5 (chemokine CC-motif

ligand 5), stromal cell-derived factor (vWF), monocytes chemoattractant protein-1 (MCP-1), matrix metallopeptidases (MMP2, MMP9), vascular endothelial growth factor (VEGF), DNA, mRNAs, miRNAs, non-coding RNAs, and peroxisome proliferator-activated receptor gamma[36].

The EVs derived from the SVF and the cells within it can have a paracrine role in repairing and regenerating damaged tissue.

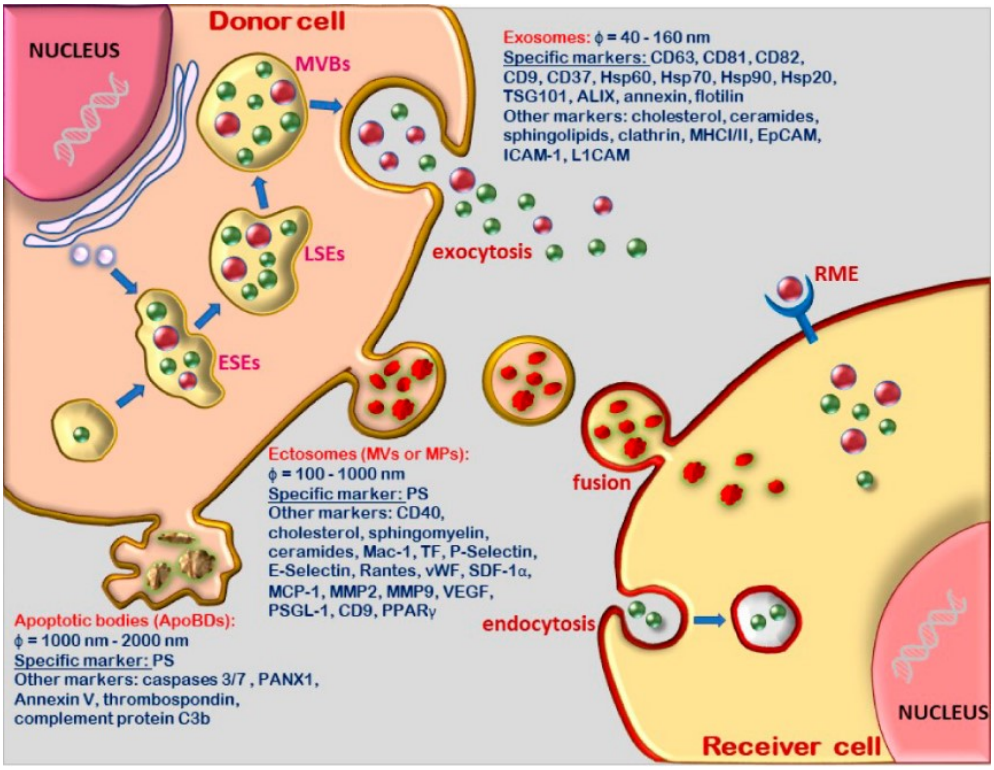

Figure 2. Diagram represent the classification, biogenesis, molecular content and interactions with target cells of EVs. Exosomes originate from the early sorting endosome (ESE), which turn sequentially into late sorting endosome (LSE), and multivesicular bodies (MVBs), whose intraluminal vesicles (ILVs) are exocytosed upon fusion and inward invagination of the plasmalemma. Ectosomes, also named microvesicles (MVs) are formed upon plasma membrane budding with phosphatidyl serine (PS) on the outer membrane surface. Apoptotic bodies (ApoBDs) are membrane-derived large vesicles originating form apoptotic cells with PS as surface marker. Image form Georgescu and Simionescu, Extracellular vesicles: versatile nanomediators, potential biomarkers and therapeutic agent in atherosclerosis and COVID-19-related thrombosis, 2021.

1.2 HYALURONIC ACID

Hyaluronic acid (HyA), or hyaluronan, is a natural linear polysaccharide composed of alternating units of repeating disaccharide of N-acetyl-D-glucosamine and D-glucuronic acid linked by β (1,4) and β(1,3) glycosidic bonds[37, 38] (Figure 5). HyA is a non-sulfated glycosaminoglycan (GAG) present in all tissues and fluids of the body. HyA is most abundant in the skin (50% of the total body HyA), the vitreous of the eye, the extracellular matrix (ECM) of cartilage tissues, the umbilical cord, and synovial fluid, but it is also present in other parts of the body, such as skeletal tissues, heart valves, the lung, the aorta, the prostate, tunica albuginea, corpora cavernosa and corpus spongiosum of the penis[39]. HyA is an essential component of the ECM, in which its structural and biological properties mediate its activity in cellular signaling, wound repair, morphogenesis, and matrix organization[40].

It has good biocompatibility, biodegradability, and non-immunogenicity, with anti-inflammatory and bio-stimulated effects[41]. These characteristics make HyA a promising candidate for the tissue regeneration process[42, 43].

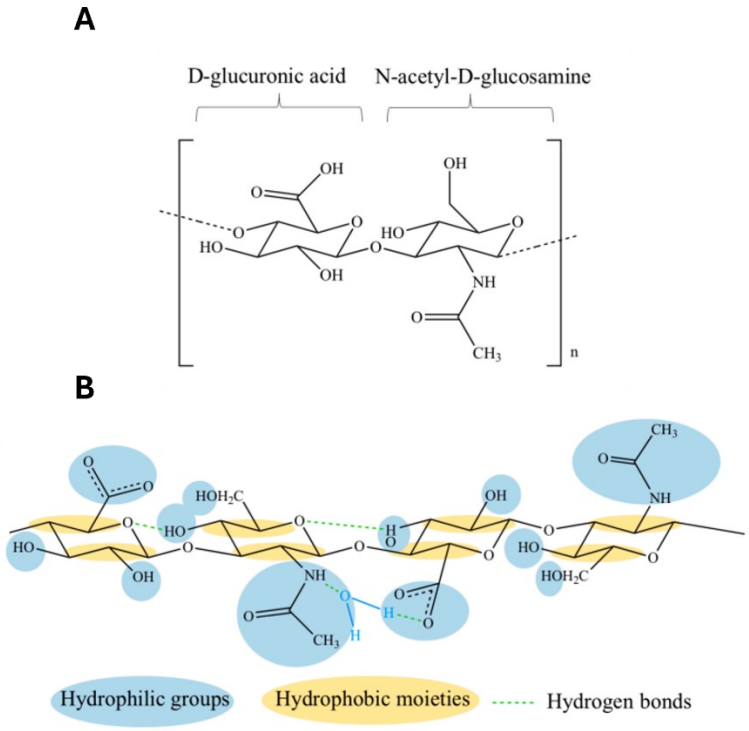

Figure 3. Chemical structure of HyA. (**A**) Chemical structure of Hya disaccharide unit, (**B**) and HyA tetrasaccharide unit when the hydrophobic functional groups and the hydrophobic moieties are respectably evidenced in blue and yellow, while the hydrogen bonds are represented by green dashed lines. Image form Fallacara et al., Hyaluronic acid in the third millennium, 2018.

1.2.1 Structure, functions, and degradation

The simple molecular unit repeated thousands of times form a structure of long linear polymer, with a molecular weight (MW) reaching very high molecular weight, up to 20,000 kDa[37, 44]. HyA is synthesized by HyA synthetases on the inner surface of the cellular membrane and translocate into extracellular space for elongation[45, 46]. The different types of hyaluronidase generate HyA with different molecular weights, that exhibit different biological effects[47]. For instance, high molecular weight HyA displays anti-inflammatory and immunosuppressive properties, controlling the recruitment of inflammatory cells. In contrast, low molecular weight HyA is a potent proinflammatory molecule and promotes angiogenesis and tissue remodelling in the wound healing process. It is also able to inform the cells about stress conditions[48].

Two mechanisms carry out the degradation of HyA in the human body. The first one is specific, mediated by enzymes, the hyaluronidases (HYALs), that can cleave the β—1,4 glycosidic bonds. The second is non-specific, determined by oxidative damage due to reactive oxygen species (ROS)[49]. According to these degradation mechanisms, it is estimated that the half-life of HyA varies from 12-24 hours in the skin to a few minutes in the bloodstream[50].

The balance between the synthesis and degradation process, and the MW disposition plays an essential regulatory role in the containment of human homeostasis.

1.2.2 Biological functions

HyA participates in multiple biological functions, such as lubrification, hydration, matrix structure, and steric interactions, and is involved in several cellular interactions that are important for proliferation, differentiation, development, and

recognition[41, 51, 52]. HyA is the most abundant component of ECM, which performs its biological function according to two mechanisms:

- passive structure molecule, that is related to their physiochemistry propriety[53]. The unique structure of HyA, a long, negatively charged, randomly coiled with its macromolecular size, hydrogroscopy, and viscoelasticity, modulates the tissue hydration, osmotic balance, and physical proprieties of ECM. HyA maintains all the components of ECM (cells, collagen, and elastic fiber) and determines the cell migration rate according to the matrix porosity it forms[54].
- Signalling molecules interacting with molecules of ECM and cell surface receptors, the hyaladherins[55, 56]. These interactions are essential in developing cells and organs in response to tissue damage, inflammation, cell migration, formation, and resistance to cancer.

  Hyaladherins are divided into three main classes:

  - CD44: is a cell surface glycoprotein adhesion receptor that can interact with HyA[51, 53]. It is expressed in many isoforms and spread in many cell types[53]. When the CD44 extracellular domain interacts with HyA, the CD44 intracellular domain interacts with the cytoskeleton, forming a cytoskeleton-biopolymer link[53]. The CD44 cellular receptor can interact with HyA with different MW or small fragments of HyA, activating different pathways and functions, such as cell adhesion, migration, inflammation, and tumour metastasis[57].
  - RHAMM: is a receptor for HyA-mediated cell mobility, or CD168. It is expressed in several isoforms, and the location is not only in the cell membrane but also in the cytoplasm and nucleus[50]. RHAMM regulates cellular response to growth factors and plays a role in cell migration, particularly for fibroblasts and smooth cells. The HyA-RHAMM interactions have roles in inflammation and tissue repair, triggering various signaling pathways (cell migration, adhesion, and proliferation) and controlling cells such as macrophages and fibroblasts. The RHAMM is expressed on the cell surface, interacts with CD44, and modulates cell mobility, wound healing, and signal

transduction. At the intracellular level, RHAMM binds to actin filaments, podosomes, centromeres, microtubules, and mitotic spindle, affecting crucial cellular processes[58].

- ICAM-1: the intercellular adhesion molecule 1 or CD45 is a cell surface glycoprotein typically expressed on endothelial cells and cells of the immune system. This molecule may also release HyA from the body fluid and plasma, responsible for most of its turnover. The interaction between HyA and ICAM-1 also regulates the inflammatory reaction[59].
- HARE: the HyA receptor for endocytosis is expressed in the inner surface of endothelial cells in vascular and lymphatic vessels. This receptor mediates the systemic clearance of HyA from the circulatory and lymphatic systems[60, 61].
- LYVE-1: the lymphatic vessel endothelial receptor-1 is expressed in the vascular lymph endothelium and macrophages. It controls the renewal of HyA meditating its absorption from the tissues into the lymph[53, 56].
- TLRs: toll-like receptors are usually expressed on sentinel cells, such as macrophages and dendritic cells. The interaction between HyA and TLRs in the surfaces of immune system cells switches on a pro-inflammatory response[56, 62].

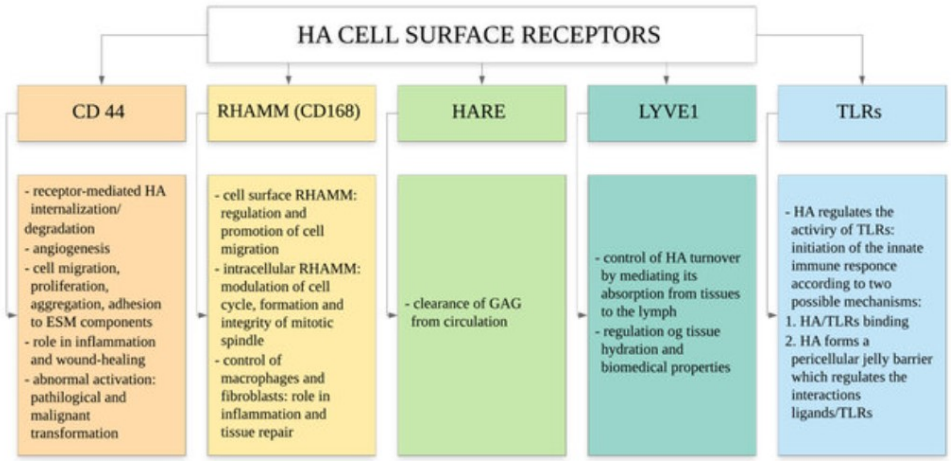

Figure 4. HyA cell surface receptors and their functions. Image form Fallacara et al., Hyaluronic acid in the third millennium, 2018.

1.2.3 Modification of hyaluronic acid for biomedical applications

The HyA can be considered an essential building block for creating new biomaterials with utility in tissue engineering, regenerative medicine, and drug delivery[41-43, 63]. There are several modifications and functionalizations in the structure of HyA that can be customized for specific applications. During the modification process, it's important particular attention in maintaining the native HyA properties, such as biocompatibility, biodegradability, and mucoadhesive[64]

1.2.3.1 Chemical addition of pendant groups/conjugation

Conjugation is the chemical addition of a monofunctional compounds into an HyA chain by single covalent bound[53]. In general, chemical modification occurs in the liquid phase, with water or other organic solvents, such as dimethyl sulfoxide (DMSO), dimethylformamide (DMF), and hexafluoroisopropanol[53]. A final purification step is necessary to remove any unreacted reagents that could cause toxicity. The chemical modifications target three functional groups: the glucuronic acid carboxylic acid, the primary and secondary hydroxyl groups, and the N-acetyl group. The most common modifications are the carbodiimide-mediated reactions, esterification, and amidation on the carboxylates, etherification, divinyl sulfone crosslinking, esterification, and bis-epoxide crosslinking on the hydroxyls. The chemical-modified HyA is divided into two categories:

- monolithic HyA derivates are terminally modified forms of Hya that can not form new chemical bonds in the presence of cells or tissues and must be processed and fabricated into different forms;
- living HyA derivates can form new covalent bonds in the presence of cells, tissue, and therapeutic agents. These compounds are usually required to create 3D cell cultures and in vivo cell delivery.

1.2.3.2 Crosslinking

A polyfunctional compound is linked to more than one original or modified HyA by two or more covalent bonds. Crosslinking is mainly used in the preparation of HyA hydrogel[65]. Crosslinking can be induced in two ways, chemical or physical. The most common chemical compounds that produce crosslinking are dithiothreitol (DTT), sodium tetrathionate, polyethylene glycol (PEG)-dithiol, and peptide-linked. The benefits of this methodology are to form derivates with high molecular weight, a high degree of substitution, and require a short activation time.

Differently, physical crosslinking can be produced using pH, temperature, ionic strength, photo-induction, and enzymatic-induction. The advantage is that it endured minimal toxicity due to no other crosslinking agents being used[66].

1.2.4 Applications of hyaluronic acid

Thanks to its numerous proprietaries (Fig 5), the incorporation of HyA in wound healing improves tissue regeneration. HyA finds numerous applications, including:

- Drug delivery: HyA-based nanoparticles and hydrogel are used as drug delivery vehicles to improve the solubility, stability, and targeted delivery of pharmaceutical compounds[67].
- Molecules delivery: ECMs hydrogel control the spatiotemporal release of grow-factors, to induce a regenerative action.
- Tissue engineering: HyA scaffolds are used in tissue engineering applications to support cell growth and tissue regeneration. Indeed, HyA has the ability to mimic the microenvironment provided by the ECM and accelerate cell proliferation in the injured site. For example, HyA sustains wound healing and re-epithelialization process, thanks to ability to increase cell proliferation, migration, and adhesion in the wound site[68].
- Cell delivery: HyA scaffolds have the capacity for cell retention, thereby enhancing the natural biological repair processes mediated by endogenous cells[43, 69]. The encapsulation of cell types inside an HyA scaffold allows the recreation of different microenvironments, reducing inflammation and stimulating the regeneration process[70].

- Orthopaedics: HyA injections are used to treat osteoarthritis by lubricating and cushioning the joints, reducing inflammation, and improving mobility[69].
- Ophthalmology: HyA is used in eye drops and ointments to lubricate the eyes and provide relief from dryness and irritation[69, 71].
- Dermal fillers: HyA is injected beneath the skin's surface to add volume, smooth wrinkles, and enhance facial contours[72].

Figure 5. Medical, pharmaceutical, cosmetic, and dietary applications of HyA and its derivates. Image form Fallacara et al., Hyaluronic acid in the third millennium, 2018.

1.3 SKELETAL MUSCLE

Skeletal muscle consists of hierarchically organized muscle fibers, also known as myofibers, blood vessels, nerves, and connective tissue. Myofibers, the functional muscle unit, are formed by the fusion of myoblasts into elongated, cylindrical, multi-nucleated fibers named myotubes, which are 10-100 µm in diameter[73]. The plasma membrane of the muscle fibers is called the sarcolemma, and the cytoplasm is referred to as sarcoplasm. As myofibers mature, their nuclei are located along the periphery below the sarcolemma. The parallel myofibers are bundled into fascicles enclosed by the perimysium. Somatic motor neurons innerve the skeletal muscle for the contraction.

Each muscle fiber is composed of many myofibrils, which contain sarcomeres identified between two cytoskeletal structures called Z-bands, the contractile unit of the skeletal muscle. The sarcomeres contain contractile proteins, thin filament actin, and thin filament myosin[74].

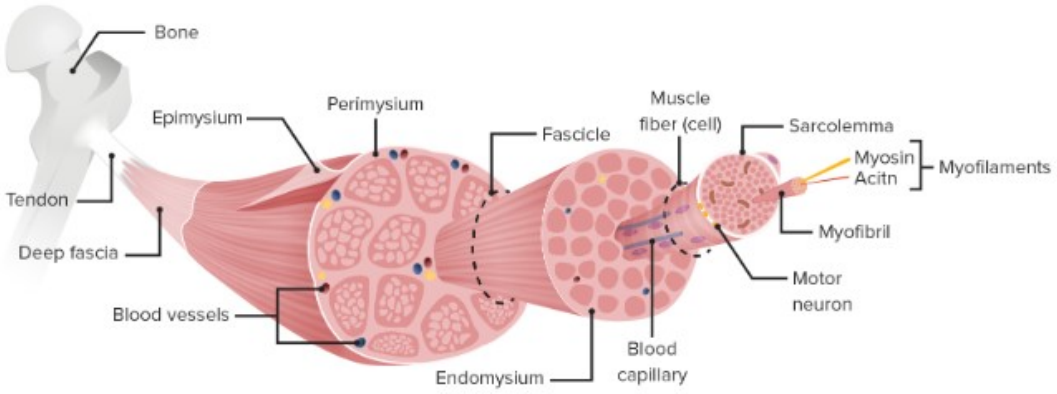

Figure 6. Skeletal muscle anatomy.

1.3.1 Anatomical and histological characterization of posterior compartment of the hindlimb

Skeletal muscle tissue is composed of thousands of muscle fibres, that differ for the contractile and metabolic properties. There are two main fibre types[75]:

-type 1 fibres, slow-twitch oxidative, red muscle, that contain more mitochondria, possess a high oxidative capacity, and are resistant to fatigue.

-type 2 fibres, fast-twitch glycolytic, white muscle, possess a high glycolytic capacity, and fatigue easily.

It is known that the fibre typer composition can be vary depending on exercise performance, fatigue resistance, and metabolic activity[76]. Furthermore, animal model studies demonstrated a strong relationship between muscle fibre types and pathological conditions or clinical manifestation, such as diabetes and obesity[77].

Myosin is a predominant and the kye component of skeletal muscle proteins, that have the ability to generate contractile force through the consumption of ATP (Figure 7A). The myosin molecule is composed of hexamer consisting of two

identical myosin heavy chain (MyCH) subunits and four light-chain subunits. The catalytic domain is located within the MyCH subunits, and its function is to hydrolysed ATP and interact with actin[78]. To date, four predominant MyHC isoforms have been identified in adult rodent skeletal muscles: MyHC1, 2A, 2X, and 2B[79]. MyHC1 is expressed in slow-type 1 muscle fibres. Meanwhile, fast-type 2 fibres are subdivided into 2A, 2X, and 2B muscle fibres, which preferentially express MyHC2A, 2X, and 2B, respectively. Type 2A and 2X fibres exhibit intermediate contractile characteristics of type 1 and type 2B fibres.

The main mammal's posterior compartment of the leg is formed by 3 types of muscles: soleus, plantaris, and gastrocnemius (medial: MG and lateral: LG)[80] (Figure 7B, C). They extend behind the knee and into the sural region (calf) of the posterior leg with the flexion function of the foot at the ankle joint and of the knee ate the knee joint. The immunostaining figure shows that soleus is characterized by mixed fibre composition, with an hight presence of slow-type 1 muscle fibres that express MyHC1, and fast-type 2 fibres that express MyHC2A and MyHC2X. The plantaris mainly express fast-type 2 fibres, with an hight quantity of MyHC2B, but also My2A and 2X. Lastly, gastrocnemius is predominantly marked with fast-type 2 muscle fibres with MyHC2B expression, but in the plantaris and soleus proximal regions its express also some MyHC2X and 2B[80].

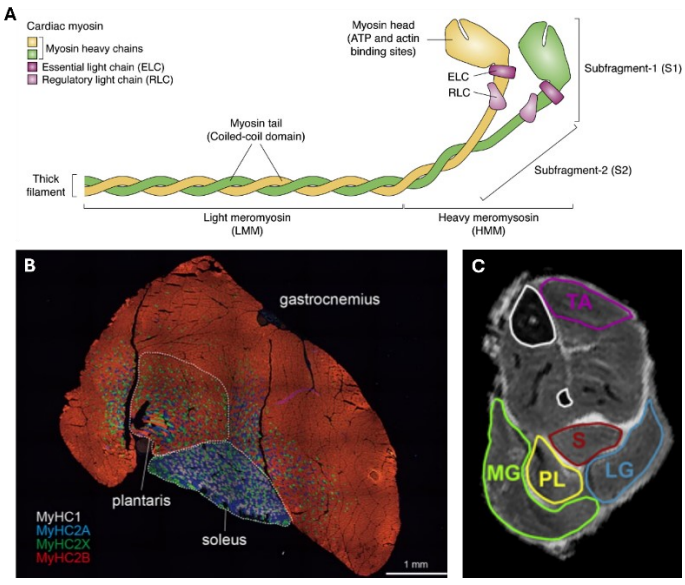

Figure 7. (**A**) Myosin structure, that consists in two heavy chains (yellow and green), each bound to an essential light chain (ELC, dark pink), and a regulatory light chain (RLC, light pink). The myosin heads (S1 region) contain the sites of ATP and actin binding. The tails (LMM) are coiled coils that assemble into the thick filaments. Image form Barrick et al., Cardiac myosin contraction and mechanotransduction in health and disease, 2021. (**B**) Mouse cross-section immuno-stained. Cross-section are obtained from calf muscle including gastrocnemius, plantaris, and soleus muscle, and immunopositive MyHC isoforms are visually classified as MyHC1 (white), MyHC2A (blue), MyHC2X (green), and MyHC2B (red). 10x magnification. Image form Sawano et al., A one-step immunostaining method to visualize rodent muscle fiber type within a single specimen, 2016. (**C**) Manual segmentation of high-resolution MRI of mouse calf muscles, formed by lateral gastrocnemius (LG), medial gastrocnemius (MG), plantaris (PL), soleus (S), and tibial (TA). Image form Zhang et al., Magnetic resonance imaging of mouse skeletal muscle to measure denervation atrophy, 2007.

1.4 SKELETAL MUSCLE REGENERATION

Satellite cells (SCs) are the muscle-resident stem cells that are located between the sarcolemma and basal lamina of myofibers and also close to the blood capillaries[81]. They are responsible for skeletal muscle growth and regeneration. SCs reside in a specialized microenvironment known as the niche, which contains stem cells, soluble factors, ECM, vascular networks, and cell adhesion molecules [82-84]. The satellite niche is responsible for maintaining the physiological quiescent stem cells population from diminishing and also for regulating the response to different stress, such as excise, injury, or disease[82]. SCs express the transcription factors Pax7 and Pax3, as well as myogenic factor 5 (Myf5)[85]. Pax7 is the most important marker for the maintenance of SC function and can be expressed in particularly in quiescent and proliferating SCs[81, 85, 86].

The maintaining of a small number of SCs in a quiescent state is fundamental for the replenishment of the stem cell pool (self-renewal ability). In the case of stress signaling, the SCs, once activated, migrate to the injury site and differentiate into skeletal myoblast to regulate muscle regeneration[87]. Upon activation, SCs move out of the basal lamina, upregulate the expression of MyoD, Pax7, and Myf5, and then undergo a cell cycle to generate myoblasts. After cell divisions, myoblasts exit this

cycle and fuse directly with the existing injured myofibers, or they fuse to generate multi-nucleated myotubes following the increased expression of myogenin (Myof4) in the terminal differentiation process. The myotubes express desmin, myosin heavy chain (MyoH), and α-actinin, and can form mature myofibers [88].

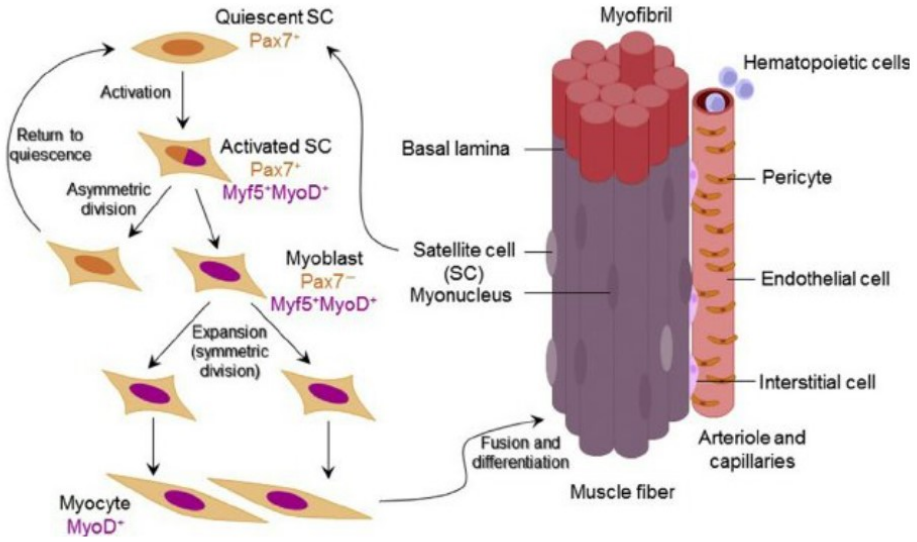

Figure 8. Skeletal muscle resident stem cells. SCs (Pax7 +) reside in the space between the sarcolemma and the basal lamina and are required for repair and regeneration of the myofiber following injury. SCs activation in response to injury includes upregulation of the myogenic regulatory factors Myf5 and MyoD and asymmetric cell division. Newly formed myoblasts or myocytes can fuse with damaged fibers or fuse together to form new fibers in the muscle environment. Pax7 (nonsatellite) stem cells (interstitial cells) and pericytes are located outside the basal lamina in close proximity to vessels. The majority of nonsatellite stem cells in muscle contribute to repair via secretion of factors that allow for satellite cell activation. Image form Marni Boppart et al, Exrcise and Stem cells, 2015.

1.5 MUSCLE INJURY

Common causes of skeletal muscle injuries include high-energy traffic accidents, blast trauma, combat injuries, surgical and orthopaedic procedures (such as after-compartment syndrome or tumour removal), and sports-related contusions leading to acute muscle tissue loss[89]. Progressive muscle loss can occur due to metabolic disorders or inherited genetic diseases like Duchenne muscular dystrophy, Amyotrophic Lateral Sclerosis, and pediatric Charcot-Marie-Tooth disease[90-92].

Another common cause of muscle damage leading to subsequent functional impairment is the phenomenon of ischemia-reperfusion. Indeed, physiological and anatomical studies show that irreversible muscle cell damage starts after 3 hours of ischemia and is nearly complete at 6 houses [93].

A muscle injury is typically quantified as decreases in force production, disruptions in the normal structure of myofibrils, or loss of volume[94].

The most rigorous assessment of injury involves quantifying the loss of muscle contractile function, such as reductions in force production relative to muscle cross-section (specific tension or specific force), increases in time-to-peak force production, loss of peak tetanic force, or increases in fatigability[94]. The skeletal muscle tissue has the ability to self-repair. However, severe injuries involving volumetric muscle loss (VML), or disruption of myofibrils result in permanent functional limitation. It can substantially impact the quality of life of patients by significantly reducing the functionality of the locomotion system.

1.5.1 Ischemic reperfusion injury

1.5.1.1 Pathophysiology

Ischemia is a deficient blood supply to tissue resulting from a blockage in arterial inflow. Tissue injury and death occur as a result of the initial ischemic insult, which is determined primarily by the magnitude and duration of the interruption in the blood supply, and then subsequent damage induced by reperfusion. The total tissue injury is attributable to an ischemic component followed by the blood supply reestablishment[95]. The first are tissue injury processes due to ischemia *per se.*

Ischemia leads to three fundamental mechanisms/events:

a) triggering of anaerobic metabolism, which decreases cellular pH. The accumulation of hydrogen ions activates the Na^+/H^+ exchanger to excrete excess hydrogen ions, which causes a large influx of sodium ions;

b) depletion of cellular ATP, which inactivates the ATPase pump, reduces active Ca^{2+} efflux, and limits calcium reuptake by the endoplasmic reticulum (ER), thereby producing calcium overload in the cell;
c) opening of the mitochondrial permeability transition (MPT) pore, which dissipates mitochondrial membrane potential and further impairs ATP production[96].

Although the delivery of oxygen, substrates required for aerobic ATP generation, and normalization of extracellular pH are restored by reperfusion. This phase triggers multifactorial complex mechanisms and involves:

d) generation of reactive oxygen species (ROS) caused by the reintroduction of molecular oxygen when the blood flow is re-established;
e) calcium overload;
f) opening of MPD pore;
g) endothelial dysfunction;
h) appearance of a prothromobogenic phenotype;
i) pronounced inflammatory response[97].

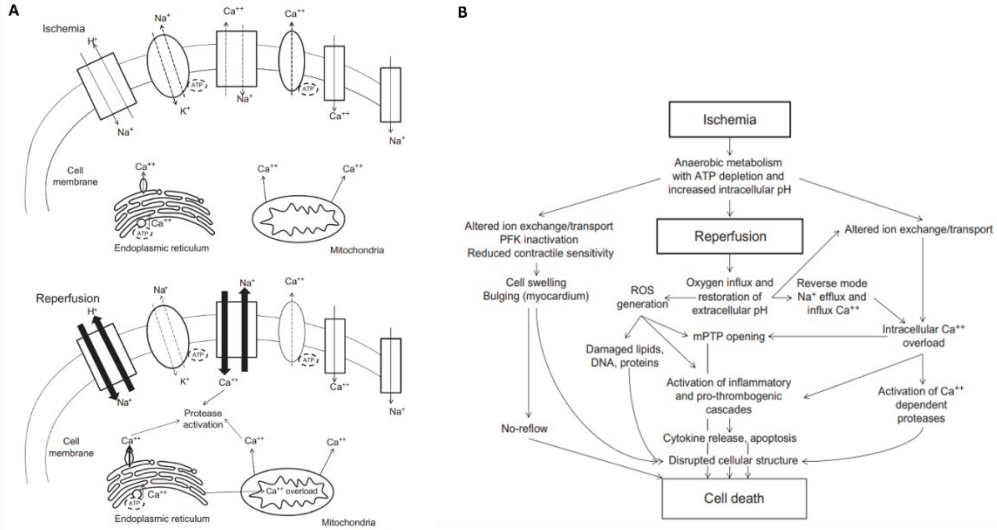

Figure 9. Ischemic reperfusion injury. (**A**) Major pathological events contributing to ischemic (upper panel) and reperfusion (lower panel) components of tissue injury. (**B**) Overall integrated responses to I/R injury summer. Image from Kalogeris et al., Cell biology of ischemia/reperfusion injury, 2012.

1.5.1.2 Molecular and biological mechanisms in ischemic/reperfusion injury

Interconnecting multifactorial outcomes are caused in response to the ischemic perturbation followed by reperfusion when the blood supply is re-established.

1.5.1.2.1 Calcium overload

During ischemia, an anaerobic metabolism is triggered. This leads to the accumulation of hydrogen irons with the activation of Na^+/H^+ exchanger to excrete excess hydrogen ions. The Na^+ ions are, in turn, exchanged for Ca^{2+} by the Na^+/H^+ poms[98]. In addition, the endoplasmic/sarcoplasmic reticulum Ca^{2+} reuptake is impaired during I/R injury[99]. These mechanisms cause the alteration in intracellular Ca^{2+} concentration, which can contribute to cell death.

The mitochondrial increase of Ca^{2+} can induce the opening of the MPT pore, which dissipates mitochondrial membrane potential and further impairs ATP synthesis. In addition, water enters the mitochondria, causing sweat and rupture. The high concentration of intracellular Ca^{2+} leads to the pathological activation of Ca^{2+} / calmodulin-dependent protein kinase (CaMKs), contributing to cell death[100]. Increased Ca^{2+} can also activate calpains, some cysteine proteases that degrade cytoskeletal, ER, and mitochondrial proteins. Generation of calcium pyrophosphate complexes and formation of uric acid followed by high levels of Ca^{2+} can induce the activation of inflammasomes complex that mediates increase of production of inflammatory cytokines (e.g., IL-1β and TNFα), which in turn, activate transcriptional factors (e.g., NFkB).

1.5.1.2.2 Reactive oxygen species

Re-entry of oxygenation blood into ischemic tissue results in the production of toxic ROS, such as superoxide anions (O2-), hydroxyl radical (OH-), hypochlorous acid (HOCl), hydrogen peroxide (H2O2), and nitric oxide-derived peroxynitrite[101] by mitochondrial enzymes. The ROS productions induce the destruction of cell and organelle membrane and DNA single-

stand breakage with resultant enzyme inactivation, as well as activation of nuclear enzyme poly (ADP-ribose) synthetase, leading to cell death[102]. ROS are potent oxidizing and reducing agents that directly damage cellular membranes by lipid peroxidation[103], creating toxic metabolites such as malondialdehyde[104]. In addition, ROS stimulates leukocyte chemotaxis and activation by activating plasma membrane phospholipase A_2 to form arachidonic acid[103]. These toxic compounds can increase leukocyte activation, chemotaxis, leukocyte-endothelial adherence, and expression of pro-inflammatory mediators by various cell types[105].

1.5.1.2.3 Endoplasmic reticulum stress

The function of ER can be compromised by stress stimuli, which cause an accumulation of misfolding and unfolding proteins. The ER stress can be captured by some membrane receptors, which activate the unfolded protein response (UPR) and act by increasing the expression of ER-resident chaperones, increasing protein transduction, and accelerating the degradation of unfolded proteins[106]. However, an I/R stress can compromise the UPR system and trigger cell death.

1.5.1.2.4 Mitochondrial dysfunction

Mitochondria have a significant role in the progression of I/R injury and contribute to cell death. Due to the activation of anaerobic metabolism during ischemia, electron flow through the respiratory chain is inhibited, and ATP production is blocked[107]. In addition, blocking oxidative phosphorylation also inhibits the breakdown of fatty acids, which accumulate in the cells[108].

During the reperfusion, the huge increases in mitochondrial Ca^{2+}, coupled with the ROS burst, induced the opening of the MPT pore, which caused mitochondria to swell and rupture[109].

1.5.1.2.5 Activation of mechanism of cell death

Four different types of cell death pathways are initiated by I/R injury.

- Apoptosis: is a regulated cell death that causes cell shrinkage and condensation of the cytosol and nucleus, eventually forming apoptotic bodies. Phagocytes can engulf the apoptotic bodies without evoking an inflammatory response. Apoptosis is divided into the "extrinsic" and "intrinsic pathways[110].
- Autophagy: is the cell's primary mechanism to remove damaged or senescent protein aggregates and organelles. These obsolete components are enclosed in membrane-lined vesicles called phagosomes, which fuse with lysosomes, contacting enzymes that degrade the ingested materials without an inflammatory response. Thus, autophagy is a cell survival mechanism, but I/R injury may contribute to triggering uncontrolled autophagy[111].
- Necrosis: occurs due to a dysfunctional ion transport mechanism, which causes cell and organelle swelling, mitochondrial dysfunction, lack of nuclear fragmentation, plasma membrane rupture, and leakage of intracellular contents. In contrast to programmed cell death, such as apoptosis and autophagy, necrosis is believed to occur by a random, uncontrolled process in response to stress[112]. Necrosis causes the release of pro-inflammatory, cell disintegration, and fibrosis.
- Necroptosis: is a programmed necrosis. Cell stress activates the receptor-interacting proteins (RIPs), leading to increased ROS production either through activation of NADPH oxidase or increased mitochondrial oxidant production[113]. The MPT pore is one potential mitochondrial target for RIP-mediated necrosis, leading to ATP depletion, ROS production, and swelling and rupture of the organelle[98, 114].

1.5.1.2.6 Inflammation

Sterile inflammation caused by I/R injury is characterized by the marked recruitment of neutrophils and the production of cytokines, chemokines, and other pro-inflammatory stimuli[114]. Pro-inflammatory responses generated by necrotic cells and mediators formatted by attract neutrophil infiltration, ROS

production by XO and other enzymes promote leukocyte adhesive interaction with endothelium postcapillary venules and subsequent transmigration into the tissue. The activation and transmigration of leukocytes induce microvascular barrier dysfunction via release of oxidants and hydrolytic enzymes[114]. Neutrophils secrete pore-forming molecules to parenchymal cells, that increase cell damage and death. Coincident with these phenomena, perivascular cells (e.g. macrophages, mast cells) become activated and release inflammatory mediators[115].

1.6 ACUTE LIMB ISCHEMIA

Peripheral artery disease (PAD) is responsible for 12 to 15% of deaths in Europe[116]. The Spectrum ranges from asymptomatic or intermittent claudication to necrosis and limb loss[117]. The primary clinical emergency is represented by acute limb ischemia (ALI), a sudden decrease in limb perfusion. The clinical presentation is considered acute if it occurs within 14 days after symptom onset[118, 119]. The insufficient time for new blood vessels reformation to compensate for the loss of perfusion makes a dangerous condition for limb viability. In contrast with critical limb ischemia (CLI) or chronic limb-threatening ischemia (CLTI), in which collateral blood supply is often present[118].

The incidence of ALI is approximately 1.5 cases out of 10,000 people per year, and high compliance risks, such as mortality and amputation, are between 10 and 15%[119-121].

Urgent recognition and intervention are requested to preserve limb viability as soon as possible. Many patients can also suffer from skeletal muscle necrosis, compartment syndrome, and multi-organ failures and loss of muscular function due to the reperfusion of the ischemic skeletal muscle.

1.6.1 Etiology

ALI can result from a range of causes, such as arterial embolism (30%), arterial thrombosis due to plaque progression and compliance (40%), thrombosis of a popliteal aneurysm (5%), trauma (5%), or graft thrombosis (20%)[117, 122]. The acute

decrease in limb perfusion is correlated to potential embolic causes, such as cardiac and aortic embolization, thrombosed graft, ergotism, hypercoagulative states, paradoxical venous-to-arterial embolism, and iatrogenic complications related to endovascular procedures[118].

1.6.2 Risk factors

Several risk factors can contribute developing or exacerbating limb I/R injury. The most critical comorbidities are coronary artery disease, a history of stroke, diabetes, and chronic renal failure[123]. Advancing age, male gender, and genetic factors are significant factors that cannot be preventatively addressed[123, 124]. Nevertheless, other important risk factors can be modified or controlled, such as obesity, metabolic syndrome, diabetes mellitus, hypertension, hyperlipaemia, physical inactivity, and tobacco smoking[123]. Disorders of collagen formation and vascular inflammation (vasculitis) may also lead to PAD by causing loss of structural integrity and dilatation of the arteries[125]. Coagulation disorders caused by abnormalities in the blood clotting system may contribute to thrombosis and increase the risk of reperfusion injury[126]. Also, medications that affect blood clotting or inflammation could increase the risk of I/R injury.

1.6.3 Symptoms

Symptoms range from the onset or worsening intermittent claudication to severe rest pain, paraesthesia, muscle weakness, paralysis, and in severe cases, gangrene. Symptoms manifest in several minutes, to hours or days. The clinical features of ALI are grouped into 6 points, “ 6 Ps”: pain, pallor, paralysis, pulse deficit, paraesthesia, and poikilothermia[127]. However, the diagnosis cannot be excluded if all of these features are absent. Differentiation of thrombotic versus embolic causes can be difficult[128]. In general, sudden-onset development of ischemic symptoms (due to the absence of collateral vessels) in a patient who was previously asymptomatic is most considered with an embolus, and sudden worsening symptoms in a patient with a history of CLTI with limb revasculation and claudication is more indicative of arterial thrombosis[129]. The severity of ALI is grated according to the Rutherford classification (Figure 4), and it is important

because evaluation, treatment, and prognosis depend on the degree of ischemic tissue damage[130]. The degree of severity is based on physical examination: skin colour, venous filling, and motor, and sensory function[130]. It also includes the evaluation of arterial and venous flow signals using a Dopper device.

Category	*Description/prognosis*	*Findings*		*Doppler signals*	
		Sensory loss	*Muscle weakness*	*Arterial*	*Venous*
I. Viable	Not immediately threatened	None	None	Audible	Audible
II. Threatened					
a. Marginally	Salvageable if promptly treated	Minimal (toes) or none	None	Inaudible	Audible
b. Immediately	Salvageable with immediate revascularization	More than toes, associated with rest pain	Mild, moderate	Inaudible	Audible
III. Irreversible	Major tissue loss or permanent nerve damage inevitables	Profound, anesthetic	Profound, paralysis (rigor)	Inaudible	Inaudible

Figure 10. Rutherford classification use to describe lower extremity ischemia.

1.6.4 Diagnostic test

For the high amputation and mortality rates, patients with suspicion of ALI must go imminently in Emergency. Immediately, anticoagulant treatment with heparin prevents thrombus progression and preserves microessels[131]. Analgesic treatment is often necessary. Coagulative tests, electrolyte panels, and total creatine kinase (CK) should be performed. Auscultation of the heart, chest X-ray, and electrocardiography are mandatory in every patient to identify intracardiac thrombus or cardiac diseases. Non-invasive images are performed in patients with viable (stage I) or marginally threatened (stage IIa) limbs to determine the location and extent of the obstruction.

1.6.5 Vascular imaging

Vascular imaging is important to evaluate the severity and disposition of ischemic injury. Different techniques can be used:

- Duplex ultrasound (DUS): is widely available and non-invasive for the patient, takes a relatively short time to take the images, and has a low cost. DUS is useful for assessing anatomic location, obstruction degree, and hemodynamic information[132].
- Computed tomography angiography (CTA) and magnetic resonance angiography (MRA): are high-resolution imaging tools. CTA and MRA have excellent sensitivity and specificity, and the monitoring of blood vessels could be investigated with a contrast medium injection (e.g. Gadolinium)[133].
- Invasive angiogram (DSA): is an invasive procedure with a potential risk of complications[134].

1.6.6 Therapy

Different types of intervention can be applied to an ischemic injury, either endovascular or surgical (thrombectomy, bypass, and arterial repair). The therapeutic strategy will depend on different parameters, such as type of occlusion (thrombus or embolus), location, Rutherford class, duration of ischemia, co-morbidities, therapy-related risk and outcomes[135].

1.6.6.1 Endovascular techniques

The endovascular approach is based on the usage of a catheter to restore the blood flow, as quickly as possible, to the ischemic limb, with the use of drugs, medical devices, or both.

1.6.6.2 Open surgery

The surgical approach is preferred in patients with ischemic symptoms for over 2 weeks or with a nonviable limb, bypass graft with suspected infection, or contraindication to thrombosis. The most used surgical technique includes thrombectomy with a balloon catheter, bypass, surgery, and adjuncts such as endarterectomy, patch angioplasty, and intra-operative thrombolysis. The combination of these approaches is frequent[136].

1.6.7 Reperfusion injury

The tissue injury response after reperfusion is directly correlated with the duration of the ischemia. Indeed, prolonged and severe ischemia induces inflammation, tissue dysfunction, and cell death that is exacerbated by reperfusion. However, short cycles of ischemia events are protective, rendering tissues resistant to the effects of prolonged ischemia followed by reperfusion via activation of intrinsic cell survival program (adaptive response)[96]. Nevertheless, restoration of blood flow to the affected organ at the earliest time possible is obviously of prime importance. Reperfusion results in the release of products of cell death, including potassium, phosphate, and myoglobin. Kidney injury could be associated with the production of toxic metabolites. Prefund limb swelling, with a high increase in compartmental pressure, is the trademark of this phenomenon[93]. Thrombosis could be complicated with compartment syndrome, and surgical fasciectomy is indicated to prevent irreversible neurological and soft-tissue damage.

1.6.8 Systemic inflammation and remote organ injury

Ischemic and reperfusion injurie occurs primarily locally, but with the post-revascularization the mediators can infiltrate in the systemic circulation and influence other remote non-ischemic organ system. This event is called distant or remote organ injury (ROI), and can be caused by ROS, leukocytes, and inflammatory mediators[137].

1.6.9 Post procedure and follow-up care

A successful treatment is suggested with the restoration of palpable pulse, audible arterial Dropper signals, and observable enhancement of perfusion level. Following the revascularization procedure, it is important to evaluate dorsiflexion of the foot and sensory function to identify potential signs of compartment syndrome. If the perfusion is incomplete, monitoring is important. Anticoagulative and vitamin K antagonist drug could be prescribed to prevent future events[138].

2 AIM OF THE PROJECT

In this thesis project was evaluated the regenerative potential of the human vascular fraction combined with 2% auto-crosslinked hyaluronic acid in a pathological model of skeletal mouse ischemic reperfusion injury.

The *in vitro* characterization of SVF was performed to elucidate its potential mechanism of action. Furthermore, both *in vitro* and *in vivo* assessments of SVF with three different hyaluronic acids enabled the identification of the formulation with the highest regenerative potential.

3 MATERIALS AND METHODS

3.1 Characterization of the Stromal Vascular Fraction

3.1.1 Adipose tissue collection

Adipose tissue was obtained from 27 women undergoing liposuction for aesthetic purposes, aged between 41 and 69 years. Prior to adipose tissue collection, informed consent was obtained in adherence to the ethical guidelines set by the review committee for human studies at AOU "Ospedali Riuniti," Ancona, Italy (Micro-adipose graft_01, May 18, 2017). In summary, Klein tumescence solution (2% Lidocaine solution: 0.08% w/v; Adrenaline 1mg/mL solution: 0.1% v/v in 0.9% saline) was administered, and liposuction commenced after a 10-minute interval. A cannula with 11 G, 6 holes, and a 20 ml Vac-Lock syringe provided with the Hy-Tissue SVF kit was used to lipoaspirate approximately 30 ml of fat from each donor's abdominal area. The collected fat was transported to the laboratory in an adiabatic container and processed within 18 hours of harvest.

3.1.2 Mechanical treatment of adipose tissue

Each adipose tissue sample (approximately 30 ml ± 5 ml) was decanted to remove excess oil and divided into two portions. The first portion of the lipoaspirate samples was mechanically processed using the Hy-Tissue SVF kit (Fidia Farmaceutici, Abano Terme, Italy) and the second one was enzymatic treated (see details in the paragraph 3.1.3). The kit consists of a sterile, single-use, double bag, including an inner filter bag with a mesh size of 120 µm. A volume of 25-30 ml of lipoaspirate was introduced into the inner porous bag using an upper syringe. After placing the kit vertically to remove excess Klein solution, the adipose tissue was manually processed for 5 minutes with the plastic rod located within the microporous bag. The micro-fragmented tissue was then collected through a syringe in the lower part of the outer bag and centrifuged at 1200 x g for 10 minutes. The cellular pellet obtained, called stromal vascular fraction (SVF), was resuspended in a complete culture medium

consisting of Dulbecco's modified Eagle's Medium (DMEM), 10% health-inactivated fetal bovine serum (FBS), 100 U/ml penicillin, 100 µg/ml streptomycin and 0,3% amphotericin B (all from GibcoBRL/Life Technologies, Milan, Italy). The product obtained through this method was referred to as "Hy-Tissue Stromal Vascular Fraction (SVF)".

3.1.3 Enzymatic treatment of adipose tissue

The second portion of lipoaspirate (5 ml) was processed with the following standard enzymatic procedure as reported in Dai Pre et al.[139]: the extracellular matrix was digested at 37°C in Hank's balanced salt solution (HBSS) with 1 mg/ml collagenase type I and 2% w/v of bovine serum albumin (BSA) (all from GibcoBRL/Life Technologies, Milan, Italy). After 45 minutes of incubation, enzymatic activity was neutralized with complete culture medium and centrifuged 1200 x g for 10 minutes. The pellet was incubated at room temperature for 10 minutes to lysate contaminating red blood cells with red blood lysing solution (Miltenyi Biotec, Germany), centrifugated then resuspended in complete culture medium as reported in 3.1.2. The product obtained through this method was designated as "Fat-enzymatic digestion (FAT-ED)".

3.1.4 Enzymatic treatment of stromal vascular fraction

Adipose tissue from N = 5 patients was only mechanically treated with Hy-Tissue SVF kit as reported in 3.1.1. A portion of each SVF product was reserved for proliferation capacity and CFU-F evaluation of SVF fraction, while the remaining was centrifugated at 1200 x g for 10 minutes. The resulting cellular pellet was digested at 37°C in HBSS with 1 mg/ml collagenase type I and 2% w/v BSA, as previously described. After 45 minutes, enzymatic activity was neutralized with complete culture medium and centrifuged. The product obtained through this process was designated as "Stromal Vascular Fraction-Enzymatic Digestion (SVF-ED)".

3.1.5 Cellular yield viability

Cellular viability was calculated by dividing the total amount of free cells obtained following each treatment (SVF, SVF-ED or FAT-ED) by the volume of processed fat, excluding the Klein solution. Free cells number was determined with trypan blue dye exclusion assay using CytoSMART counter (Automated Image-Based Cell Counter, version 1.5.0.16380, CytoSMART Technologies B.V, Eindhoven, The Netherlands).

3.1.6 Cellular proliferation capacity

The cellular proliferative capacity was determined by counting the number of days required to achieve cellular confluence. Briefly, 2 x 10^5 free cells for each treatment (SVF, SVF-ED, or FAT-ED) were cultured in T-25 cm^2 flasks (in triplicate) with complete cell medium and incubated at 37°C with 5% CO_2 until reaching 95% confluence. Additionally, the cellular growth capacity was estimated through the population doubling time assay: 5 x 10^4 free cells for each treatment (SVF, SVF-ED, or FAT-ED) were plated in T-25 cm^2 flasks (in triplicate) with complete culture medium and incubated at 37°C with 5% CO_2. After 24, 72, and 96 hours of incubation, the cells were trypsinized (0.05% trypsin at 37 °C for 5 min, GibcoBRL/Life Technologies), harvested and counted using the CytoSMART counter (Automated Image-Based Cell Counter, version 1.5.0.16380, CytoSMART Technologies B.V, Eindhoven, The Netherlands). The population doubling time (PDT) was calculated using the following equation: PDT = [t(h) * log2] / log (Nf/Ni), where Ni and Nf represent the initial and final cell numbers, respectively.

3.1.7 Colony forming unit assay

The Colony Forming Unit (CFU) assay was performed to assess the colony-forming capacity of cells. Three aliquots of 1 × 10^3 and 5 × 10^3 SVF, SVF-ED, or FAT-ED cells for each patient were seeded in 6-wells plate, and after 14 days of culture the number of adherent cells was estimated by colony forming unit fibroblast (CFU-F) count. The colonies were stained with Toluidine Blue (Sigma-Aldrich, Milan, Italy) and only the colonies macroscopically visible as

blue spot were counted. The number of CFU-F within SVF, SVF-ED, or FAT-ED cells was expressed as a percentage of total seeded cells.

3.1.8 Morphological and ultrastructural evaluation

Pellets obtained from Hy-Tissue SVF kit (N = 8) were morphologically analysed with whole-mount method (Larsen PL 1989) and hematoxylin and eosin paraffin embedding.

One set of pellets (N = 4) were stained with toluidine blue (Bio-Optica, Milan, Italy), and directly mounted on slides without dissection.

Another set of SVF pellets (N = 4) were fixed in 10% formalin (Sigma-Aldrich, Milan, Italy) for 4 hours, dehydrated to xylene, and embedded in paraffin. Sections of 7 μm thickness were cut with a microtome (Leitz 1512, Wetzlar, Germany) and stained with hematoxylin and eosin (Bio-Optica, Milan, Italy). All samples were examined using an Olympus BX51 microscope (Olympus, Tokyo, Japan) equipped with a digital camera (DKY-F58 CCD JVC, Yokohama, Japan). Digital images were analysed using Image-ProPlus 7.0 software (Media Cybernetics, Silver Spring, MD, USA).

For ultrastructure evaluation, scanning electron microscopy (SEM) analysis was used. Briefly, SVF pellets (N = 4) were fixed with glutaraldehyde 2% in 0.1 M phosphate buffer (Sigma-Aldrich, Milan, Italy), postfixed in 1% osmium tetroxide (Sigma-Aldrich, Milan, Italy), and dehydrated in graduated acetone concentrations (Sigma-Aldrich, Milan, Italy). The samples were treated with a critical-point dryer (CPD 030, Balzers Vaduz, Liechtenstein), fixed to stubs with colloidal silver, sputtered with gold by a MED 010 coater (Balzers), and examined with an XL30 ESEM scanning electron microscope (FEI Company, Eindhoven, Netherlands).

3.1.9 Immunophenotyping

Expanded cells from SVF and FAT-ED products at passage 4^{th} were characterized by flow cytometry. For this purpose, SVF and FAT-ED products were passed through a 45 μm cell strainer to remove cellular aggregates. Twenty

thousand cells were washed with PBS and incubated with the specific monoclonal antibody at 4°C for 30 min. After incubation, the cells were centrifuged and resuspended in PBS. CD29 (APC conjugate, 1:5 dilution), CD34 (PE conjugate, 1:5 dilution), CD44 (BV785 conjugate, 1:20 dilution), CD45 (FITC conjugate, 1:20 dilution), CD68 (FITC conjugate, 1:20 dilution), CD73 (BV421 conjugate, 1:20 dilution), CD90 (APC conjugate, 1:5 dilution), CD105 (PerCP-Cyt5.5 conjugate, 1:20 dilution), CD116 (FITC conjugate, 1:20 dilution), and CD146 (APC conjugate, 1:20 dilution) monoclonal antibodies were used (all from BD Biosciences, Becton Dickinson Italy S.P.A., Milano, Italy). Cell viability was also evaluated with propidium Iodide (PI). At least 10,000 events were analysed by flow cytometry (FACScalibur, Becton Dickinson) using the Cell Quest software. Moreover, a white blood cell differential (WBC diff) count was performed with ADVIA 120 haematology analyser (Bayer Diagnostics, Berkshire, Newbury, UK). The WBC were divided into four main cell subpopulations, corresponding to neutrophils (NEUT), lymphocytes (LYMPH), monocytes (MONO), eosinophils (EO), basophils (BASO), were counted in a separate channel.

3.1.10 *In vitro* differentiation assay

Adipose derived stem cells at passage 4^{th} from SVF and SVF-ED were used for the evaluation of the differentiation potential. Adipogenic differentiation was induced by exposing 7000 cells on a 6-well plate to adipogenic differentiation medium (Sigma-Aldrich, Milan, Italy) for 16 days. Then, cells were fixed with 4% paraformaldehyde for 30 min at 4 °C and then stained with Oil Red O (Bio-Optica, Milan, Italy) and hematoxylin (Bio-Optica, Milan, Italy). For chondrogenic differentiation, 1×10^6 cells resuspended in 5 µl of complete culture media were seeded in a 24-well plate, and after 2 hours, the chondrogenic media was added (StemPro chondrogenic differentiation Kit - GIBCO Life Technology, Monza, Italy). Fourteen days later, chondrocyte–specific markers and extracellular matrix production were evaluated using Alcian Blue and Fast Red staining (Sigma-Aldrich, Milan, Italy). For osteogenic differentiation, 5×10^3 cells were seeded on a 12-well plate and were treated

with osteogenic media (StemPro osteogenesis differentiation Kit–GIBCO Life Technology, Monza, Italy). After 21 days, osteoblast–specific marker and mineralization were assessed using Alizarin Red staining. Images were obtained using optical Olympus BX51 microscope (Olympus, Tokyo, Japan) equipped with a digital camera (DKY-F58 CCD JVC, Yokohama, Japan).

3.2 Hyaluronic acids

Hyaluronic acids of three different chemical characteristic were used:

HyA1: HyMovis, modified (derivatized)-HyA (500-730 kDa). The hydrogel Hymovis® consists of an 8 mg/ml formulation in phosphate buffer solution (PBS) of HYADD®4, the novel HyA derivative where 2–3% of the disaccharide repeating units have been modified by introducing hexadecylamine as a side-chain on the CDI-activated carboxyl group of the glucuronic unit[140, 141].

HyA2: Hyalubrix, linear unmodified HyA (1500-3200 kDa). The hydrogel Hyalubrix® is a 1.5% solution of non-modified Hya (15 mg/ml) obtained by biofermentation with molecular weight in the range 1500-2000 kDa[141, 142].

HyA3: Ial-System ACP, 2 % self-crosslinked HyA (200 kDa). Ial-System ACP hydrogel is inter- and intra-molecular esters of hyaluronan in which the carboxyl group is estrificated with hydroxyl groups of the same and or different molecules of the polysaccharides[143]. Briefly, 200kDA tetrabutyl ammonium salt of HA (HATBA) was dissolved in N-Metyl-2-Pyrrolidone (NMP) with 2-chloro-1-methylpyrinium iodide (CMMPI), which promotes the formation of intra- and intermolecular ester bounds between the carboxyl and the hydroxyl groups of the HA chains[143].

3.3 Hyaluronic Acid *in vitro* response

3.3.1 MMT assay

1 x 10^4 Adipose Derived–Mesenchymal Stem Cells (AD-MSCs, passage 4^{th}) were seeded in 96 well plates and incubated for 24 hours at 37°C in humidified air with 5% CO_2. The complete culture medium was then replaced after 24 hours

with fresh medium (DMEM with 10% FBS) containing different concentrations (0-7-15-25% v/v) of each hyaluronic acid (HyA1, HyA2, HyA3). Cytotoxicity was assessed through the MTT (3-(4,5-dimethylthiazol-2-yl)-2,5-diphenyltetrazolium bromide) assay after 72 hours of incubation. Then, 100 µl of MTT solution (5 mg/ml, Sigma-Aldrich, St Louis, USA) was added to each well and incubated for 4 hours. The MTT solution was removed, and 100 µl of DMSO was added to each well to dissolve the formazan crystal. Absorbance was read using an HTX microplate reader (BioTek Instruments, Winooski, VT, USA) at a wavelength of 570 nm. Eight measurements of optical density (OD) were recorded for each sample, and percentage of cell viability (CV) was calculated with the following equation: CV = (ODsample/ODcontrol) × 100.

3.3.2 *In vitro* adipogenic stimulation

The highest non-toxic concentration of each hyaluronic acid was used to perform an adipogenic stimulation assay. AD-MSCs (passage 4^{th}) were seeded on a 12-well plate and incubated with a complete culture medium for 24 hours at 37°C and 5% CO_2. After verifying that the cells were adherent, the highest non-toxic concentration of each hyaluronic acids were added to the medium, and the AD-MSCs were left in culture for 7, 14, 21 and 28 days. Two types of controls were used: positive control with adipogenic differentiation medium and negative control with standard complete culture medium. At the end of each time point, the cells were stained with Oil-Red-O (Bio-Optica, Milan, Italy). The degree of adipocytic differentiation achieved with the different hyaluronic acids was assessed through a semi-quantitative analysis of the absolute number and average area of formed lipid droplets within the cytoplasm of AD-MSCs. Each condition was measured in triplicate and five images per well were acquired, for a total of fifteen Regions of Interest (ROI) per experimental group. The images were acquired with an optical Olympus BX51 microscope (Olympus, Tokyo, Japan) equipped with a digital camera (DKY-F58 CCD JVC, Yokohama, Japan) with a 20x magnification (200 times magnification). Each image was quantified and analysed using Photoshop and ImageJ software.

3.4 *In vivo* regenerative potential of Hyaluronic Acids and Stromal Vascular Fraction

3.4.1 Therapeutic/treatment preparation/therapeutic strategy development

The harvested lipoaspirate (n = 5) was collected and transported as previously described (chapter 3.1.1). A volume of 60 ml of adipose tissue was divided into 4 fractions of 15 ml each. Every portion was individually mechanically treated with Hy Tissue SVF kit for 5 minutes, and after centrifugation (1200 x g for 10 minutes), each cellular pellet obtained was resuspended in 50 µl PBS. Three cellular pellets were mixed with 200 µl of the different types of hyaluronic acids (HyA1, HyA2, HyA3) at passage 0 (P0).

3.4.2 Animals

For *in vivo* regenerative evaluation, 25 Balb/c nu/nu male mice (BALB/cOlaHsd-Foxn1nu, Envigo, Bresso, Italy), 6-8 weeks old, were used. Mice were maintained under standard environmental conditions (temperature, humidity, 12h/12h light/dark cycle, with water and food ad libitum) and veterinarian assistance in the University of Verona facility. Animal handling was performed following a protocol approved by the Animal Care and Use Committee of the University of Verona (Centro Interdipartimentale di Servizio alla Ricerca Sperimentale, CIRSAL) and by the Italian Ministry of Health, in strict adherence to the European Communities Council (86/609/EEC) directives, minimizing the number of animals used and avoiding their suffering. Animals were anesthetized by 1.5% isoflurane inhalation in a mixture of O_2 and air and received a subcutaneous injection on the right flank of the SVF in PBS with one of the three hyaluronic acids. The contralateral flank was used as a control, receiving injection of the corresponding hyaluronic acid without cells.

3.4.3 MRI analysis

Animals were monitored with a Bruker Biospin 7T scanner (Bruker Biospin, Ettlingen, Germany) MRI at 3, 7, 14, and 30 days post-injection. Animals were

placed in a prone position over a heated animal bed and inserted in a 3.5 cm internal diameter bird-cage coil under anesthesia (1.5% isofluorane in a mixture of O2 and air). To perform *in vivo* MRI, T2-weighted (T2w) fat suppression on and off images were acquired with TR = 5777 ms, TEeff = 39 ms, FOV = 3.40×3.05 cm^2, MTX = 256, slice thickness = 0.5 mm, and N slice = 45. A quantitative H-NMR spectroscopy was used to understand the chemical composition in the injected area.

3.4.4 Histological analysis

Animals were sacrificed at 3, 7, 14, and 30 days post-injection; their flanks were removed and fixed in 10% formaldehyde. After rinsing in 0.1 M phosphate buffer, specimens were dehydrated through an ascending series of ethanol, transferred to xylene, and embedded in paraffin wax. Serial 7 µm thick sections were cut on a rotative microtome (Leitz 1512, Germany), collected on polylysine-coated slides, and dried overnight at 37°C. The sections were stained with hematoxylin and eosin for the morphological evaluation and alcian blue fast red for glycosaminoglycans and mucopolysaccharides detection.

3.4.5 Immunofluorescent

Sections were deparaffinized, rehydrated with xylene, and a descending ethanol series. The sections were placed in a microwave oven at 600 W for three 5-minute cycles in antigen unmasking solution (Vector Laboratories, Burlingame, USA). After PBS washing, slices were blocked for 1 hour in 0,3% Triton X-100, 1% bovine serum albumin (BSA) in PBS; the same solution was used to dilute the antibody. Subsequently, sections were incubated overnight at 4°C with PE-anti-human HLA-DR (1:200, Sony Biotechnology, CA, USA). Finally, the sections were washed, reacted with Hoechst nuclei staining with 1:1000 PBS dilution, mounted with PPT aqueous mounting medium, and observed with a confocal laser scanning microscope (Leica TCS SP5 AOBS, Germany).

3.5 Metabolic activity, DNA content, and migration evaluation of Stomal Vascular Fraction and Hyaluronic Acid 3

3.5.1 Cellular metabolic-activity assay

To determine the metabolic activity of the expanded SVF cells with the HyA3 an alamar blue assay (ThermoFisher Scientific, Dublin, Ireland) was performed. The adherent SVF cells (n = 3 per group) were seeded in 48-well plates with complete growth medium and incubated at 37 °C in a humidified environment with 5% CO_2. After 24 hours, the cells were exposed to a concentration of 50% HyA3 and 50% complete growth medium. At 3, 7, and 14 days, 10% alamar blue viability reagent was added at 37°C for 1 h. A spectrophotometer (Victor2 D, Wallac, Boston, MA, USA) with an excitation wavelength of 550 nm and an emission wavelength of 590 nm was used to read the resulting fluorescence level. Half complete culture media and half HyA3 containing 10% alamar blue were used as a blank sample and subtracted to eliminate background fluorescence. The cellular metabolic activity of was evaluated at day 3, 7 and 14 was measured.

3.5.2 DNA quantification

To assess the DNA content of the expanded SVF cells in contact with HyA3, a Quant-iT™ PicoGreen® dsDNA assay kit (Invitrogen, Loughborough, UK) was used. Expanded SVF cells (n = 3 per group) were seeded in 48-well plates with complete growth medium and incubated at 37°C in a humidified environment with 5% CO_2. After 24 hours, the cells were exposed to a concentration of 50% HyA3 and 50% complete growth medium. At 3,7 and 14 days, adherent SVF cells were digested in a lysis buffer solution prepared with 0.2 M sodium carbonate and 1% triton X-100. A spectrophotometer (Victor2 D, Wallac, Boston, MA, USA) with an excitation wavelength of 485 nm and an emission wavelength of 538 nm was used to read the resulting fluorescence level. The DNA of cells grown in contact with HyA3, pretested for cellular metabolic activity, was quantified.

3.5.3 Scratch assay – cell migration

The spreading and migration capabilities of adherent SVF cells in contact with HyA3 were assessed using a scratch wound assay. SVF's adherent cells were seeded on a 24-well plate and fed with complete culture medium until a confluent monolayer of cells was present in the plate. Forty-eight hours before performing the scratch, all cells were FBS-deprived. Then, a linear wound was generated in the monolayer with a sterile 200 µl plastic pipette tip. Each of the wells was washed three times with PBS to remove the detached cells. Half HyA3 and half complete culture medium (n = 3 per group) was added and incubated at 37°C with 5% CO_2. The cells treated with only complete culture medium were used as a control. To evaluate cell migration, images at 20× magnification were taken at 0, 1, 2, 4, 8, 24, 36 h post-stretch using an inverted microscope (Leica DMIL, Leica Microsystems S.r.l., Buccinasco, MI, Italy) equipped with a camera (Optika Microscopes, Ponteranica, BG, Italy). The scratched area free of cells was measured in three randomly chosen fields, in three independent experiments, for a total of 6 fields per sample by ImageJ software. The value of the cell-free area was expressed as a percentage of the value at time 0 (considered as 100%).

3.6 *In vivo* pathological regenerative potential in a muscle ischemic reperfusion model

3.6.1 Animals

Animal handling was performed following a protocol approved by the Animal Care and Use Committee of the University of Verona (CIRSAL) and by the Italian Ministry of Health, in strict adherence to the European Communities Council (86/609/EEC) directives, minimizing the number of animals used and avoiding their suffering. 25 Balb/c nu/nu male mice (BALB/cOlaHsd-Foxn1nu, Envigo, Bresso, Italy), 6-8 weeks old were used. Mice were maintained under standard environmental conditions (temperature, humidity, 12h/12h light/dark cycle, with water and food ad libitum) and veterinarian assistance in the University of Verona facility. All mice were included in the following ischemia-

reperfusion (I/R) experiments. Isoflurane was delivered by face mask at a concentration of 2% for induction and then 1% for maintenance, along with continuous oxygen while the mice were kept on a heating pad to maintain the body temperature at 37°C. Ischemia was induced on the quadricipital level with a tourniquet application for 3 hours. Twenty-four hours post-ischemia-reperfusion (I/R) injury, mice were randomly divided in four groups and they received an intramuscular (quadricipital level) injection. The first experimental group received saline injection, the second HyA3, the third SVF, and the fourth SVF+HyA3, with a final treatment volume of 100 µl.

3.6.2 Rotarod Accelerod

A rotarod test was used to evaluate the motor coordinator of I/R injured mice. A rotarod machine with automatic timers and falling sensor (RotaRod, Ugo Basile s.r.l.) was used. A training rotarod test before accelerod test was performed to exclude differences in motivation and motor learning. During the training phase for 3 consecutive days each animal was placed on the rotarod at a constant speed (12 rpm) for a maximum of 120 sec, and the latency and frequency to fall off the rotarod within this time period was recorded. Subsequently, a horizontally suspended motorized rod that revolves around its axis at an increasing rotation speed from 4 rpm to 40 rpm for 5 minutes was used. The animals were tested in 3 trials per day with an interval of 30 minutes. Accelerod test was carried out at different time points: pre-I/R injury induction (baseline), 4, 7, and 15 days post-I/R injury (dpi). Latency and rotation speed at which the animals fell off the rod were recorded.

3.6.3 MRI

MR images were acquired using a Bruker Biospin 7T scanner (Bruker Biospin, Ettlingen, Germany). Animals were anesthetized using 1.5-2% isoflurane inhalation in a mixture of oxygen and air, placed in a heated animal bed, and inserted in a 3.5 cm internal diameter bird-cage coil. During the experimentation, breathing rate, and body temperature were monitored. T2-

weighted (T2w), T2-mapping, and Diffusion-weighted images (DWIs) were performed 4, 7, 14, and 18 days post-IRI.

Briefly, T2w were acquired using the following parameters: repetition time (TR) = 2653.998 ms, echo time (TE) = 33 ms, field of view (FOV) = 40 x 35 mm, matrix size (MTX) = 128 x 128, slice thickness = 1 mm, n° of slice = 25, number of averages = 2, for a total acquisition time of 1 min 24 sec.

T2-mapping images were acquired using a multislice multi-echo sequence with TR = 3000 ms, TE = 8 ms, FOV = 40 × 35 mm, MTX = 128 x 128, slice thickness = 1.5 mm, n° of slice = 15, number of averages = 2, number of echoes = 12, echo time = 8 ms, for a total acquisition time of 12 min 48 sec.

DWIs were acquired with an echo planar imaging (EPI) sequence with the following parameters: TR = 3000 ms, TE = 24.68 ms, FOV = 40 x 20 mm, MTX= 256 x 128, slice thickness = 1 mm, n° of slice = 15, number of averages = 4, segments = 25, b value = 900 s/mm^2 for a total acquisition time of 10 min.

Furthermore, a dynamic contrast-enhanced (DCE) MRI was performed at 3, 14, and 18 days post I/R injury. The DCE-MRIs were acquired with a rare acquisition with relaxation enhancement (RARE) sequences and the protocol consisted of the continuous acquisition of more dynamic multiple repetitions including 7 initial dynamic repetitions followed by the intravenous injection of Gadolinium-diethylenetriamine pentaacetic acid (Gd-DTPA,Magnevist, 0.1 mmol/kg) and the acquisition of 143 other dynamic repetitions. DCE-MRI sequences were acquired with the following parameters: TR = 120.715 ms, TE = 4.99 ms, FOV = 30 × 40 mm, MTX = 96 x 128, slice thickness = 1.5 mm, n° of slice = 5, number of averages = 2, echo spacing = 4.992 ms, rare factor = 4, for a total acquisition time of 14 min 50 sec.

3.6.4 Histology and immunohistochemistry

Animals were perfused with 4% paraformaldehyde in phosphate buffer solution at 18 days post-injection; their peripheral muscle (gastrocnemius and quadricipital) were removed, and transversal divided into two sections: one for histology and immunohistochemistry and the other one for transmission

electron microscopy. After rinsing in 0.1 M phosphate buffer, specimens were dehydrated through an ascending series of ethanol, transferred to xylene, and embedded in paraffin wax. Serial 7 μm thick sections were cut on a rotative microtome (Leitz 1512, Wetzlar, Germany), collected on polylysine-coated slides, and dried overnight at 37°C. The sections were processed for peroxidase immunohistochemistry, immunofluorescent, and hematoxylin and eosin staining for morphological evaluation.

3.6.4.1 Immunohistochemistry

The sections were deparaffinized, rehydrated with xylene and a descending ethanol series, and then stained using immunoperoxidase, using the avidin–biotin complex (ABC, Vector Laboratories, Burlingame, CA, USA) technique. Briefly, the sections were placed in a microwave oven at 600 W for three 5-minutes cycles in antigen unmasking solution (Vector Laboratories, Burlingame, USA). Endogenous peroxidase activity was inhibited by immersion in a solution of 0,3% hydrogen peroxide in methanol for 30 minutes. After washing in PBS, the slices were incubated for 45 minutes with Boxall blocking solution (Vector Laboratories, Burlingame, USA). Primary antibodies were applied on the slice overnight at 4°C, as indicated in Table 1. Processed sections void of primary antibodies were used as negative controls.

Antibody	**Dilution**	**Source**
Fast myosin (MyoF)	1:8000	Mouse source, Sigma-Aldrich
Slow myosin (MyoS)	1:1000	Mouse source, Sigma-Aldrich
Desmin	1:80	Mouse source, GeneTex, USA
Pax7	1:200	Rabbit source, Abcam, UK
CCL5	1:1000	Rabbit source, Bioss antibodies

Table 1. Primary antibodies dilution and source.

After washing, the sections were then reacted with biotinylated secondary antibody (anti-rabbit and anti-mouse antibody diluted 1:200) for 1 hour at room temperature. The immunoreaction was identified using a VECTASTAIN Elite ABC kit (Vector Laboratories, Burlingame, CA, USA) and then marked with 3,3′-diaminobenzidine tetrahydrochloride (Dako, Milan, Italy) for 3 minutes. Finally, the sections were dehydrated, coverslipped with Entellan (Merck, Kenilworth, NJ, USA), and observed in an Olympus BX51 microscope equipped with a KY-F58 CCD camera (JVC).

3.6.4.2 Morphological evaluation

The slices were incubated with a hematoxylin solution for 30 seconds. After washing with tap water, the sections were stained with eosin (all Bio-Optica, Milan, Italy) for 10 seconds and washed with distilled water. The sections were dehydrated, coversipped with Entelan, and observed using an Olympus BX51 photomicroscope equipped with a KY-F58 CCD camera (JVC).

3.6.4.3 Oil Red O staining

Oil Red O (ORO) staining was used to evaluate the presence of lipids in skeletal muscle tissue. Slices were deparaffinized, rehydrated with xylene and a descending ethanol series, and stained in Oil Red O solution (Bio-Optica, Milan, Italy) for 20 minutes. After washing in tap water, muscles were counterstained with Mayer's hematoxylin, washed in tap water and mounted with an aqueous medium (Bio-Optica, Milan, Italy). Quantification of area covered by Oil Red O staining was performed on digital images acquired with the same objective (40x) of the optical Olympus BX51 microscope equipped with a KY-F58 CCD camera (JVC). 3 digital images per zones (superior medial gastrocnemius, inferior medial gastrocnemius, superior lateral gastrocnemius, inferior lateral gastrocnemius, plantaris) were randomly selected in both control and treated grouped. Post-processing of the images was carried out using a custom MATLAB script (Matlab R2023a, MathWorks, MA, USA). In brief, images underwent deconvolution, and a threshold was applied to the channel of

interest. The area occupied by positive pixels was quantified and converted into μm^2.

3.6.4.4 Analysis of fiber area

The post-processing evaluation of the images was conducted utilizing a custom script developed in MATLAB software (MATLAB R2023a, MathWorks, MA, USA). In summary, RGB histological images of muscles were first converted into Lab* colour space. Subsequently, a threshold was established based on the histogram settings for each channel, followed by the creation of a corresponding mask. Background noise was eliminated from the resultant black and white (BW) image. To mitigate over-segmentation, a common issue with raw watershed transforms, a "minima imposition" technique was employed to filter out small local minima. A distance transform was subsequently applied to generate an image capable of identifying catchment basins, followed by the application of a watershed transform. The Area property was then extracted and converted into square micrometers (μm^2) for each independent region.

3.7 Characterization of human adipose tissue supernatant obtained by Stromal Vascular Fraction

The supernatant phase of human adipose tissue after mechanical fragmentation with Hy-tissue SVF kit was used for analysing the content of extracellular vescicles (EVs). After centrifugation (3500 rpm for 7 min), the supernatant phases were filtered through a 0,22 µm nylon mesh to remove cell debris. All the samples were aliquoted and frozen at -20 °C for the characterization.

3.7.1 NTA measurement

The EVs size distribution and concentrations were measured by nanoparticles tracking analysis (NTA) system (Nanosight NS300). All HT-SVF supernatant samples were correctly diluted in PBS to a final volume of 800 µl. For each measurement, three 1-min videos were captured under the following conditions: 25°C cell temperature, 20 µl/s syringe speed, 488 nm laser wavelength, and the setting acquisition parameters were set according to the manufacturer's

software (NanoSight NS300) in order to obtain the validation of the measurement. NTA 3.4 software (Malvern Panalytic) was used to acquire and analyse the sample videos. The results are reported as mean ± standard deviation of the mean of three measurements. For size determination, the data are reported as statistical mode ± standard deviation of the mean of three measurements.

3.7.2 Transmission electron microscopy (TEM)

For TEM analysis, 10 µl SVF supernatants were fixed in 2% glutaraldehyde in DNase/RNase-Free Distilled Water for 10 min on 150 mesh formvar carbon-coated copper grids (Societa Italiana Chimici, Rome, Italy) and dried under a hood. Samples were stained with lead citrate and the images were acquired with a Philips Morgagni 268 D electron microscope (Fei Company, Eindhoven, The Netherlands), equipped with a Megaview II camera for acquisition of digital images.

3.7.3 Cellular transmission electron microscopy

SVF cellular pellet were fixed in 2% glutaraldehyde in Sorensen buffer pH 7.4 for 2 h, post-fixed in 1% osmium tetraoxide (OsO4) in aqueous solution for 2 h, dehydratated in graded concentrations of acetone and embedded in Epon–Araldite mixture (Electron Microscopy Sciences, Fort Washington, PA, USA). The semi-thin sections (1 mm thickness) were examined by light microscopy and stained with toluidine blue. The ultra-thin sections were cut at 70 nm thickness and placed on Cu/Rh grids with Ultracut E (Reichert, Wien, Austria), stained with lead citrate and observed using Philips Morgagni 268 D electron microscope (Fei Company, Eindhoven, The Netherlands), equipped with a Megaview II camera for acquisition of digital images.

3.7.4 Purification

Exosomes were isolated from 2 ml SVF supernatant by PureExo® Exosome isolation kit (101Bio, CA, USA), following the manufacturer's protocol. Exosomes were directly stored at 4°C for up to 1 week or at 80 °C for 3 months. The protein content of the exosomes was determined by Bicinchoninic Protein

Assay (BCA method) using the manufacturer's protocol (Thermo Scientific™ Pierce™ BCA™ Protein Assay).

3.7.5 Western blot

Analysis of exosomes or microvesicles by immunoblotting was performed using the following protocol. Proteins are denatured, separated into 4-20 % polyacrylamide gels, transferred onto a polyvinylidene difluoride (PVDF) membrane, and probed with primary antibody, as indicated in Table 2. Human AD-MSCs lysates were used as a positive control.

Antibody	**Dilution**	**Source**
Alix	1:1000	Rabbit source, Abcam, UK, Cambridge
GM130	1:1000	Rabbit source, Abcam, UK, Cambridge
CD9	1:1000	Rabbit source, Abcam, UK, Cambridge
Calnexin	1:1000	Rabbit source, Abcam, UK, Cambridge
CD63	1:1000	Rabbit source, Abcam, UK, Cambridge
CD81	1:700	Rabbit source, Abcam, UK, Cambridge
HSP70	1:1000	Rabbit source, Abcam, UK, Cambridge
TSG101	1:1000	Rabbit source, Abcam, UK, Cambridge
CD40	1:1000	Mouse source, Abcam, UK, Cambridge
CD62L	1:1000	Rabbit source, Abcam, UK, Cambridge

Table 2. Primary antibodies dilution and source

After washing, the membranes were incubated with the appropriate horseradish peroxidase (HRP) conjugated secondary antibodies. The blots were then

incubated with a chemiluminescent HRP substrate and detected with G: BLOX F3 GeneSys (Syngene, UK).

3.8 Statistical analysis

Statistical analysis was conducted with Prism software (8, GraphPad Inc., La Jolla, CA, USA). All data reported were expressed as mean ± standard error of the mean (mean ± SEM/SD). A One or Two-way ANOVA test was applied to evaluate statistically significant differences The statistical significance level was placed at $p < 0.05$.

Muscle relaxation time (T2-rt), apparent diffusion coefficient (ADC), and signal intensity of Gd-DTPA over time were obtained from images using the ParaVision 6.0.1 software (Bruker Biospin, Ettlingen, Germany) compared treated I/R injury paw with the contralateral.

For DCE-MRI all the Gd-DTPA signal intensity points (143 total) over time were normalized to the average baseline values. Subsequently, the area under the curve (AUC) was calculated with MATLAB software.

T2-rt, ADC, and AUC of DCE-MRI were analyzed with GraphPad Prism 8.0.2 software.

4 RESULTS

4.1 Characterization of the Stromal Vascular Fraction

4.1.1 Morphological and ultrastructure analysis

Microscopic analysis of the stromal vascular fraction (SVF) pellet (Figure 11A) obtained after the mechanical fragmentation of adipose tissue with Hy-Tissue SVF kit detected the presence of free cells (Figure 11B) and micro-fragments of stromal connective tissue (Figure 11C). Heterogeneous cellular components with different morphology, size, and shape (Figure 11B black stars) were observed. The micro-fragments exhibited an elongated cylindrical morphology, with an average diameter of 30 to 70 μm and variable lengths. These fragments displayed a fibrinoid arrangement with tubular structures (stained in deep purple), indicating the presence of preserved microvascular elements consistent with capillaries of varying lengths containing endothelial and perivascular cells (Figure 11D, E). The composition of the SVF pellet was also supported by the scanner electron microscopy (SEM) images (Figure 11F, G, H), in which the dense connective tissue formed by isolated and coarse bands of collagen fibers (Figure 11F, G) containing adherent cells was observed. Furthermore, SEM images depicted the existence of adipocytes (Figure 11H) characterized by their small size (10–20 μm), indicative of adipocytes that have either lost their lipid content or have not undergone complete differentiation.

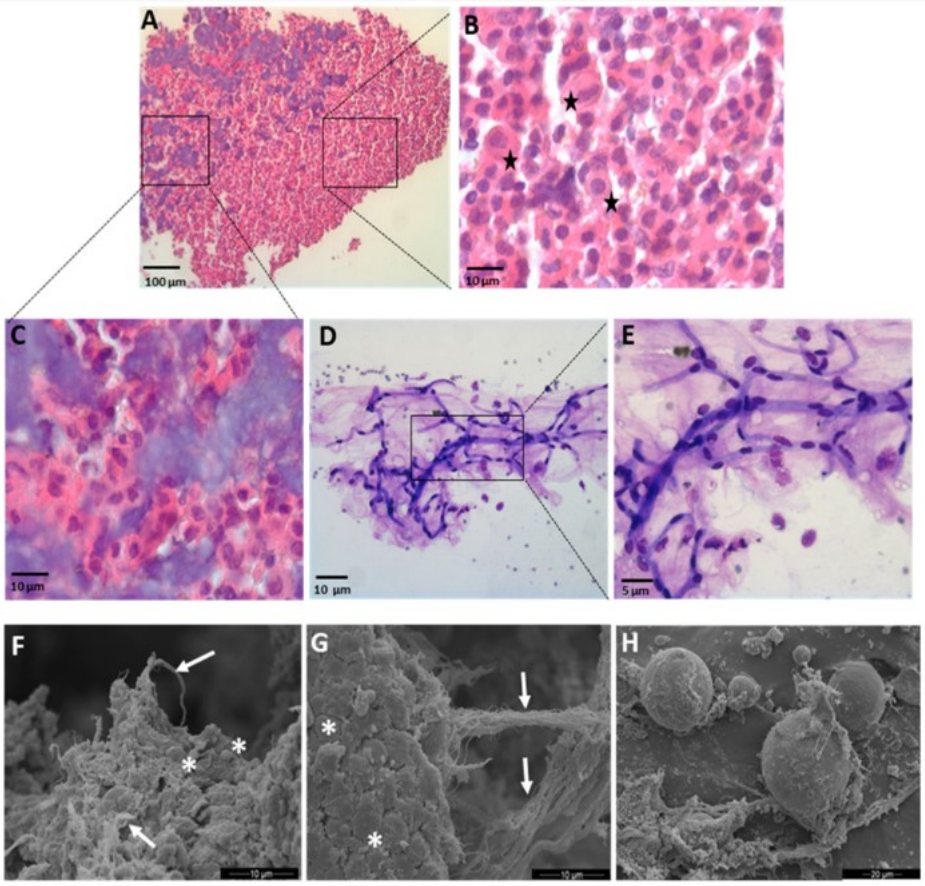

Figure 11. Morphological and ultrastructural analysis of Hy-Tissue SVF product. (**A, B, C**) Light microscopy of a pellet single-layer section stained with hematoxylin and eosin. The black stars indicated cellular heterogeneity. The square indicated the location of the higher magnification images. Scale bar, 100 µm (A) and 10 µm (B, C). (**D, E**) Light microscopy of a SVF pellet stained with toluidine blue relieved the presence of preserved microvascular elements that appeared as tubular structures. The square indicates the location of the higher-magnification image. Scale bar, 10 µm (D) and 5 µm (E). (**F, G**) SEM evaluation of SVF pellet revealed the presence of connective tissue micro-fragments. The arrows indicated collagen fibers, and asterisks adherent cells. Scale bar, 10 µm. (**H**) Small adipocytes were identified in the SVF pellet. Scale bar, 20 µm.

4.1.2 Quantitative assessment of cellular yield, CFU-F population and cellular proliferative capacity

A quantitative evaluation was conducted to assess the different mechanical and enzymatic methods for obtaining SVF. The cell yield of free nucleated cells in the SVF product was 4.1 x 10^4 ± 2.0 x 10^4 cells/ml fat (Figure 12A). When the SVF pellet underwent to collagenase enzymatic digestion, the resultant product (stromal vascular fraction-enzymatic digest, SVF-ED) demonstrated a notable increase, showing a 3.2-fold rise in the yield of free nucleated cells (1.3 x 10^5 ± 4.7 x 10^4 cells/ml fat, SVF vs SVF-ED $p<0.001$). On the other hand, the enzymatic treatment of adipose tissue (FAT-ED), used as the gold standard methodology, revealed a 12-fold increase in cell yield compared to mechanical treatment (5 x 10^5 ± 2 x 10^5 cells/ml fat, SVF vs FAT-ED $p<0.001$).

To assess the colony-forming ability of the SVF pellet, colony-forming unit fibroblast (CFU-F) assays were conducted (Figure 12C). The results indicated that the SVF CFU-F yield was 178 ± 49 CFU/ml fat, and after the enzymatic digestion, the CFU yield increased by over 2.4 times (424 ± 181 CFU/mL fat, $p=0.048$). FAT-ED CFU-F capacity was increased 27 times (4877 ± 2477 CFU/ml fat) with a statistically significant in comparison to the SVF pellet (SVF vs FAT-ED $p<0.001$). Furthermore, the frequency of CFU-F in FAT-ED was 5.6 times higher than that in the SVF product (FAT-ED: 1.7 ± 1.9%; SVF: 0.3 ± 0.2%; SVF-ED: 0.3± 0.1%, Figure 12D).

Finally, the days required to achieve cell confluence from SVF, SVF-ED, and FAT-ED was analysed to evaluate the cellular proliferative capacity (Figure 12E). There were no statistically significant differences between SVF and SVF-ED cells in reaching confluence (respectively 8 ± 2 days and 8 ± 1 day, respectively); instead, FAT-ED cells required less time (5 ± 2 days). The histograms illustrate that the doubling time of SVF and SVF-ED cells was comparable (59.35 ± 2.8 h and 57.38 ± 3.9 h, respectively), while cells from FAT-ED required less time to double their number (45.31 ± 3.95 h, SVF vs FAT-ED $p=0.014$, SVF-ED vs FAT-ED $p=0.037$; Figure 12F).

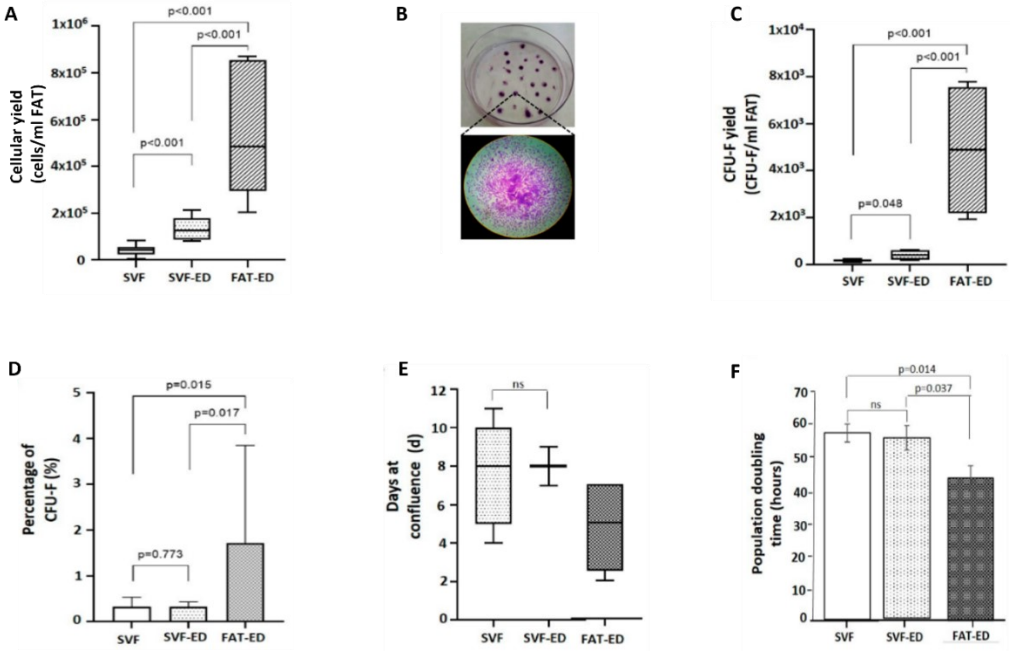

Figure 12. Cellular yield, CFU-F, and cellular proliferation capacity of SVF, SVF-ED, and FAT-ED. (**A**) Nucleated cellular yield showed a significant increase in FAT-ED and SVF-ED compared to SVF (SVF vs SVF-ED $p<0.0001$, SVF vs FAT-ED $p<0.0001$, SVF-ED vs FAT-ED $p<0.0001$). (**B**) Representative CFU-F assay in a cell culture dish stained with toluidine blue. The square indicated the location of the higher magnification images. 4x magnification. (**C**) CFU-F yields significant increase in the FAT-ED and SVF-ED compared to SVF (SVF vs SVF-ED $p=0.048$, SVF vs FAT-ED $p<0.001$, SVF-ED vs FAT-ED $p<0.0001$). (**D**) Percentage of CFU-F significant increase in the FAT-ED compared to SVF (SVF vs SVF-ED $p=0.773$, SVF vs FAT-ED $p=0.015$, SVF-ED vs FAT-ED $p=0.017$). Results were presented as the mean and error bar one standard deviation. (**E**) Proliferation capacity of cells in T-25 flasks with no differences between SVF, SVF-ED, and FAT-ED. Box and whisker plots represented the median, the lower and upper quartile, and the minimum and maximum. (**F**) Population doubling time of SVF significantly increased compared to FAT-ED (SVF vs SVF-ED $p=0.0014$, SVF-ED vs FAT-ED $p=0.037$). Mann-Whitney test was used to analyse the data, n=27.

4.1.3 Immunophenotyping

SVF composition was characterized by flow cytometry and compared with the enzymatic gold standard treatment (FAT-ED). The death cells positive for propidium iodide were excluded (Figure 13A). The CD34-positive cell population (endothelial, pericytes, and potential adipose-derived mesenchymal stem cells, AD-MSC) in SVF and FAT-ED was 9.9% ± 1.5% and 3.7 ± 1.3%, respectively (Figure 13B). Additionally, the frequency of cells positive for CD73 and CD105 (mesenchymal stem cells) was analysed (Figure 13C, D). The percentage of expression in SVF was 7.61 ± 2.59% and 6.28 ± 2.40% for CD73 and CD105, respectively, not thus far from the percentage of expression obtained for the same antibody with FAT-ED (10.14 ± 2.91% and 9.98 ± 1.49%, respectively).

To characterize the cellular SVF composition in terms of endothelial cells, monocytes, macrophages, and leukocytes, the percentage of CD146 (2.6 ± 0.2%), CD116 (0.7 ± 0.1%), CD68 (3.5 ± 1.5%), and CD45 (5.5 ± 1.34%) was evaluated (Figure 3E). Within the white blood cell (WBC) fraction, four main cell subpopulations were identified, and the percentage of expression for neutrophils, lymphocytes, monocytes, eosinophils, and basophils is depicted in Figure 13F.

SVF and FAT-ED expression of surface markers after cellular expansion of the adherent population were similar. As expected, most cells exhibited low CD45 expression while displaying positivity for MSC-associated markers such as CD105, CD90, CD73, CD29, and CD44 (Figure 13G).

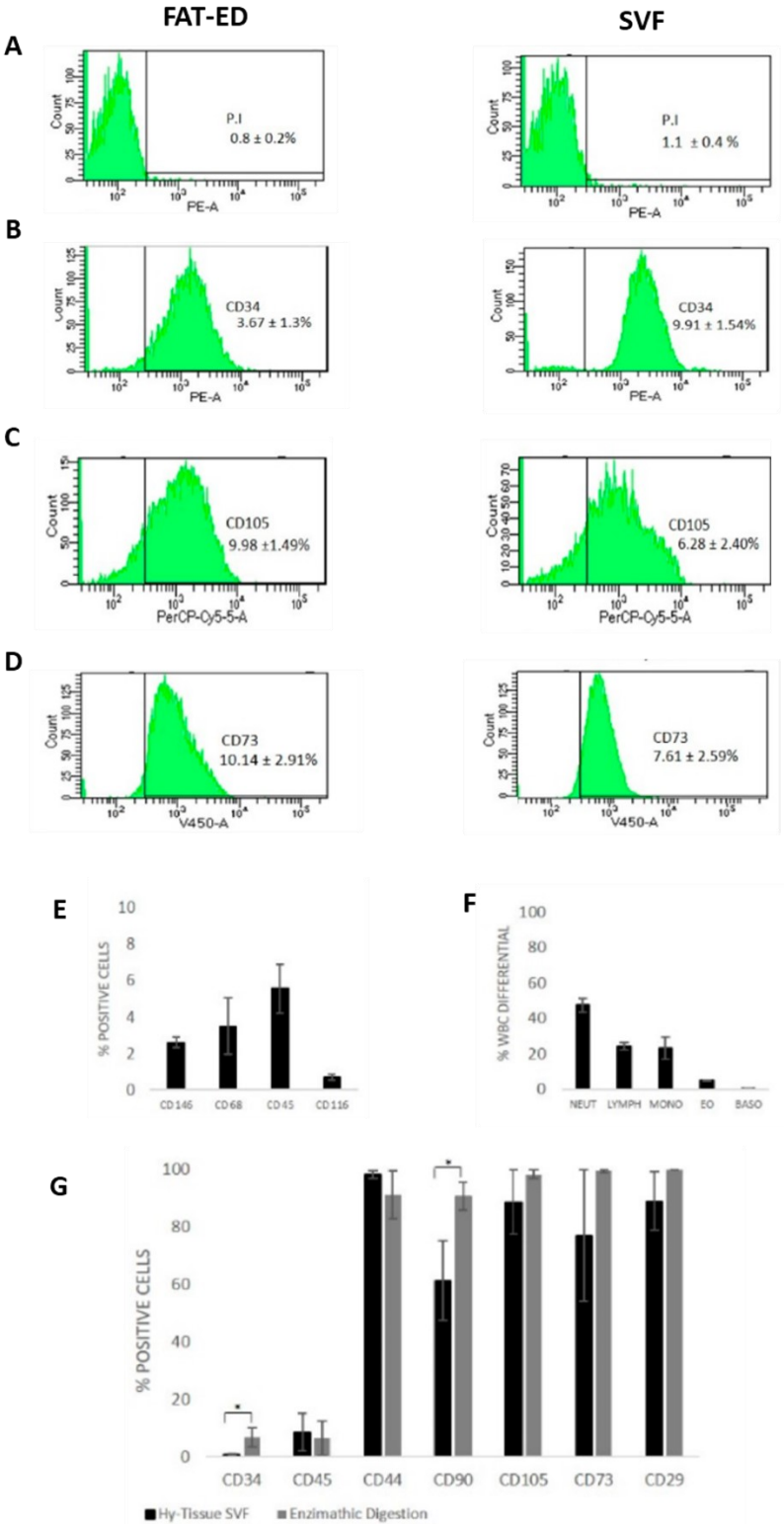

Figure 13. Expression of surface markers detected by flow cytometric analysis. (**A**) Positive cells marked with propidium iodide (FAT-ED= 0.8 ± 0.2%, SVF= 1.1 ± 0.4%). (**B**) Positive cells marked with CD34, were used for hematopoietic progenitor cells and small vessel endothelium. (**C**) Positive cells marked with CD105, were used for mesenchymal

stem cells. (**D**) Positive cells marked with CD73, were used for endothelial cells and stromal cells. (**E**) Positive SVF cells marked with CD146, CD68, CD45, CD116, were respectively used for endothelial cells, macrophages, lymphocytes, and monocytes. (**F**) Positive SVF cells were identified using white blood cells differential (WBC diff) to characterize neutrophils (NEUT), lymphocytes (LYMPH), monocytes (MONO), eosinophils (EO), and basophils (BASO). (**G**) The average number of positive SVF and FAT-ED cells after in vitro cellular expansion was marked with CD34, CD45, CD44, CD90, CD105, CD73, and CD29. Results were represented as the mean and error bars one standard deviation (* $p<0.05$).

4.1.4 *In vitro* differentiation assay

The multilineage differentiation potential of the SVF obtained with Hy-Tissue SVF was assessed by examining the capacity of SVF-expanded cells at passage 4th to differentiate into adipocytes, chondrocytes, and osteocytes (Figure 14). To eliminate peripheral blood contaminants and other non-adherent stromal cells in the SVF, cells were replated until passage 4th, retaining only adherent cells with a fibroblastoid morphology. The results of the multipotency assessment of the SVF product are shown in Figure 4. The expanded cells from FAT-ED were used as a control. Adherent cells obtained with Hy-Tissue SVF demonstrated the ability to differentiate into the three mesodermal lineages, similar to cells enzymatically extracted (FAT-ED). Positive staining for Oil Red O, Alizarin Red, and Alcian Blue compared to the control confirmed adipogenic, osteogenic, and chondrogenic differentiation, respectively.

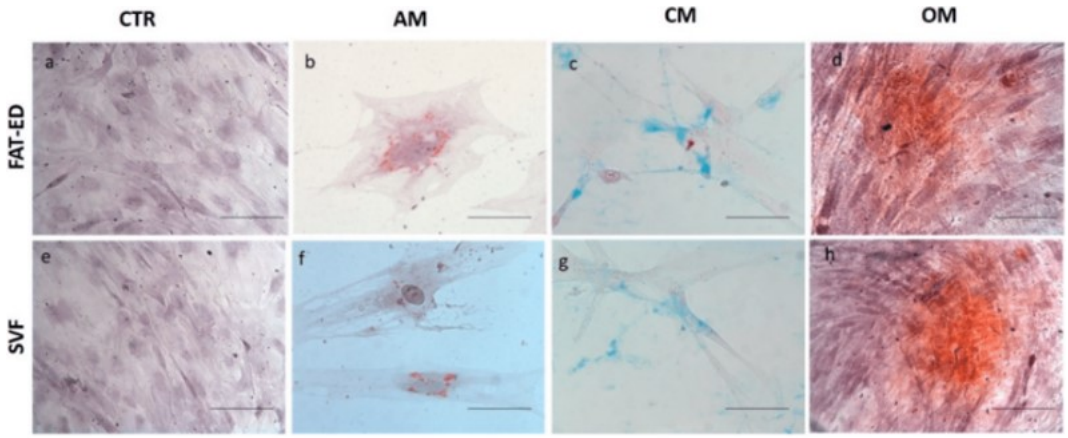

Figure 14. Multiage differentiation assay of SVF and FAT-ED passage 4th. (**A, E**) Light microscopy images of control SVF and FAT-ED cells (CTR). Scale bar, 100 µm. (**B, F**) Light microscopy images of SVF and FAT-ED cells induced to undergo adipogenic differentiation. Adipogenesis was indicated by the accumulation of cytoplasmatic lipid droplets stained with Oil Red O. Scale bar, 100 µm. (**C, G**) Light microscopy images of SVF and FAT-ED cells stimulated to differentiate into the chondrogenic lineage. Chondrogenesis was indicated by the formation of sulphated proteoglycan-rich matrix stained with Alcina Blue. Scale bar, 100 µm. (**D, H**) Light microscopy images of SVF and FAT-ED cells directed to differentiate into the osteogenic lineage. Osteogenesis was indicated by the formation of extracellular matrix calcification stained with Alzarin Red. Scale bar, 100 µm.

4.2 Hyaluronic Acid *in vitro* response

4.2.1 Metabolic activity of SVF

To assess the optimal hyaluronic acid concentration, MTT assay was performed. The MTT cytotoxicity assay was performed by incubating AD-MSC for SVF expansion for 72 hours with different concentrations (7, 15, and 25 % v/v of HyA in complete culture medium, DMEM with 10% FBS) of HyA1, HyA2, and HyA3. No significant differences between the concentrations for each hyaluronic acid were observed (Figure 15). No toxicity was observed at all according to figure below.

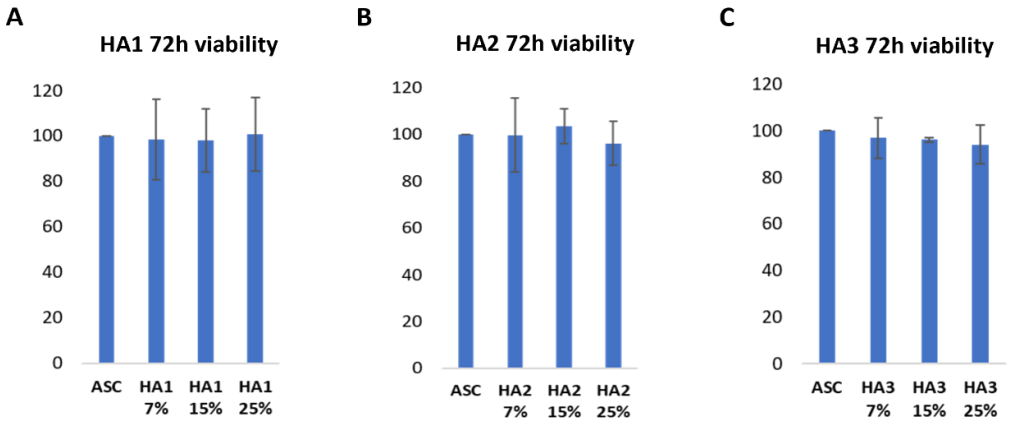

Figure 15. MMT cytotoxicity assay of AD-MSC for SVF expansion (passage 4th) tested with different concentrations: 0, 7, 15, 25% v/v of HyA in complete culture medium for 72 hours. There was no notable variance in cell viability when AD-MSCs were exposed to HyA1 (**A**), HyA2 (**B**) and HyA3 (**C**).

4.2.2 *In vitro* adipogenic stimulation

To investigate the possible role of hyaluronic acid (HyA) to inducing adipogenic stimulation, SVF expanded cells (passage 4^{th}) were cultured separately with 25% v/v hyaluronic acid (HyA1, HyA2, and or HyA3) in complete culture medium for 7, 14, 21, and 28 days when differentiated cells displayed cell rounding and lipid droplet formation. The lipid droplet absolute number and average area were quantified at each time point (7, 14, 21, and 28 days, as reported in Figure 16). From 14 days post-injection, all groups exhibited a significant increase in lipid droplet numbers compared to untreated cells with HyA (CTRL - 9.2 ± 5.7, CTRL + 74.7 ± 25, HyA1 31.3 ± 4, HyA2 108.5 ± 20.6, HyA3 86.7 ± 17.5; Figure 16A). The results confirmed HyA's adipogenic induction over time. Furthermore, the SVF expended cells exposed with HyA2 and HyA3 at 21 days showed a statistically significant increase in lipid droplet number compared to cells induced with adipogenic medium (CTRL + 57.7 ± 16.6, HyA2 216.8 ± 21.1, HyA3 289.3 ± 32.4; $p<0.0001$). The statistical difference was also maintained at 28 days for HyA3 cells compared to CNTR + (CTRL + 32.2 ± 5.7, HyA3 121.5 ± 16.8; $p=0.0015$). At 28 days, HyA3 exhibited a statistical increase in lipid droplet number compared to HyA1 (HyA3 121.53 ± 16.8, HyA1 57.53 ± 11.6; $p=0.0324$). SVF cells treated with each HyA showed a maximum peak of lipid droplet production at 21 days, followed by a subsequent decrease at the last time point (28 days, as depicted in Figure 16A).

The average area of the droplets decreased in all experimental groups from 7 to 21 days, followed by a substantially significant increase from 21 to 28 days (Figure 16B). At 21 and 28 days, all the SVF expended cells exposed with each HyA showed a statistical increase in the lipid droplet area ($p<0.0001$), except for HyA1 at 28 days. Furthermore, HyA3 induced higher lipid droplet areas than HyA2 at 28 days (HyA3 11.2 ± 0.9, HyA2 4.24 ± 0.4; $p<0.0001$).

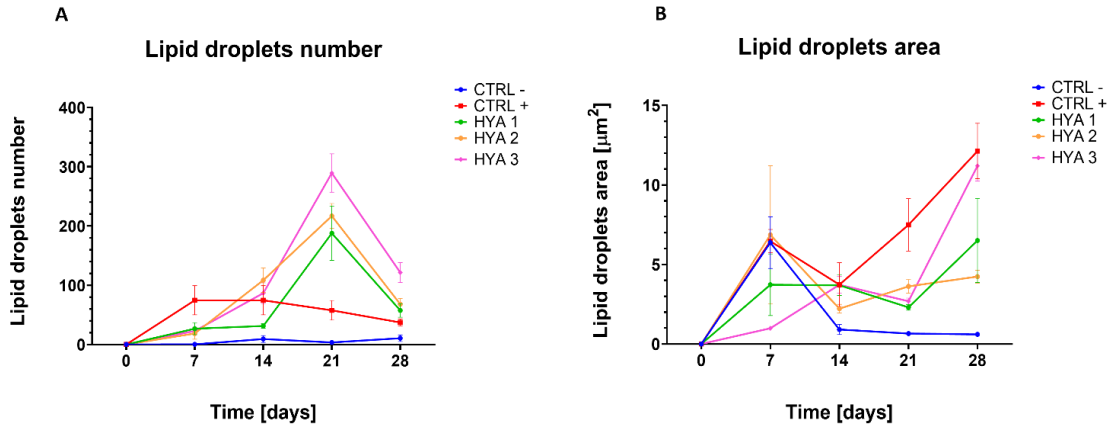

Figure 16. Lipid droplet numbers and area in SVF expanded cells (passage 4th) with HyA1, HyA2, and HyA3 for 7, 14, 21, 28 days. Control groups were treated with complete cultured medium (DMEM + 10% FBS) or with adipogenic induction medium (respectively CTRL – and CTRL +). (**A**) From 14 days, quantification of lipid droplets number showed a statistically significant increase of SVF expended cells exposed with HyA1, 2, 3 compared to CNTR -. At 21 days, HyA2 and HyA3 treated cells showed an increase of lipid drop numbers compared to CNTR + (****p<0.0001). At 28 days, HyA3 exhibited a statistical increment of lipid droplet numbers compared to CNTR + and HyA1. (**B**) Quantification of lipid droplet area showed a statistically significant increase in SVF expended cells exposed with HyA1, 2, 3 and compared to CNTR -. At 28 days SVF expended cells exposed with HyA3 had an increase in lipid droplet area compared with cells exposed to HyA2 (****p<0.0001). For each condition was analysed 5 random fields in 3 technical replicates. The data was analysed with Two-way ANOVA test. The values were represented as mean ± SEM.

4.3 *In vivo* regenerative potential of Hyaluronic Acids and Stromal Vascular Fraction

The capacity for adipose tissue neoformation following subcutaneous injection of SVF with HyA1, HyA2, and HyA3 was assessed to identify their regenerative potential. Balb/c nu/nu male mice received a right flank subcutaneous injection of micro-fragmented human adipose tissue mixed with HyA1, HyA2, or HyA3. The contralateral flank was injected with the correspondent HyA as a control. All animals were examined with magnetic resonance imaging (MRI) and histological analysis at 3, 7, 14, and 30 days post-injection were performed.

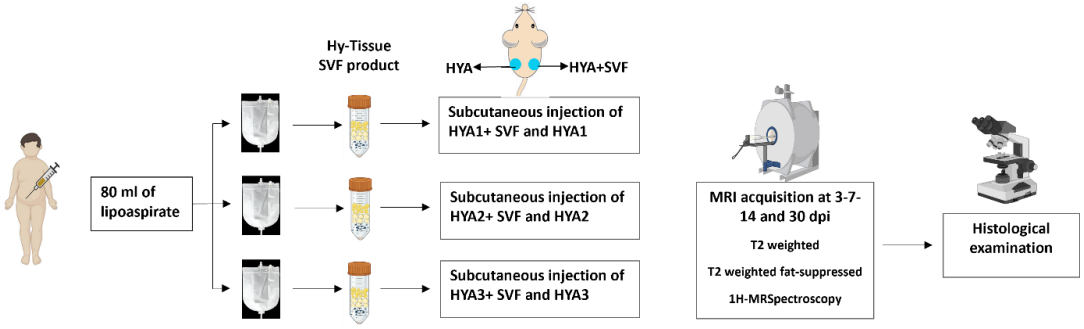

Figure 17. Experimental plan of regenerative potential.

4.3.1 *In vivo* adipose stimulation of SVF and HyMovis (HyA1)

The MRI T2-weighted (T2-w) analysis revealed that all the animals receiving the subcutaneous injection of SVF and HyA1 started a neoformation of adipose tissue 14 days post-injection (Figure 18A). This evidence was also confirmed by the MRI T2-w fat suppression, in which the possible newly formed adipose tissue signal was completely saturated (Figure 18B). Placing a voxel in the area of interest enabled localized Hydrogen-nuclear magnetic resonance (H-NMR) spectroscopy analysis, which revealed a complete correspondence between the spectrum of fat and the newly potential adipose tissue (Figure 18C).

Additionally, T2-w sequences revealed that HyA1 persisted in the subcutaneous tissue for 14 days after injection before undergoing complete reabsorption (Figure 18A).

The hematoxylin and eosin histological evaluation also confirmed MRI data. Tissues extracted from the SVF and HyA1 injected flank were characterized for the production of adipose tissue beneath the *erector pili* muscle (Figure 18E). Some small blood vessels were observed (Figure 18F). Tissue extracted from the contralateral side, treated only with HyA1, exhibited an unchanged subcutaneous morphology. (Figure 18D).

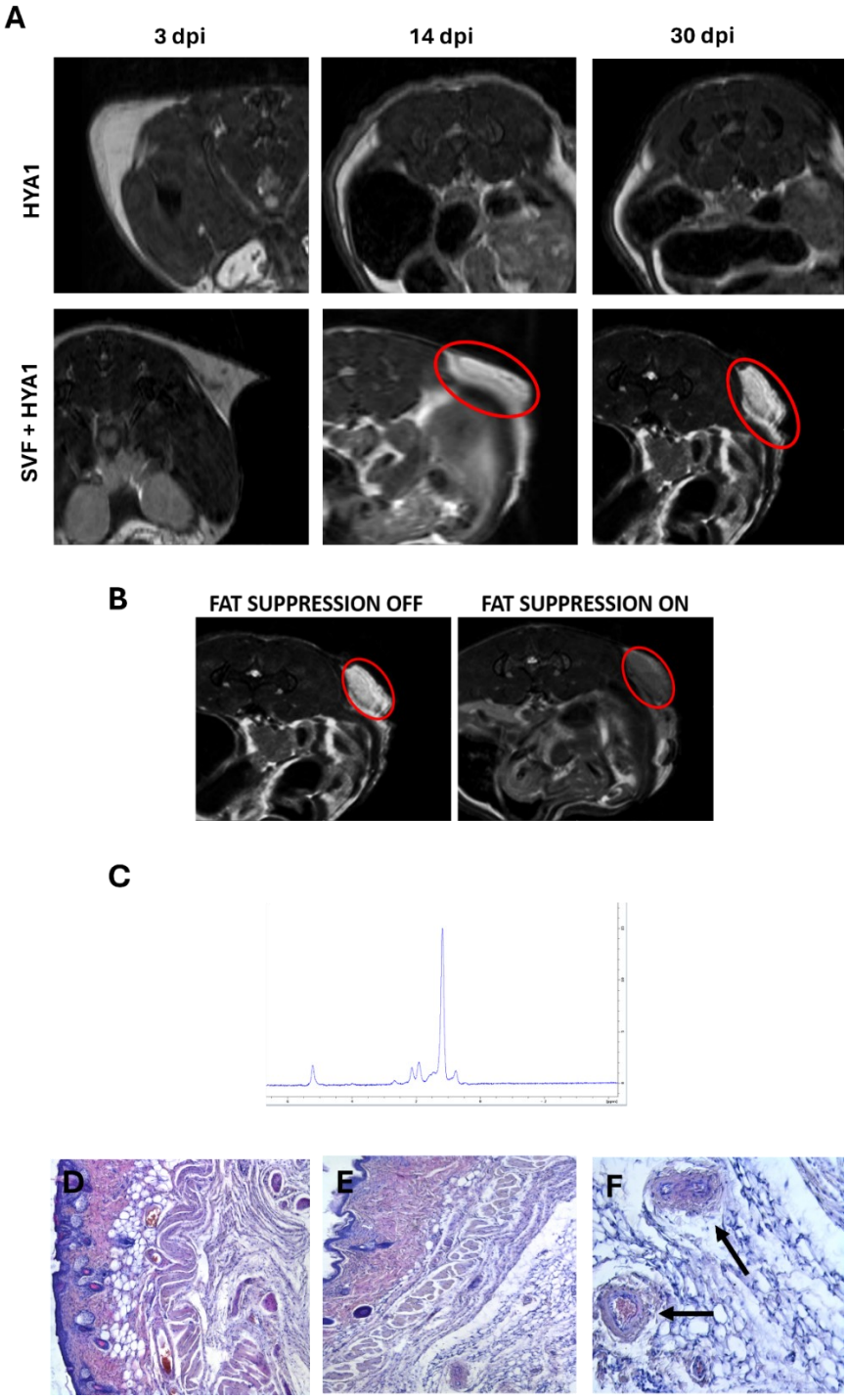

Figure 18. Adipose neoformation after subcutaneous injection of SVF and HyA1. (**A**) Axial MRI T2-w analysis showed the neoformation of adipose tissue after 14 days from the injection of SVF+HyA1, as highlighted by the red circle. The HyA1 was reabsorbed entirely after 14 days. (**B**) Axial MRI T2-w fat suppression images confirmed the formation of adipose tissue. (**C**) Fat spectrum from H-NMR spectroscopy analysis confirmed the formation of adipose tissue. (**D, E, F**) Representative light microscopy images of mice SVF

and HyA1 subcutaneous injected site stained with hematoxylin and eosin. (**D**) Mice after subcutaneous HyA1 injection showed normal tissue morphology after 14 days. (**E, F**) Mice injected with SVF+HyA1 showed the newly formed adipose tissue from 14 days, characterized by small blood vessels (indicated with black arrows).

4.3.2 *In vivo* adipose stimulation of SVF and HYAlubrix (HyA2)

The MRI T2-w analysis showed that SVF and HyA2 injected animals exhibited an adipogenic neoformation form 30 days post-injection (Figure 19A), while after 14 days post-injected, the HyA2 was completely reabsorbed from the contralateral control flank (data not shown). MRI T2-w fat suppression and localized H-NMR spectroscopy analysis confirmed these data (Figure 19B, C).

Also, these observations were corroborated by subsequent histological and ultrastructural analyses with scanning electron microscopy (SEM), illustrating the formation of newly developed adipose tissue interspersed with collagen matrix and micro-vessels in the underlying region of the *erector pili* muscle (Figure 19D, F-M). Newly adipose tissue was characterized by large diameters of adipocytes interposed by fibrotic and inflamed connective tissue, as shown by optical and ultrastructure analysis (Figure 19F-M).

Tissue injected with HyA2 alone showed an unaltered subcutaneous morphology (Figure 19D).

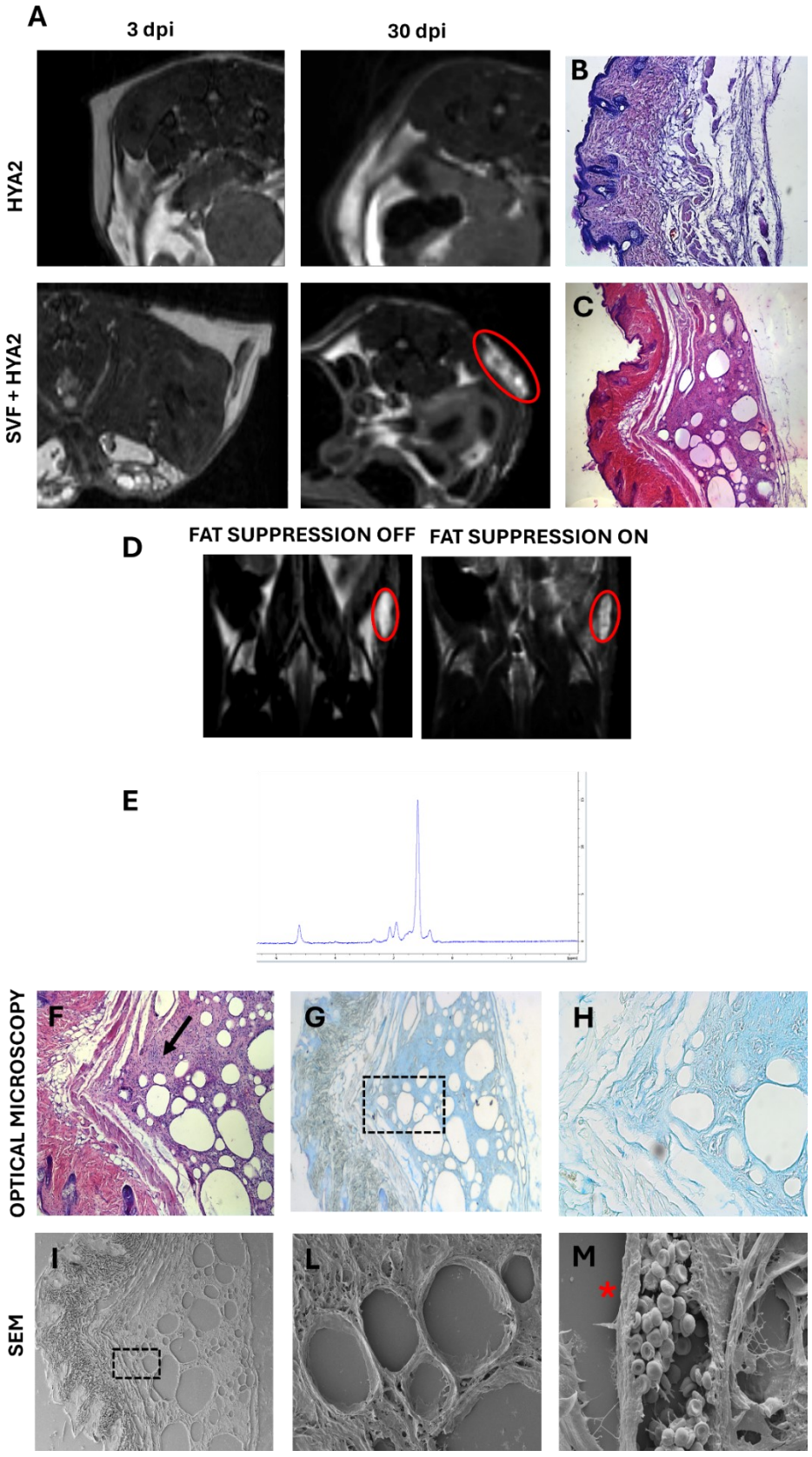
A
3 dpi
30 dpi
HYA2
SVF + HYA2
B
C
D
FAT SUPPRESSION OFF
FAT SUPPRESSION ON
E
OPTICAL MICROSCOPY
F
G
H
SEM
I
L
M

Figure 19. Adipose neoformation after subcutaneous injection of SVF and HyA2. (**A**) Axial MRI T2-w analysis showed the neoformation of adipose tissue after 30 days from the injection of SVF+HyA2, as highlighted by the red circle. (**B**) Representative picture of HyA2 subcutaneous injected site stained with hematoxylin and eosin showed no formation of adipose tissue at 30 dpi. (**C**) Representative picture of SVF and HyA2 subcutaneous injected site stained with hematoxylin and eosin showed the formation of adipose tissue form (30 days). (**D**) Coronal MRI T2-w fat suppression images confirmed the formation of adipose tissue. (**E**) Fat spectrum from H-NMR spectroscopy analysis confirmed the formation of adipose tissue. (**F**) Representative picture of SVF and HyA2 subcutaneous injected site stained with hematoxylin and eosin showed the formation of adipose tissue characterized by inflammatory and fibrotic extracellular matrix (ECM) surrounding (indicated with black arrow). (**G, H**) Alcian Blue staining confirmed the presence of fibrotic ECM that embedded the adipose tissue. (**I, L**) Scansion electron microscopy showed the large diameters of adipose tissue embedded in a fibrotic ECM. (**M**) SEM blood vessels image inside the fibrotic ECM (indicated with red asterisk).

4.3.3 *In vivo* adipose stimulation of SVF and Ial-System ACP (HyA3)

Concerning the third tested HyA, the best result was obtained after the subcutaneous injection of SVF with HyA3. The MRI T2-w analysis revealed that all the animals receiving treatment started a neoformation of adipose tissue 7 days post-injection (Figure 20), one or two time points before the other two scaffolds (HyA1 and HyA2). This evidence was also confirmed by MRI T2-w fat suppression and localized H-NMR spectroscopy analysis. The MRI analyses also showed that HyA3 was reabsorbed 7 days after the subcutaneous injection.

The subsequent histological analysis confirmed the *in vivo* MRI results (Figure 20B-G). In the tissue extracted from the SVF and HyA3 injected flank, the newly formed adipose tissue was characterized by a well-established structure with adipocytes organized in lobules separated by well-defined collagen septa (Figure 20C, D, F, G). Microvessels were present internally to facilitate the supply of essential nutrients.

Tissue injected with HyA3 displayed an unaltered morphology (Figure 20B, E).

Taking together the in vivo results from the subcutaneous injection of SVF with HyA1, HyA2, and HyA3, the best result was obtained after the injection of SVF with HyA3, showed a neoformation of adipose tissue from 7 days.

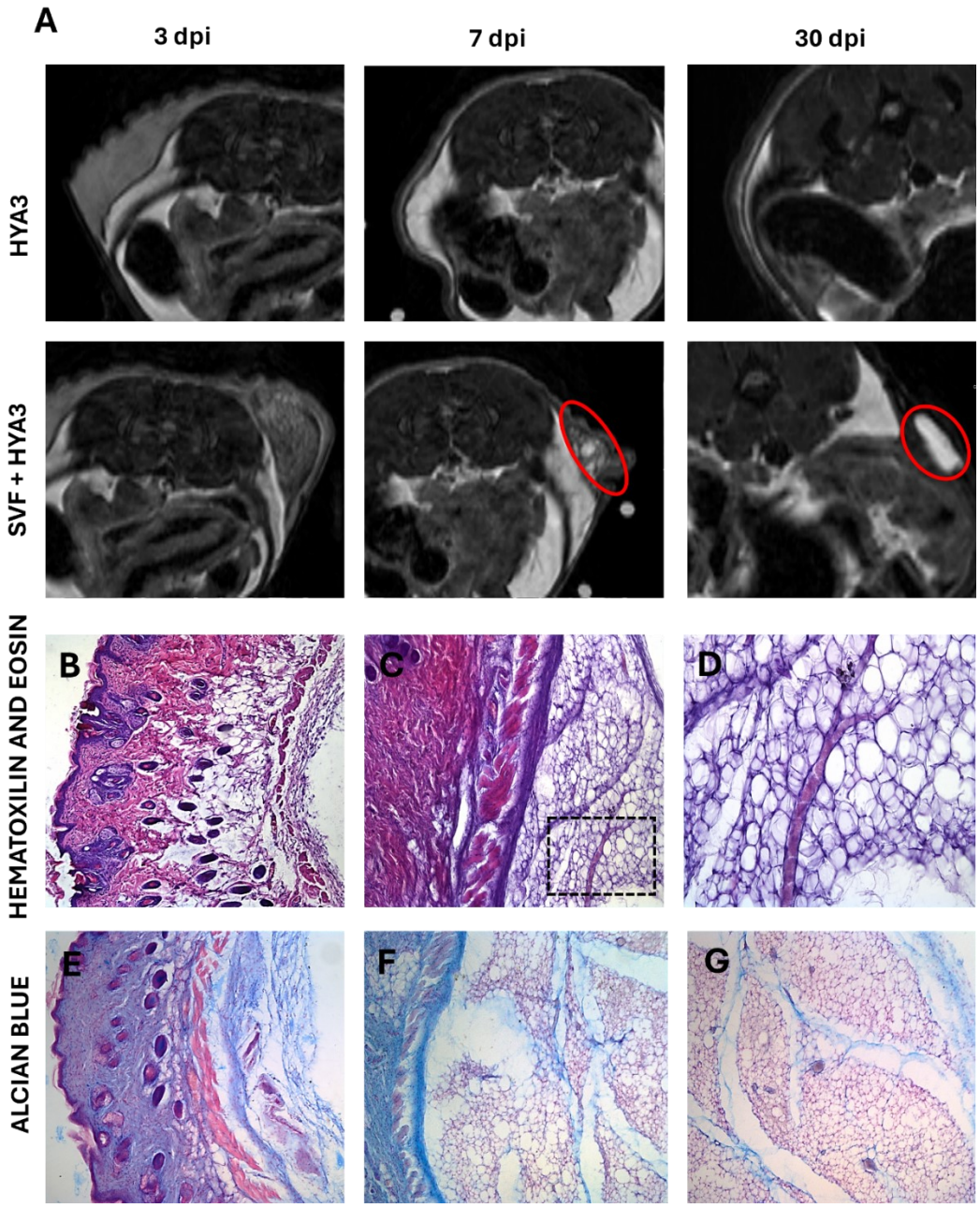

Figure 20. Adipose neoformation after subcutaneous injection of SVF and HyA3. (**A**) Axial MRI T2-w analysis showed the neoformation of adipose tissue after 7 days from the injection of SVF+HyA3, as highlighted by the red circle. The HyA3 was reabsorbed entirely after 7 days. (**B, C, D**) Representative light microscopy images stained with

hematoxylin and eosin. (B) Representative picture of HyA3 subcutaneous injected site showed no formation of adipose tissue at 7 days. (C, D) Representative picture of SVF+HyA3 showed formation of adipose tissue embedded in collagen saepta from 7 days. (**E, F, G**) Representative histological pictures stained with alcian blue and fast red (alcian blue). (E) Representative picture of HyA3 subcutaneous injected site showed no formation of adipose tissue at 7 days. (F, G) Representative picture of SVF+HyA3 showed formation of adipose tissue from 7 days.

4.3.4 Immunofluorescence analysis

To determine the origin of the newly formed tissue, the explanted tissues were examined using a human leukocyte antigen HLA antibody (HLA). This aimed to ascertain whether it resulted from the differentiation of MSCs within the SVF (human origin) or from paracrine stimulation of the SVF mixed with scaffolds (mouse origin).

Positivity was observed 14 days post-injection in animals receiving SVF mixed with HyA3 (Figure 21C), but at 30 days post-injection, HLA positive signal was absent in all animals (Figure 21F, I).

No positive signal was observed in animals injected with SVF with HyA1 or HyA2 after 14 and 30 days post-injection (Figure 21A, B, D-H).

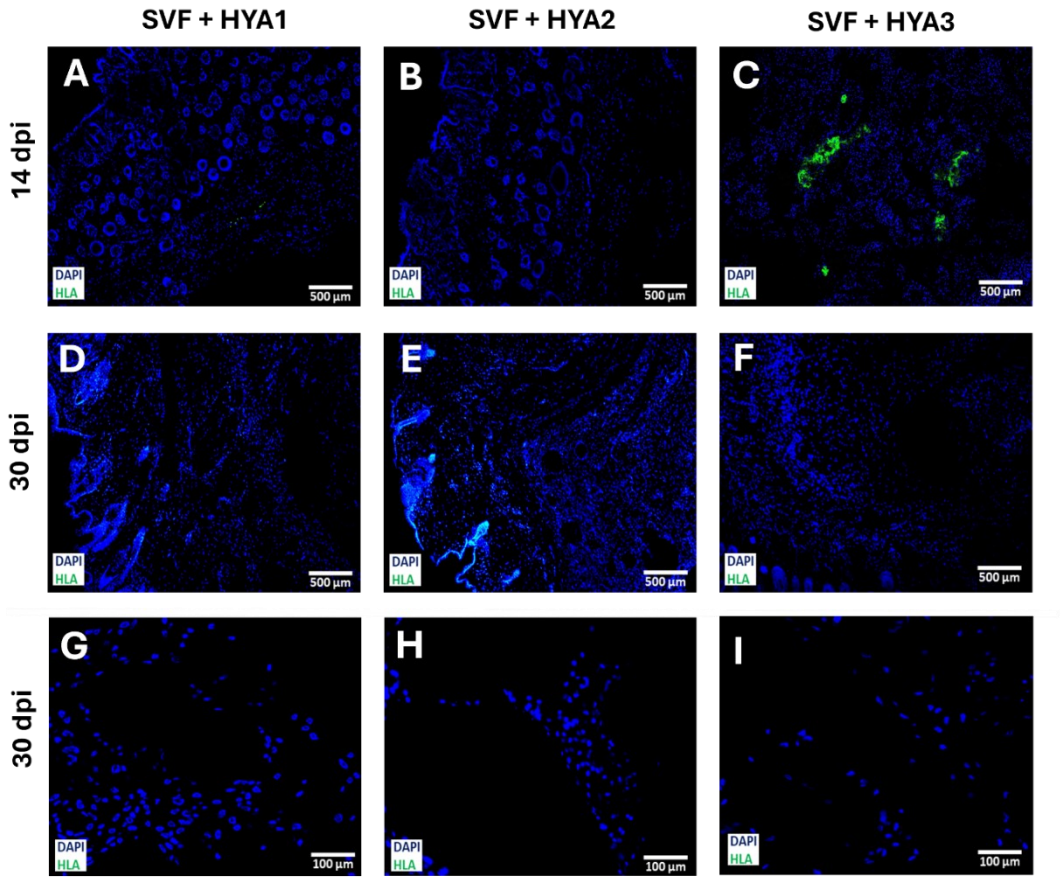

Figure 21. HLA immunofluorescent staining in the subcutaneously injected side receiving SVF+HyA1, SVF+HyA2, and SVF+HyA3 at 14 and 30 days post-injection. The HLA was stained with FITC fluorophore, and nuclei were stained in blue with dapi. (**A, D, G**) Animals treated with SVF+HyA1 showed negative HLA signals at 14 and 30 days. (**B, E, H**) Animals treated with SVF+HyA2 showed negative HLA signals at 14 and 30 days. (**C, F, I**) Animals treated with SVF+HyA3 showed positive HLA signals at 14, and negative signals at 30 days. 10x and 20x objective magnification, scale bar 500 µm and 100 µm.

4.4 Metabolic activity, DNA content, and migration evaluation of Stomal Vascular Fraction and Hyaluronic Acid 3

4.4.1 Cellular metabolic activity and DNA quantification

To assess biocompatibility, the capacity of HyA3 to support cellular viability and sustain growth in culture was investigated. Biochemical assays evaluated the cellular metabolic activity and DNA content in expanded SVF cells with half HyA3

and half complete culture medium. The results were compared with cells untreated with HyA3, but with only the complete culture medium.

HyA3 with SVF expanded cells induced a statistically significant increase in metabolic activity compared to the control cells (Figure 22A) at all time points (3 days HyA3 289.8 ± 22.2% vs medium 100% ± 5.4, 7 days HyA3 485.3 ± 17.8% vs medium 186.6 ± 3.5%, and 14 days HyA3 388.4 ± 33.9% vs medium 217 ± 21.3%, $p < 0.001$). Furthermore, no significant difference was observed in DNA content expression between the two experimental groups during the testing time (Figure 22B). These results confirm the biocompatibility of the HyA3 product.

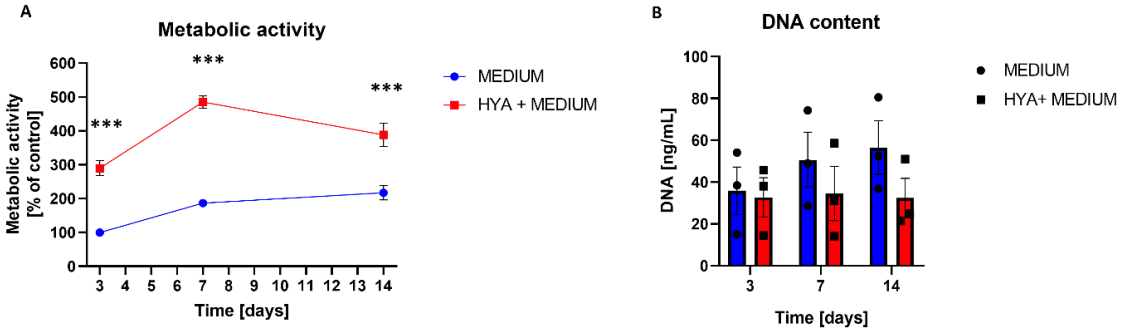

Figure 22. Metabolic activity and DNA content of SVF expanded cells at 3, 7, 14 days. (**A**) Metabolic activity of cells treated with HyA3 (HYA + MEDIUM) compared with untreated cells (MEDIUM). The treated condition showed a statistical increment of metabolic activity compared to control at each timepoint (***$p<0.001$). (**B**) No significant differences in DNA contact between the groups were found. In metabolic activity assay, for each condition was analysed 9 technical replicates at 3 days, 6 technical replicates at 7 days, and 3 technical replicates at 14 days. In the DNA content assay for each condition was analysed, 3 technical replicates at all time points. The data was analysed with Two-way ANOVA test. The values were represented as mean ± SEM.

4.4.2 Scratch test

The migration capacity of the SVF expanded cells (passage 4^{th}) cultured with half HyA3 and half complete medium was evaluated with a scratch assay (Figure 23A, B). The results were compared with the same cells cultured with complete culture medium as a control. Gap distance was measured at 0, 1, 2, 4, 8, 24, and 36 hours

post scratch. A reduction in gap distance was observed for both groups over time from 8 hours (HyA3 8h 77.8 ± 3.3% vs HyA3 24h 22.7 ± 8.4%, $p<0.0001$; medium 8h 86.7 ± 6.5% vs medium 24h 42.9 ± 12.1%, $p=0.0013$). At 24 and 36 hours, the mixture of HyA3 with complete medium induced a significant reduction in the scranched areas compared to the complete medium (HyA3 24h 22.7 ± 8.4%, medium 24h 42.9 ± 12.1%; HyA3 36h 12 ± 6.6%, medium 36h 24.8 ± 10.6%; $p<0.0001$, Figure 23B).

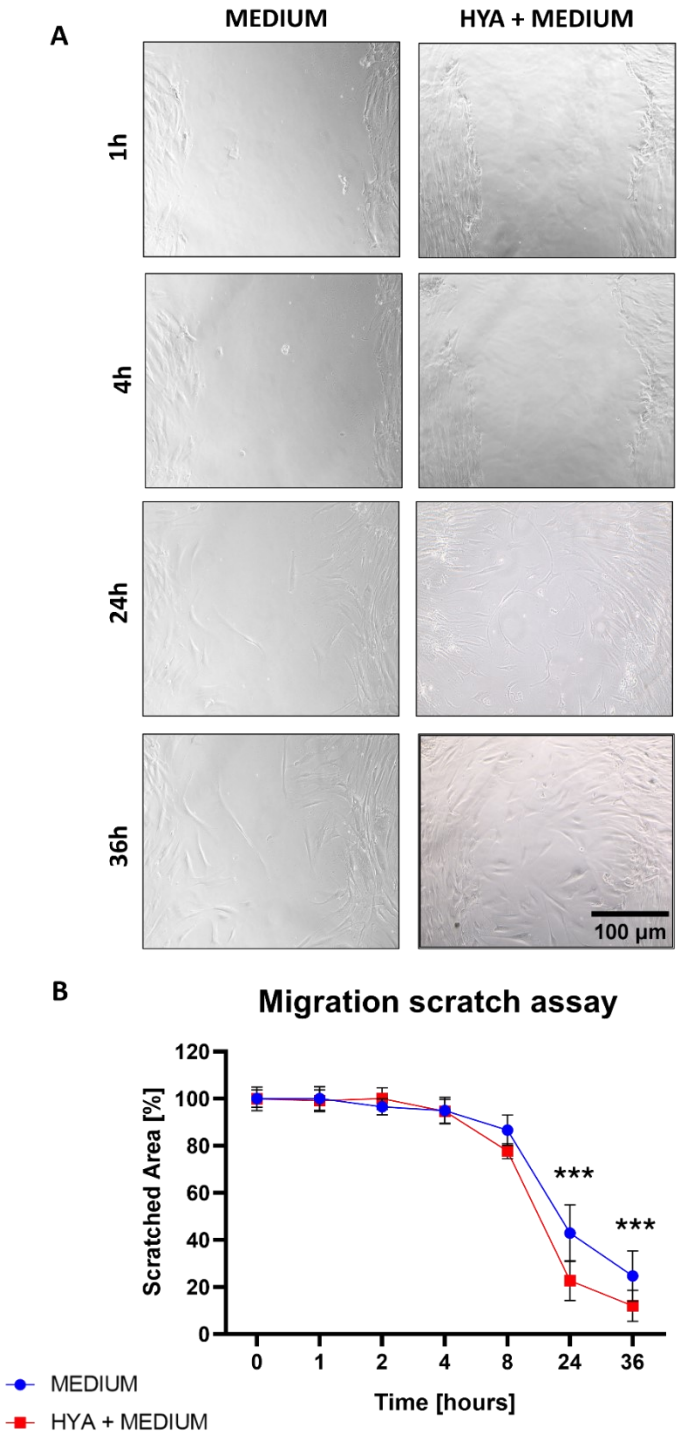

Figure 23. SVF expanded cells scratch test for cell migration assay. (**A**) Representative images of migration assay at 1, 4, 24, and 36 hours after scratch, comparing the two experimental conditions (control and cell treated with HyA3). 10x magnification, scale bar 100 µm. (**B**)At 24 and 36 hours, stanched areas of SVF-expended cells treated with HyA3 showed a significant reduction compared to cells with complete medium. (***p<0.001).

For each condition was analysed 4 conservative fields in 3 technical replicates. The data was analysed with Two-way ANOVA test. The values were represented as mean ± SEM.

4.5 *In vivo* pathological regenerative potential in a muscle ischemic reperfusion model

After the *in vivo* evaluation of the regenerative potential of the SVF with HyA, the product composition with a better outcome was tested in a muscle ischemic reperfusion mouse model. The combination of the SVF and Ial-System ACP (HyA3), through MRI and histological analysis, exhibited an early and superior capacity to stimulate adipose tissue neoformation compared to SVF with the other two hyaluronic acids (HyA1 and HyA2). The muscle ischemic reperfusion (I/R) injury was induced with a tourniquet model. Twenty-four hours post-I/R injury, mice received intramuscular treatment injection in the quadriceps. The animals were monitored for 18 days with MRI protocol acquisitions and motor behavioral experiments. Post-mortem histological and immunohistochemistry evaluations were performed.

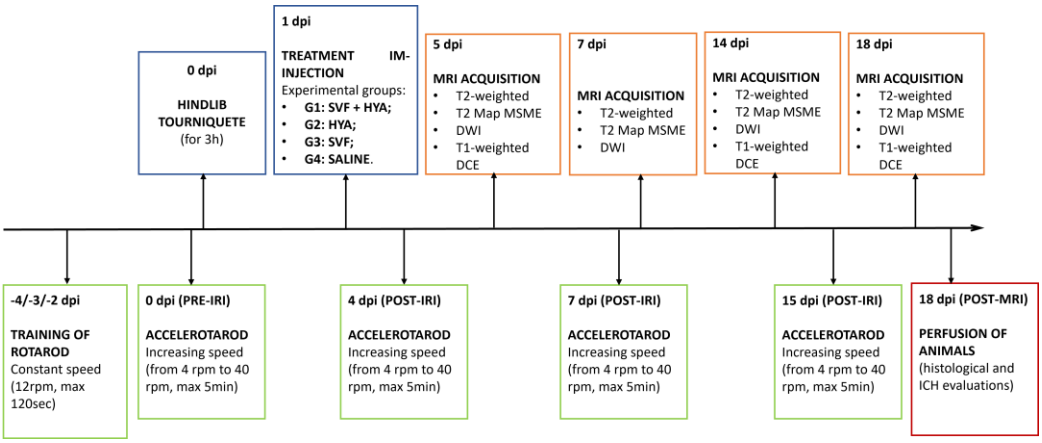

Figure 24. Experimental plan of muscle I/R injury.

4.5.1 Motor Behavioral Experiment

After three consecutive training days, an accelerod test was conducted to evaluate motor coordination. Accelerod test was performed at different time points: 4, 7, and 15 dpi (Figure 25). Latency and rotation speed were recorded, indicating the time taken for animals to fall off the rod. A progressive improvement in motor

performance was observed over time in the SVF and SVF+HyA groups (SVF 7 dpi 13.8 ± 0.5, SVF 15 dpi 15.5 ± 0.5; SVF+HyA 7 dpi 15.6 ± 3.4, SVF+HyA 15 dpi 18.7 ± 3.7). By 7 dpi, motor performance was comparable to baseline. Conversely, the group receiving HyA injection showed a linear performance trend between 4 and 7 days post-I/R injury and a slight decrease from 7 to 15 days (HyA 7 dpi 14.6 ± 3.9, HyA 15 dpi 13 ± 1.5). No alterations in motor performance were observed in saline-injected animals (saline 0 dpi 11.7 ± 3, saline 4 dpi 12.3 ± 1.7, saline 7 dpi 12 ± 1.8, saline 15 dpi 11.7 ± 2.1).

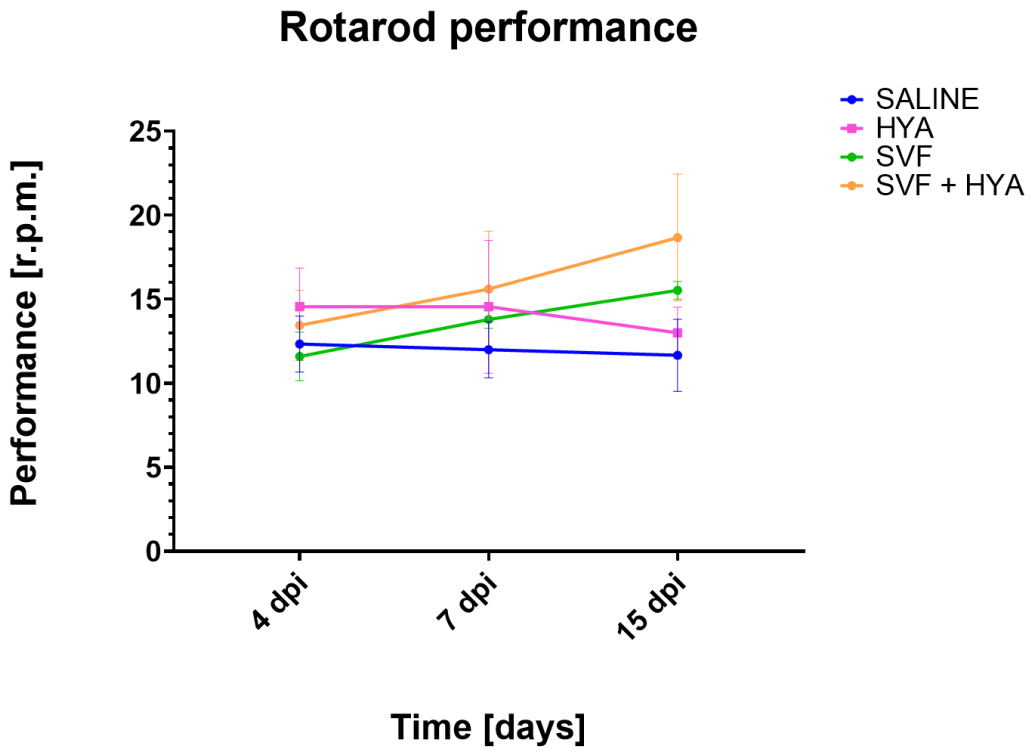

Figure 25. Rotarod test performed 4 dpi, 7dpi, and 15 dpi to saline, HyA, SVF, and SVF+HyA treated animals. The performance was expressed in rpm. No significant differences were observed, but a progressive improvement in motor performance was observed from 4 to 15 dpi in the SVF and SVF+HyA groups. The data was analysed with Two-way ANOVA test. The values were represented as mean ± SEM, n=25.

4.5.2 MRI

Structural and functional changes after intramuscular injection of saline, HyA, SVF, and SVF+HyA were investigated with multi-parametric MRI analysis. T2-weighted (T2-w), T2-mapping, and DWI acquisitions were performed at 4, 7, 14, and 18 days post-I/R injury. The ischemic reperfusion-treated limb of each animal was compared with the contralateral control limb (CTRL).

4.5.2.1 T2-weighted

T2-w MRI acquisitions at 4 dpi revealed hyperintense contrast in all injured right hindlimbs, associable with increased tissue water content resulting from edematous and inflammatory responses following I/R injury (Figure 26). Starting from 7 dpi, SVF+HyA-treated animals exhibited a T2-weighted contrast similar to CTRL over time. Differently, at 7 and 14 dpi, animals treated with saline and SVF maintained a marked hyperintense contrast compared to CTRL hindlimbs, while those treated with HyA showed slight improvement. At 18 dpi only the animals treated with saline retained the hyperintense contrast.

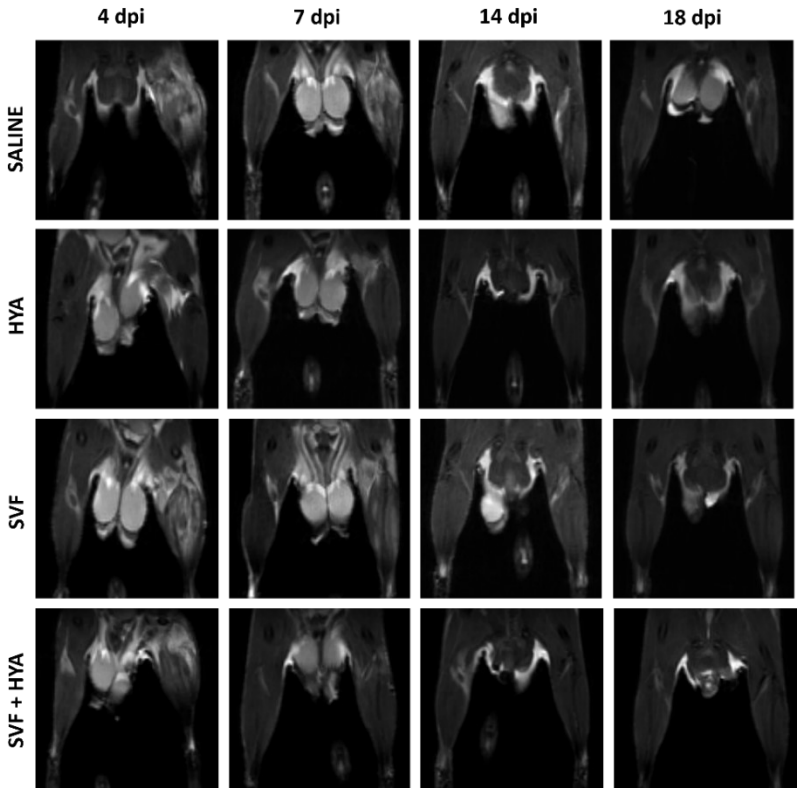

Figure 26. Representative images of T2-weighted MRI acquisitions at 4, 7, 14, and 18 dpi for saline, HyA, SVF, and SVF+HyA-treated animals. As CTRL was used the contralateral hindlimbs. N=25.

4.5.2.2 T2-mapping

The results from T2-mapping acquisitions confirmed T2-w imaging. T2-multi-sclice multi echoes (MSME) analysis revealed that the muscle relaxation time (T2-rt) of the CTRL was approximately 30 ms (Figure 27).

At 4 dpi, all treated hindlimbs exhibited a significant increment of the T2-rt compared to CTRL (CNTR 32.5 ± 0.5 ms, saline 63.8 ± 6.4 ms, HyA 132.4 ± 11.8 ms, SVF 50 ± 3.1 ms, SVF+HyA 87.1 ± 6.4 ms; CTRL vs saline p=0.0364, CTRL vs HyA p=0.005, CTRL vs SVF p=0.0075, CTRL vs SVF+HyA p=0.0004). From 7 dpi, the SVF+HyA treaded limbs showed a reduction of T2-rt value (close to 35 ± 1.3 ms) without significant difference compared to the CTRL T2-rt value. I/R injured animals treated with saline, HyA, and SVF maintained a significant increment of T2-rt at 7 and 14 dpi compared to CTRL and SVF+HyA treatment (saline 7 dpi 47.2 ± 2 ms, saline 14 dpi 41.7 ± 1.1 ms, HyA 7 dpi 68.5 ± 8.2 ms,

HyA 14 dpi 39.1 ± 0.9, SVF 7 dpi 44 ± 1.3 ms, SVF 14 dpi 37 ± 0.3; CTRL vs saline 7 dpi p=0.0068, CTRL vs HyA 7 dpi p=0.01, CTRL vs SVF 7 dpi p=0.0002, CTRL vs saline 14 dpi p=0.0022, CTRL vs HyA 14 dpi p=0.0044, CTRL vs SVF 14 dpi p<0.0001). The T2-rt values of HyA and SVF-treated animals decreased at 18 days post-I/R injury, without significant difference compared with CTRL and SVF+HyA injected hindlimb.

Only the saline-received animals maintained a significant increase in T2-rt values compared to the other groups (38.04 ± 0.8 ms; saline vs CTRL p=0.0039, saline vs SVF p=0.0428, saline vs SVF+HyA p=0.0015).

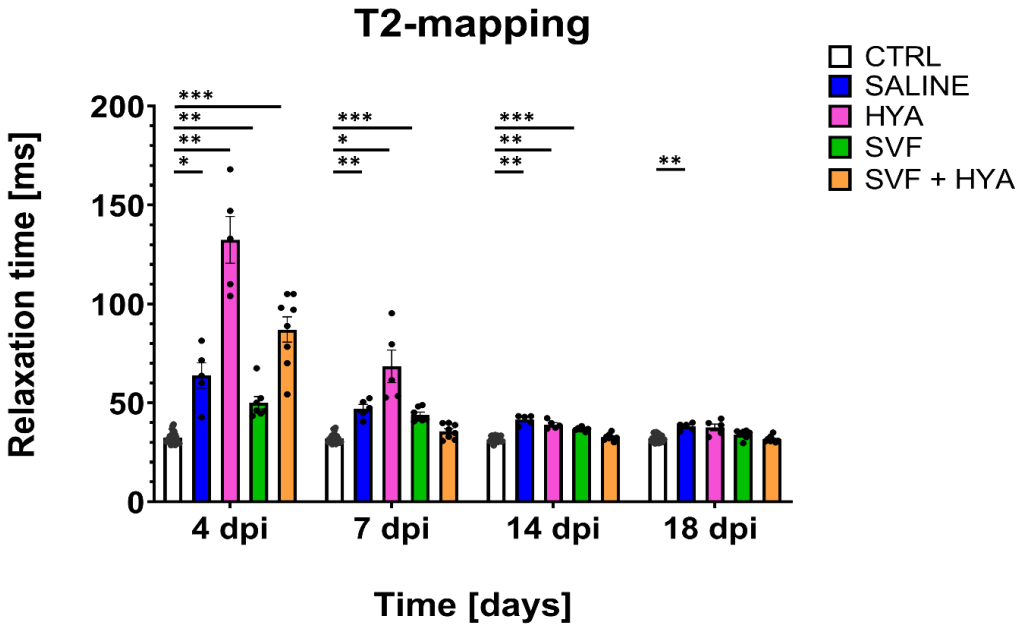

Figure 27. Muscle relaxation time was evaluated at 4, 7, 14, and 18 dpi for CNTR, saline, HyA, SVF, and SVF+HyA-treated animals. At 4 dpi all I/R injured groups showed a significant increase in T2-rt compared to CTRL (* CTRL vs saline p=0.0364, ** CTRL vs HyA p=0.005, ** CTRL vs SVF p=0.0075, *** CTRL vs SVF+HyA p=0.0004). At 7 dpi saline, HyA, and SVF maintained a significant increase in T2-rt compared to CNTR (** CTRL vs saline p=0.0068, * CTRL vs HyA p=0.05, *** CTRL vs SVF p=0.0002). No significant difference was observed between CTRL and SVF+HyA-treated animals. At 14 dpi saline, HyA, and SVF showed significantly increased in T2-rt compared to CNTR (** CTRL vs saline p=0.0022, ** CTRL vs HyA p=0.0044, *** CTRL vs SVF p<0.0001). At 18 dpi, only the saline-treated animals maintained a significant increase of T2-rt compared

to CTRL (** p=0.0039). The data was analysed with Two-way ANOVA test. The values were represented as mean ± SEM, n=25.

4.5.2.3 Diffusion-weighted imaging

The analysis of the DWI acquisition revealed no significant differences in the apparent diffusion coefficient (ADC) among all treatment groups at each time point.

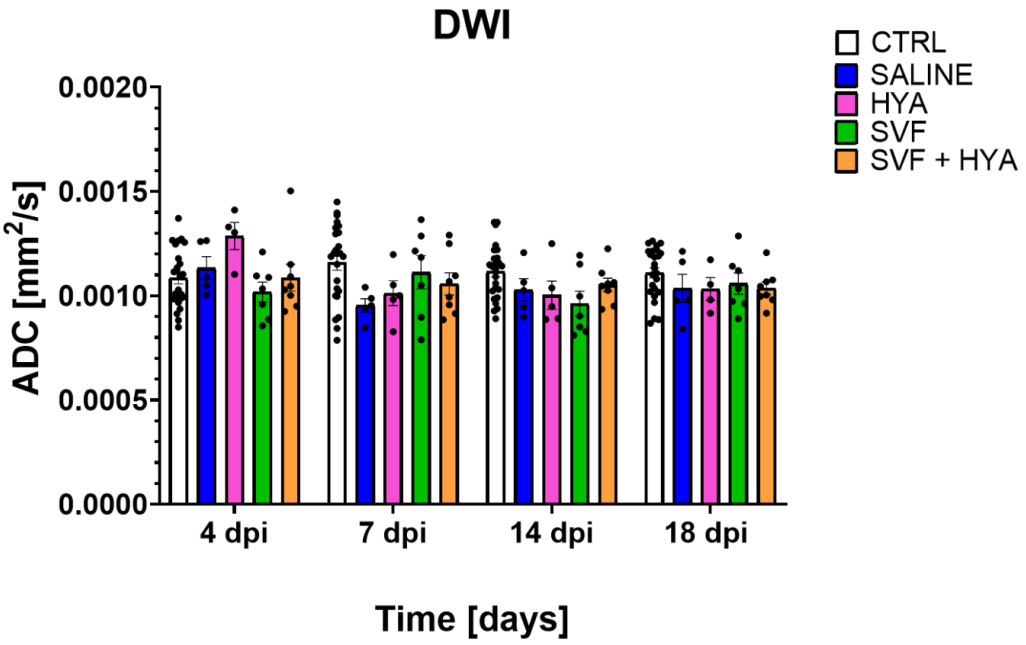

Figure 28. Diffusion-weighted imaging was performed at 4, 7, 14, and 18 dpi. The ADC was calculated for each time point in the saline, HyA, SVF, and SVF+HyA-treated groups and compared with the contralateral hindlimbs as a CTRL. No significant differences were observed. The data was analysed with Two-way ANOVA test. The values were represented as mean ± SEM, n=25.

4.5.2.4 Dynamic contrast-enhanced MRI

The vessel perfusion was assessed with a dynamic contrast-enhanced MRI (DCE-MRI) using a gadolinium-based contrast agent (Gd, Figure 29). All the gadolinium-diethylenetriamine pentaacetic acid (Gd-DTPA) signal intensity points (143 points in total) over time were normalized to the average baseline values. Subsequently, the area under the curve (AUC) was calculated. The AUC of each treatment was subtracted from the CTRL AUC.

At 4 dpi all I/R injured treated hindlimbs exhibited a nearly twofold higher contrast agent signal over time than CTRL (saline 272.1 ± 106, HyA 222.7 ± 162, SVF 141.8 ± 39, SVF+HyA 166.9 ± 80.7). At 18 dpi, salina, SVF, and SVF+HyA showed a similar Gd-DTPA intensity to the CTRL, while HyA-treated hindlimbs maintained a slight increase in Gd-DTA intensity.

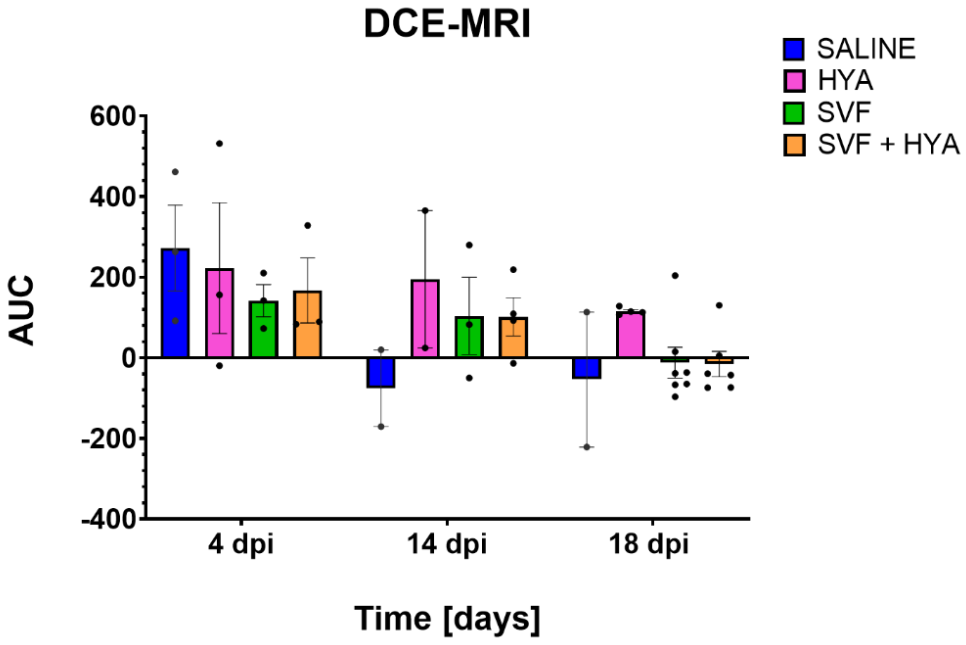

Figure 29. Dynamic contrast-enhanced MRI with the injection of Gd-DPTA contrast agent. The AUC for salina, HyA, SVF, and SVF+HyA was normalized to the average of the baseline values and then subtracted from the CTRL AUC at 4, 14, and 18 dpi. At 4 dpi all the I/R injured hindlimbs showed a higher Gd-DPTA than CTRL. At 18 dpi saline, SVF, and SVF+HyA groups showed a similar Gd-DTPA intensity to the CTRL, while HyA-treated hindlimbs maintained a slight increase in Gd-DTA intensity. The data was analysed with Two-way ANOVA test. The values were represented as mean ± SEM, n=25.

4.5.3 Histological and morphological evaluation

As described in the introduction, the gastrocnemius can be divided into two parts: medial (MG), adjacent to the plantar muscle, and lateral (LG) part, adjacent to the soleus. Since previous studies report differential impact on gastrocnemius fibers following I/R injury, the muscle has been subdivided into four principal areas, delineating regions where qualitative and quantitative assessments of histological and immunohistochemistry (IHC) parameters were conducted: superior MG, inferior MG, superior LG, and inferior LG (Figure 30).

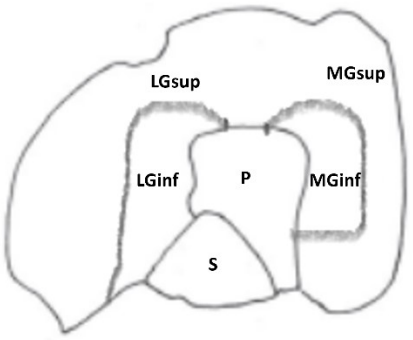

Figure 30. Graphical representation of posterior muscle division, formed by superior lateral gastrocnemius (LGsup), inferior lateral gastrocnemius (LGinf), superior medial gastrocnemius (MGsup), inferior medial gastrocnemius (MGinf), plantar (P), and soleus (S).

Hematoxylin and eosin staining were used for the histological evaluation of the cross-sectioned gastrocnemius muscle (Figure 31, 32). In sections from the CTRL group, standard histological staining with hematoxylin and eosin revealed myofibers of polygonal shape, uniform size, and laterally positioned nuclei both in LG (Figure 31A) and in MG (Figure 31B). No inflammatory infiltration was observed.

In sections from the saline-treated animal group, round-shaped fibers with size variability and centrally located nuclei indicative of muscle regeneration were mainly present in the superior and inferior regions of the LG (Figure 31C) and MG (Figure 31D-F). In addition, numerous necrotic fibers were visible in the superior

region of the MG, identified by pale eosin cytoplasmic staining (Figure 31D, G). A large infiltrate of immune cells surrounded them. Clear spaces surrounded by cells were evident in this area, most likely resulting from phagocytosis of necrotic fibers (Figure 31D, G, H). Numerous blood vessels were observed in the areas adjacent to the necrotic fibers, suggesting possible vascular compensation for muscle loss. The sections also revealed the presence of increased collagen deposition and inflammatory cell infiltrates, particularly evident in the regenerative areas.

Sections from animals treated with SVF or HyA displayed fibers in the superior LG and MG regions similar to those observed in uninjured control tissue (Figure 32I, O). However, in the inferior region of the muscle, some fibers with heterogeneous size and shape and a central nucleus surrounded by inflammatory infiltration were still detectable (Figure 32L, P). Increased collagen deposition was obvious between the altered myofibers. In the section from animals that received SVF treatment, large areas of the MG were composed of clear, rounded spaces surrounded by massive cellular infiltration (Figure 32M, N).

Sections from SVF+HyA-treated animals showed morphologically normal myofibers with the characteristic polygonal shape and a laterally positioned nucleus (Figure 32Q, R). No inflammatory infiltration between the individual muscle fibers was observed.

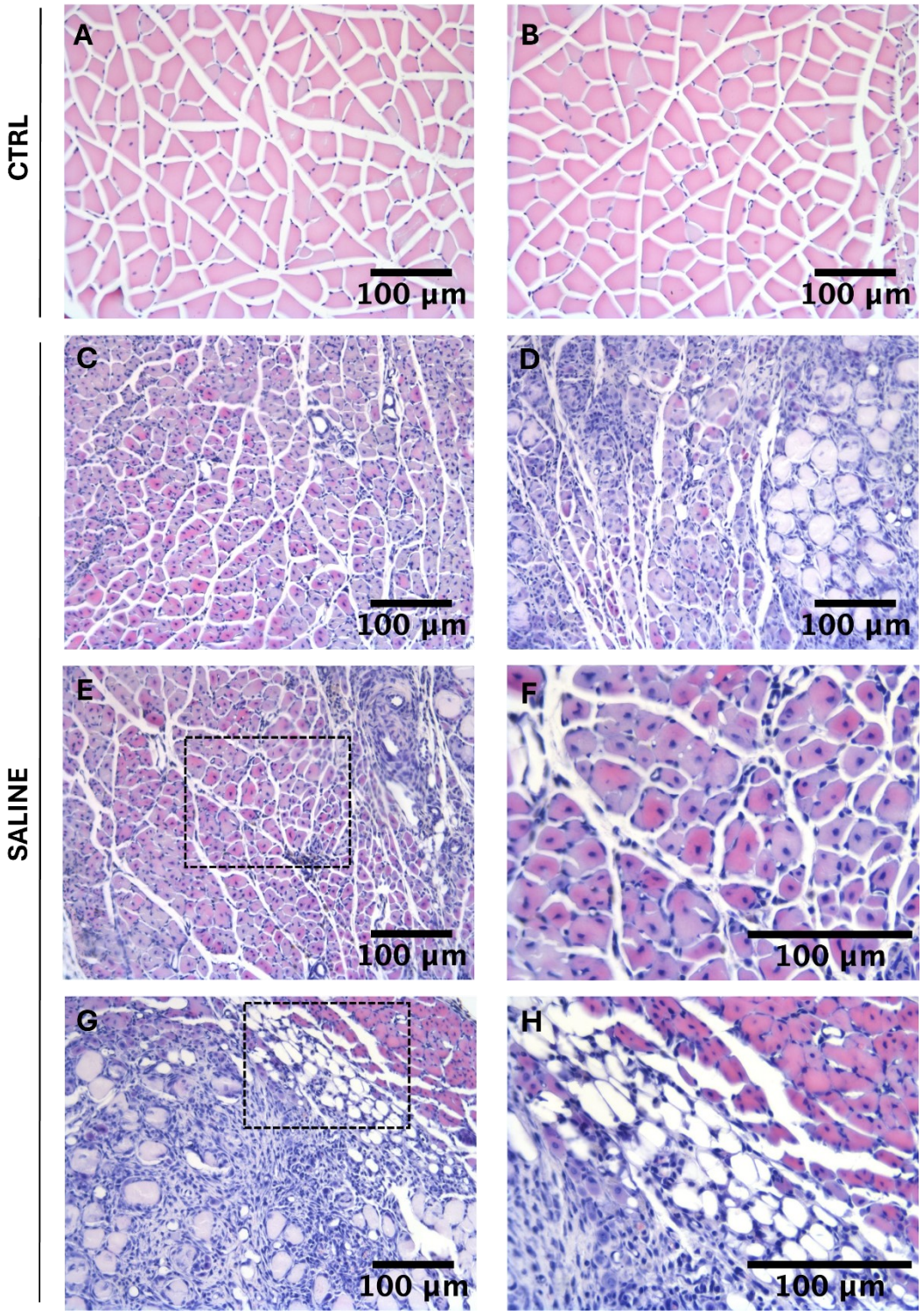

Figure 31. Histological evaluations of the gastrocnemius muscle 18 dpi of CNTR and saline groups. The muscle cross-sections were stained with hematoxylin and eosin. (**A, B, C, D, E, G**) 10x magnification, scale bar 100 µm. (**F, H**) 20x magnification, scale bar 100 µm.

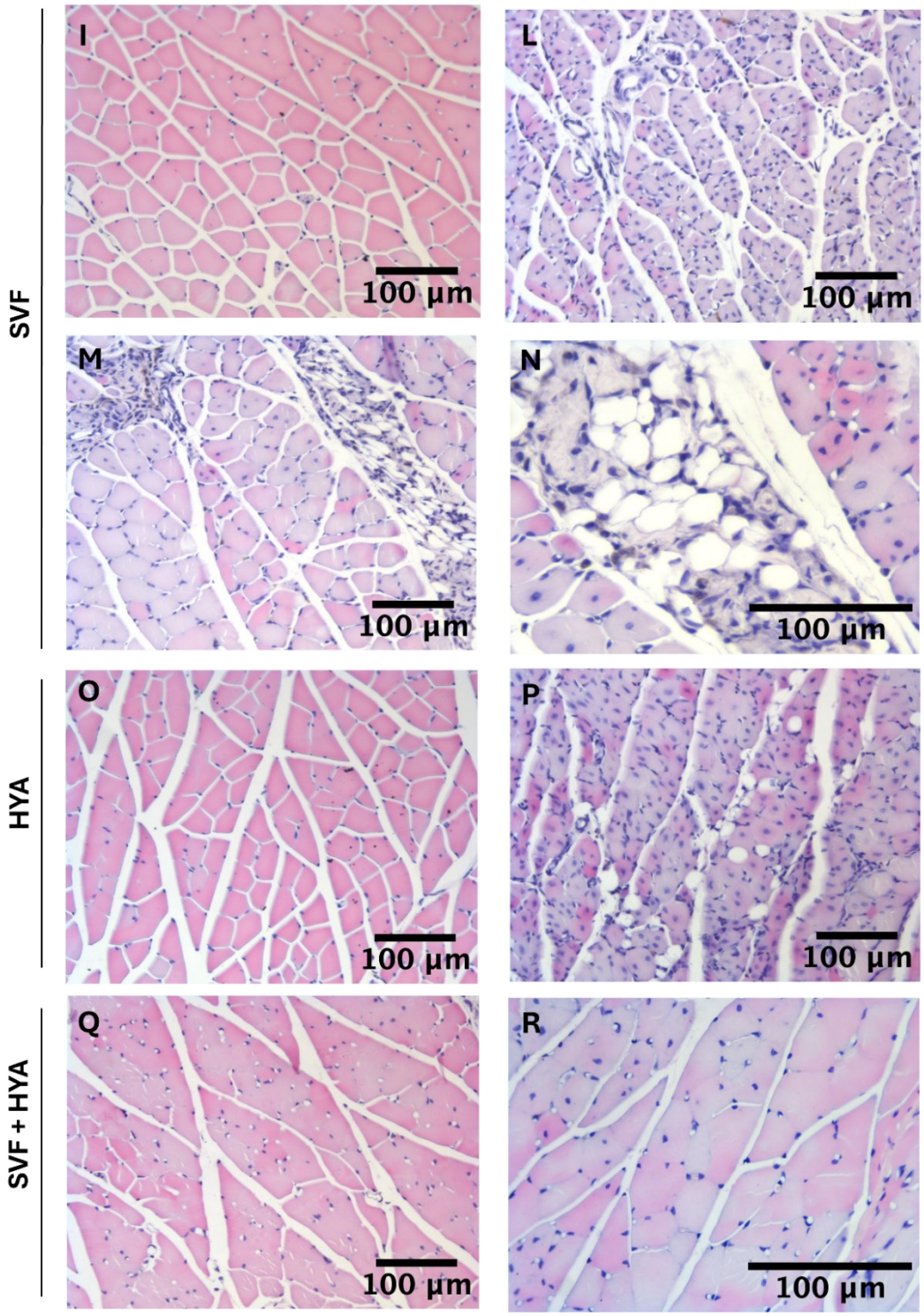

Figure 32. Histological evaluations of the gastrocnemius muscle 18 dpi of SVF, HyA, and SVF+HyA. The muscle cross-sections were stained with hematoxylin and eosin. (**I, L, M, O, P, Q, R**) 10x magnification, scale bar 100 µm. (**N**) 20x magnification, scale bar 100 µm.

4.5.4 Morphometric analysis

Hematoxylin and eosin staining performed on gastrocnemius muscle revealed the presence of fiber size variability in the inferior area of MG and LG regions. For this reason, the quantitative analysis of the average area of muscle fibers was calculated within the different groups separately in the inferior and superior of both MG and LG regions of the gastrocnemius muscle. When considering the quantitative analysis in superior MG or LG regions, the average fiber areas of CTRL were similar to that observed in SVF+HyA, while a clear decrease in average fiber area was present in saline, HyA, and SVF-treated animals compared to CTRL and/or SVF+HyA groups. The fiber area of the superior LG region in HyA and SVF groups was high compared to the corresponding group of the superior MG region, while the average fiber area of the saline group was similar both in superior MG and in LG (Figure 33A, B). When considering the quantitative analysis in inferior MG or LG regions, the average fiber areas of CTRL were similar to that observed in SVF+HyA, while a clear decrease in average fiber area was present in saline, HyA, and SVF-treated animals compared to CTRL and/or SVF+HyA groups (Figure 33C, D).

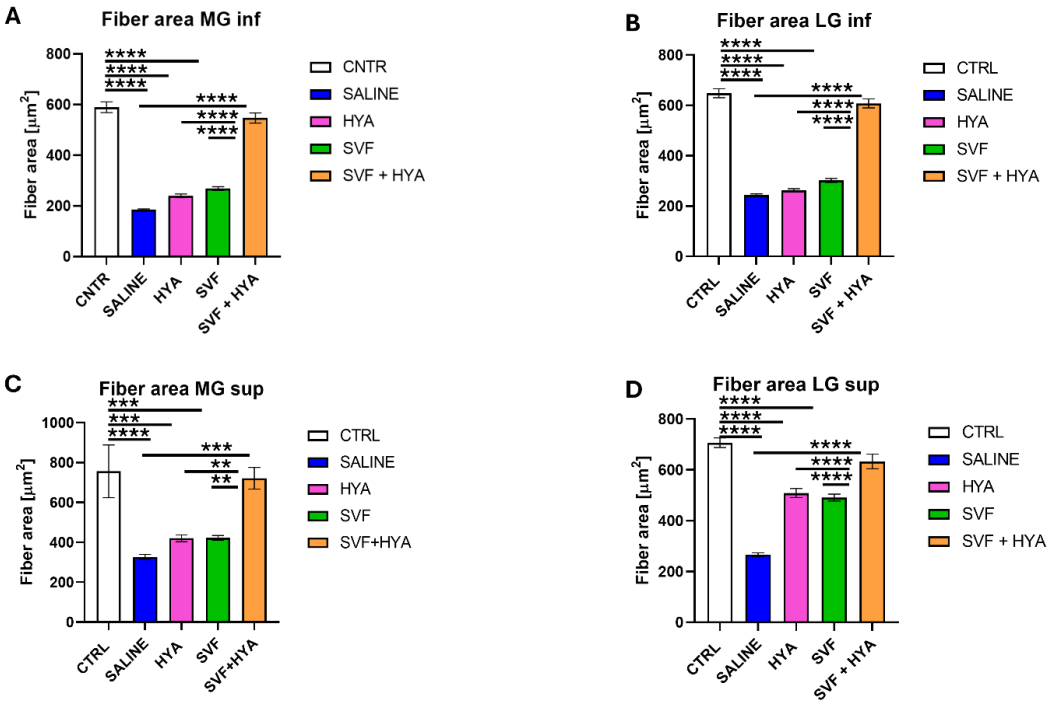

Figure 33. Quantitative analysis of the average area of muscle fibers in inferior and superior MG and LG regions. (**A**) Quantification of fiber muscle average area in inferior MG region (**** $p<0.0001$). (**B**) Quantification of fiber muscle average area in inferior LG region (**** $p<0.0001$). (**C**) Quantification of fiber muscle average area in superior MG region (**** CTRL vs saline $p<0.0001$, *** CTRL vs HYA $p=0.0003$, CTRL vs SVF $p=0.0001$, saline vs SVF+HYA $p=0.0001$; ** HYA vs SVF+HYA $p=0.0073$, SVF vs SVF+HYA $p=0.0052$). (**D**) Quantification of fiber muscle average area in superior LG region (**** $p<0.0001$). For each condition, 4 random fields in inferior and superior MG and LG regions were analyzed, N=3. The data was analysed with One-way ANOVA test. The values were represented as mean ± SEM.

4.5.5 Oil Red O

Since recent studies have confirmed that lipid droplets regulate the function of skeletal muscle satellite cells in tissue regeneration[144], the presence of lipids in the muscle cross-sections from CTRL, saline-, HyA-, SVF-, and SVF+HyA-treated animals were investigated by using Oil Red O (ORO) staining, a lipophilic histochemical method. Cells stained with ORO were absent in the CTRL group (Figure 34A, B) but particularly evident in the samples from animals treated with saline (Figure 34C, D) and to a lesser extent in SVF (Figure 34E, F) or HyA (Figure 34G, H) treated animals. Cells with diffuse cytoplasmic red staining were associated with necrotic and/or immature fibers. In the samples with SVF+HyA, cells stained with ORO were less visible than in the other treated groups (Figure 34I, L).

Quantitative analysis confirmed the histochemical analysis, comparing the percentage of area covered by ORO staining between groups. The analysis revealed a significant increase of ORO-covered area in saline-treated animals compared to CTRL, SVF, HyA, and SVF+HyA groups ($p<0.0001$, Figure 34M, N, O).

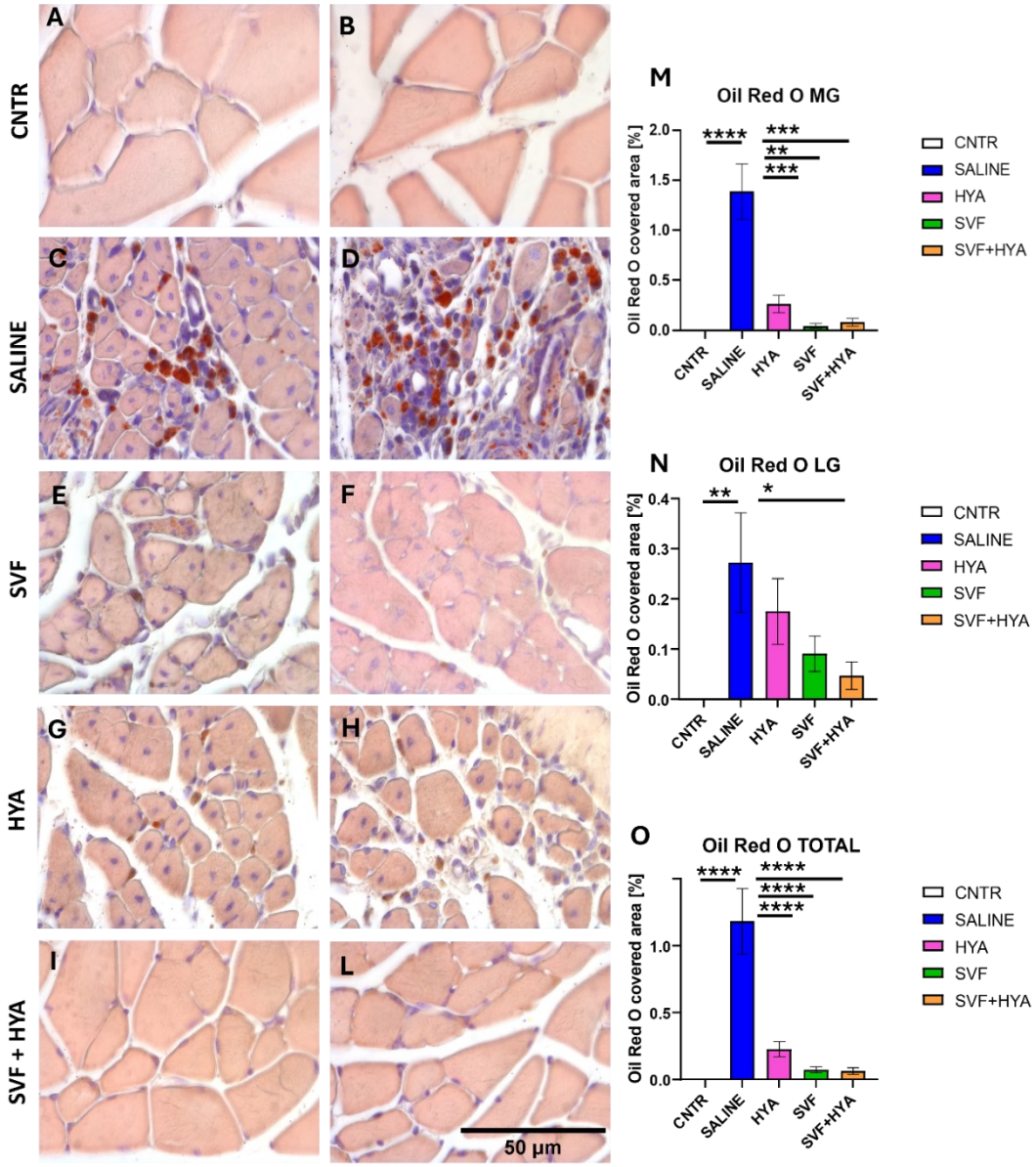

Figure 34. Oil Red O quantification in CTRL, saline, HyA, SVF, and SVF+HyA cross-sectioned gastrocnemius muscles. (**A**) Representative ORO staining images for each group. 40x magnification, scale bar 50 µm. (**B**) Quantification of ORO-covered area of MG region (*** CTRL vs saline p< 0.0001, *** saline vs HyA p=0.0008, ** saline vs SVF p=0.0016, *** saline vs SVF+HyA p=0.0003). (**C**) Quantification of ORO-covered area of LG region (** CTRL vs saline p=0.0095, * saline vs SVF+HyA p=0.0442). (**D**) Quantification of ORO-covered area of total gastrocnemius (**** CNTR vs saline p<0.0001, **** saline vs HyA p<0.0001, **** saline vs SVF p<0.0001, **** saline vs SVF+HyA p<0.0001). For each condition, 5 random fields in MG and LG regions were analysed, N=3. The data was analysed with One-way ANOVA test. The values were represented as mean ± SEM.

4.5.6 Immunohistochemistry evaluation

4.5.6.1 Myosin fast and slow

In samples from CTRL animals, normal myofibers of superficial regions of LG and MG were uniformly labeled with myosin fast (MyoF) and lacked myosin slow (MyoS; Figure 35A, B). Conversely, complementarity or coexpression of MyoF and MyoS staining was present in areas adjacent to the plantar and soleus (Figure 35C, D), confirming that different MyHC isoforms exist in the mouse gastrocnemius muscle. This result was consistently observed in muscle sections of all groups studied.

In muscle cross-sections from I/R injured saline-treated animals, both LG and MG regions showed MyoF immunoreactivity of variable distribution and intensity (Figure 35E). MyoS was absent in the majority of areas with MyoF-positive fibers (Figure 35F).

Fibers recognized as necrotic with H&E analysis displayed MyoF and MyoS labeling, which was similar to that observed in sections used as negative control and therefore considered as non-specific staining (Figure 35G, H). Some fibers showed a strong MyoF labeling in the sub-sarcolemma, which was reflected in the appearance and staining intensity of the muscle morphological abnormalities defined as tubular aggregates (Figure 35E).

In samples of animals treated with SVF or HyA, no difference in the superior regions of MG and LG was detectable in comparison with the controls (Figure 36A, B, E, F), while in the deeper regions with numerous regenerating fibers, MyoF was present in the hole myofiber cross-section but with varying intensity of expression (Figure 36C, D, G, H). Tubular aggregates-like structures with intense MyoF immunoreactivity were observed in both groups but were more prevalent in fibers from SVF-treated animals (Figure 36A, C, E, G).

Muscle cross-sections of SVF+HyA-treated animals displayed similar characteristics to those observed in CTRL. Specifically, MyoF expression was more prevalent than MyoS and distributed internally to fibers homogeneously (Figure

37A-F). Sections used as negative control lacked MyoF or MyoS expression (Figure 37G, H).

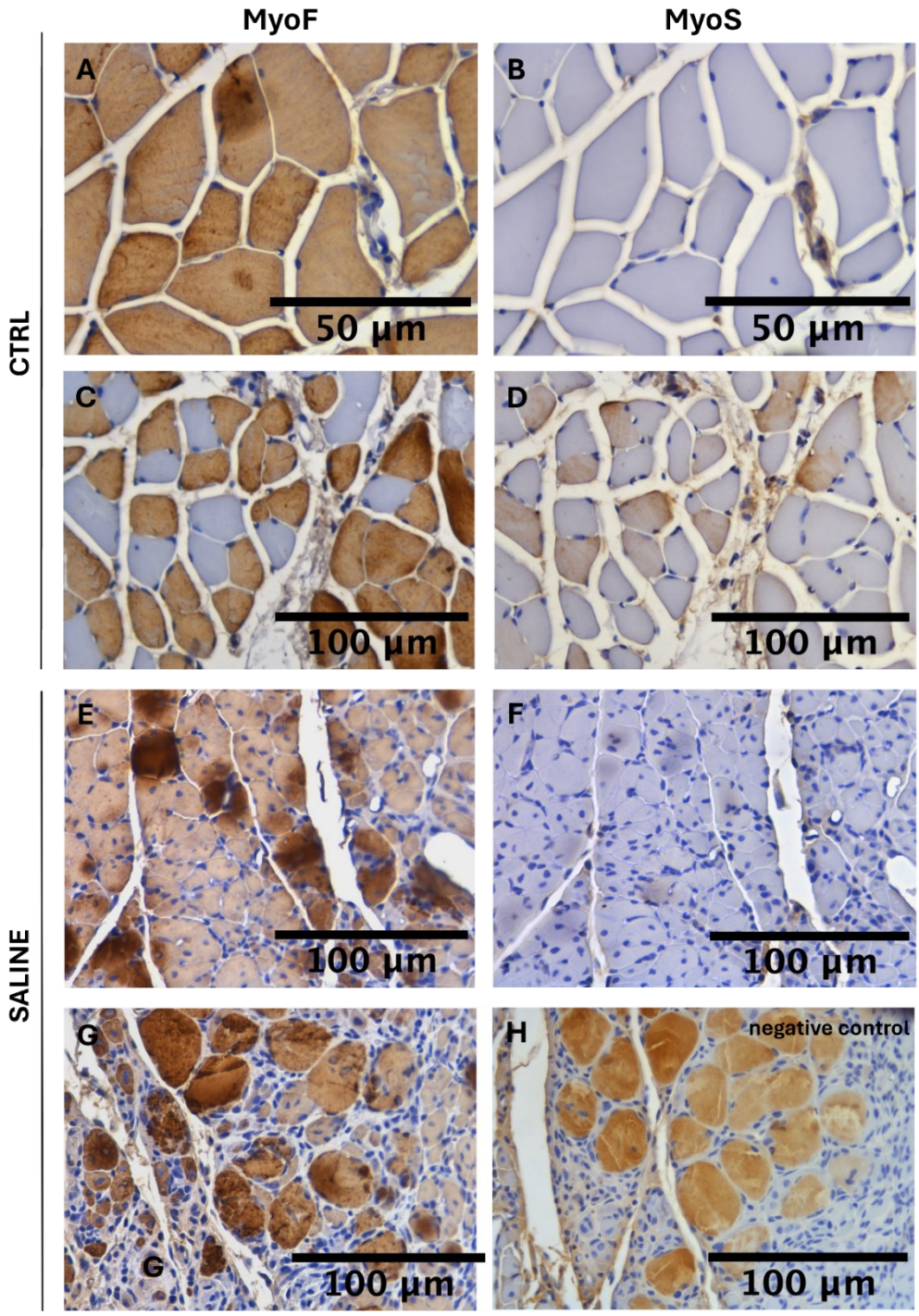

Figure 35. Immunohistochemistry with MyoF and MyoS antibodies in adjacent cross-sections of the gastrocnemius muscle 18 dpi of CNTR and saline groups. (**A, B**) 40x magnification, scale bar 50 µm. (**C, D, E, F, G, H**) 20x magnification, scale bar 100 µm. For each condition, N=3.

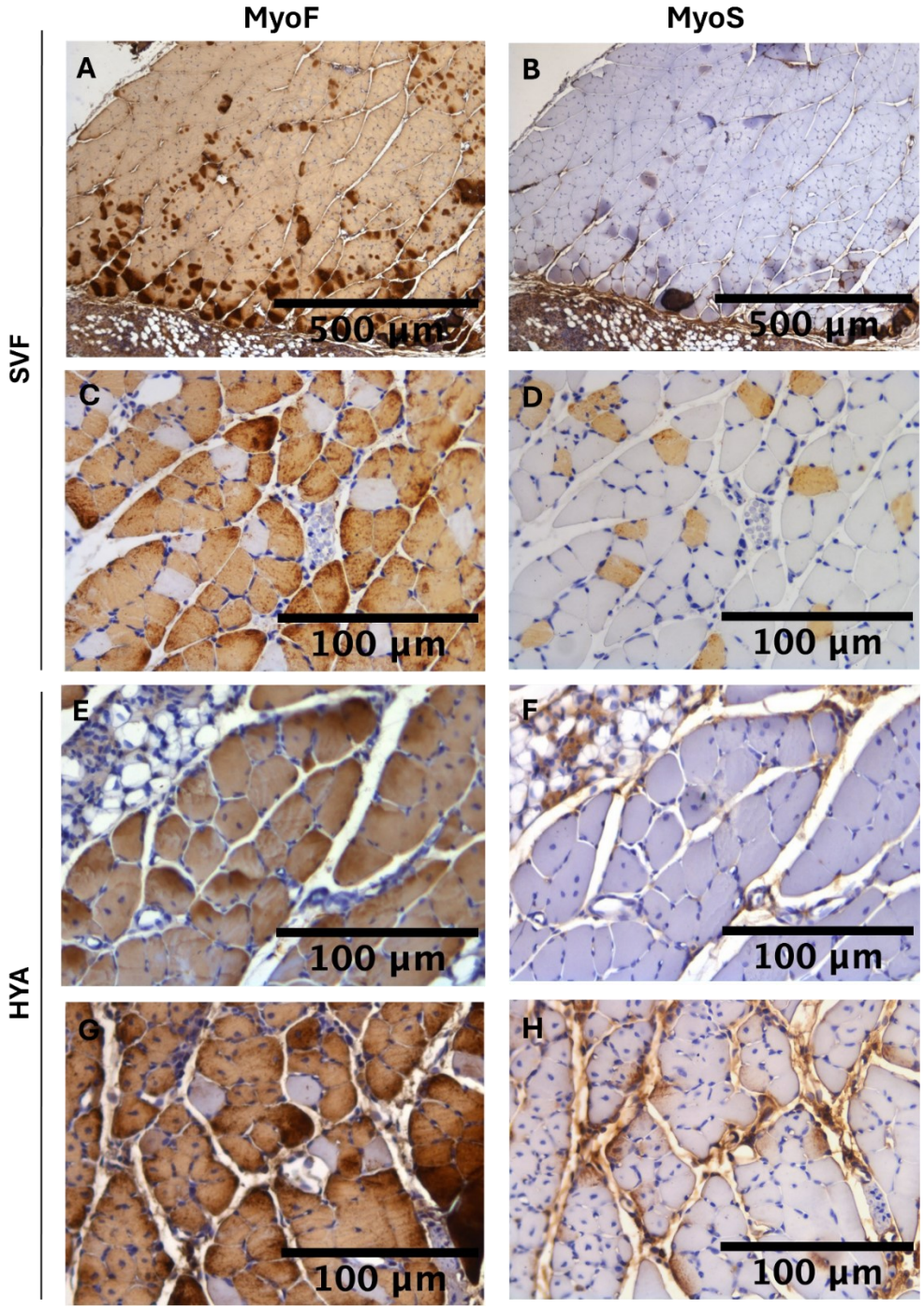

Figure 36. Immunohistochemistry with MyoF and MyoS antibodies in adjacent cross-sections of the gastrocnemius muscle 18 dpi of SVF and HyA groups. (**A, B**) 4x magnification, scale bar 500 µm. (**C, D, E, F, G, H**) 20x magnification, scale bar 100 µm. For each condition, N=3.

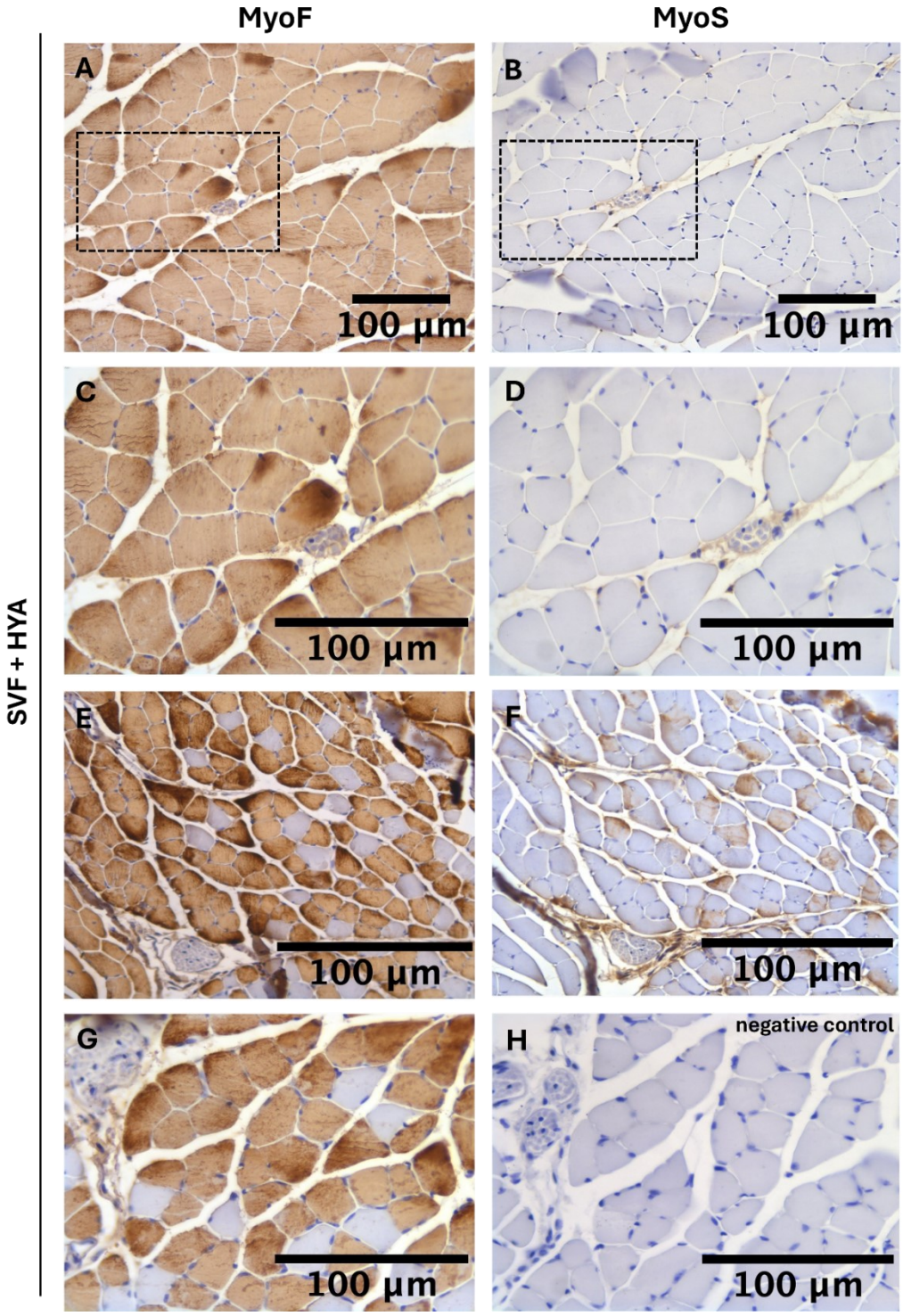

Figure 37. Immunohistochemistry with MyoF and MyoS antibodies in adjacent cross-sections of the gastrocnemius muscle 18 dpi of SVF+HyA groups. (**H**) Negative control. (**A, B, E, F**) 10x magnification, scale bar 100 µm. (**C, D, G, H**) 20x magnification, scale bar 100 µm. For each condition, N=3

4.5.6.2 Desmin

In cross-sections of the gastrocnemius muscle from CTRL animals, the localization of desmin was uniformly distributed in fibers that showed immunoreactivity in organized and regularly horizontal striations, indicative of normal myofibrillar architecture. However, the expression intensity appeared weak in the upper MG and LG regions and marked in the central area of both the inferior MG and LG regions (Figure 38A-H). Furthermore, some myofibers had dense desmin staining in restricted subsarcolemmal areas (Figure 38B, D, F).

Muscle sections from saline-treated animals displayed a large variability for desmin localization. Fibers of the peripheral areas of the MG and LG regions showed desmin distributed with a normal striated pattern, similar to that observed in the controls (Figure 39A-D). Instead, myofibers in the central portion of these regions, characterized by small diameter and centrally positioned nuclei, showed desmin distributed as grainy dots with variable intensity of expression, covering the entire surface or a limited portion of the fibers (Figure 39C-H). Such distribution likely reflected the disorganization of the myofibrillar apparatus. Desmin-positive subsarcolemmal aggregates were observed in some myofibers (Figure 39G, H).

Similarly, in samples from animals treated with SVF or HyA, fibers from the more peripheral areas revealed a desmin-striated expression pattern but with less regular and uniform horizontal striations than those observed in the controls (Figure 40A; 41A, C). The central areas of the muscle were always characterized by the presence of immature fibers in which desmin was localized as large or fine grainy dots, totally or partially scattered within the fibers (Figure 40 B-H; Figure 41B-H). Intense desmin staining was visible in the subsarcolemmal aggregates (Figure 40D; Figure 41G, H).

In the upper MG and LG regions of SVF+HyA treated animals, desmin was distributed in a normal-cross-striated pattern as in controls (Figure 42A-D). In the central area of the muscle, fibers characterized by a polygonal morphology and a peripheral nucleus revealed a desmin granular pattern, which was expressed with more intensity in some parts of the fibers sections (Figure 42E, F, H).

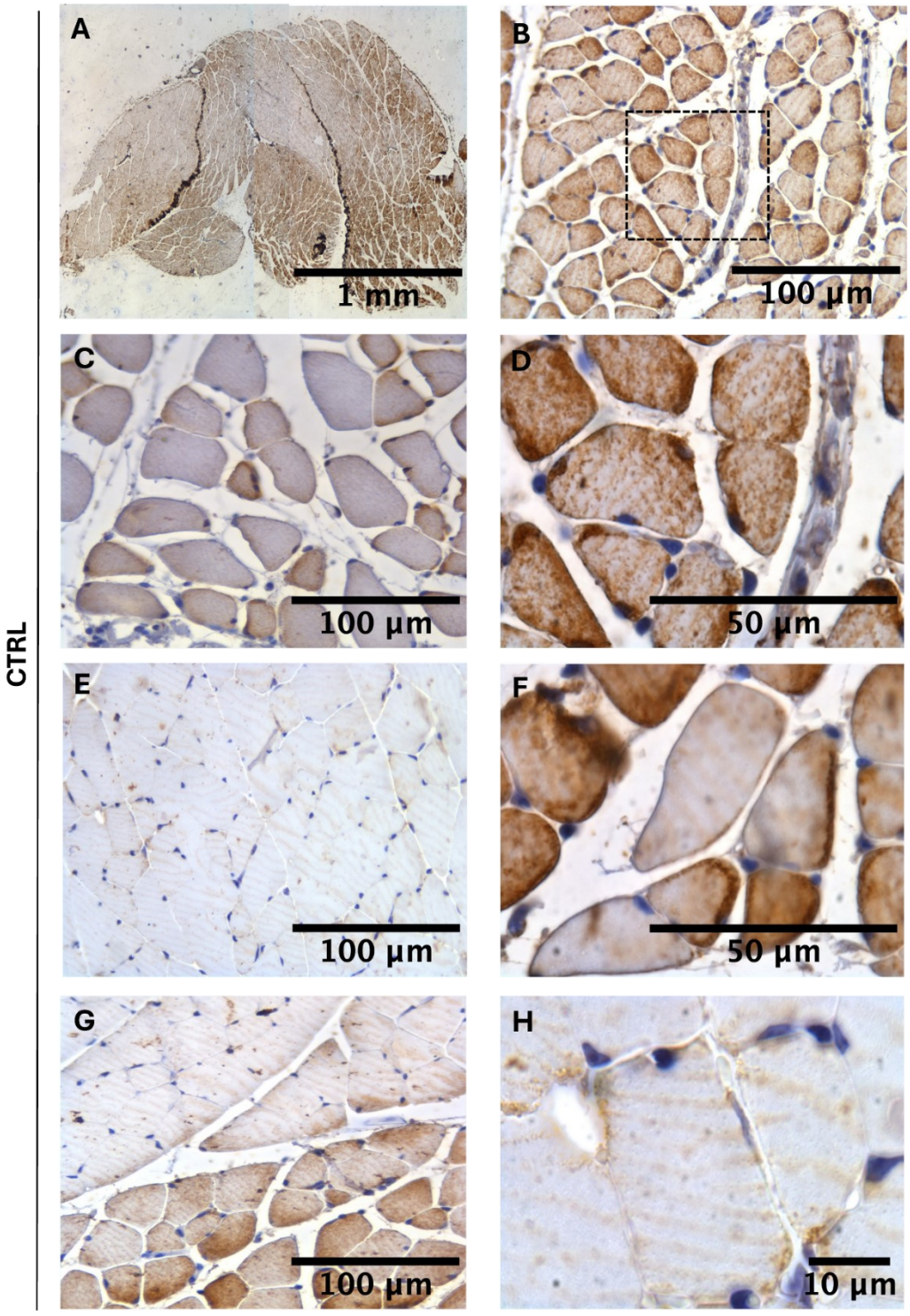

Figure 38. Immunohistochemistry with desmin antibody of the gastrocnemius muscle 18 dpi of CTRL groups. (**A**) 2x magnification, scale bar 1 mm. (**B, C, E, G**) 20x magnification, scale bar 100 µm. (**D, F**) 60x magnification, scale bar 50 µm. (**H**) 100x magnification, scale bar 10 µm. N=3.

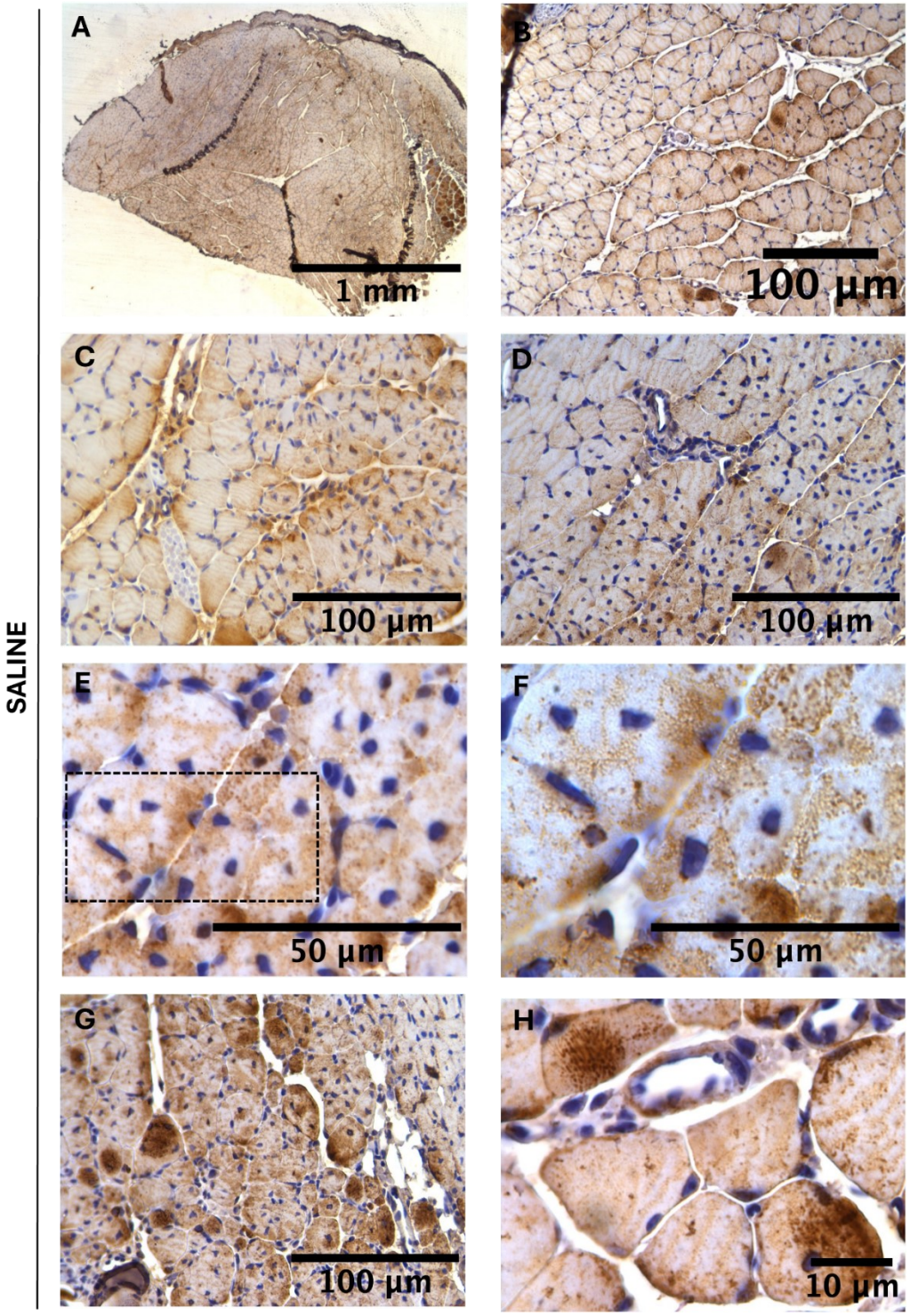

Figure 39. Immunohistochemistry with desmin antibody of the gastrocnemius muscle 18 dpi of saline groups. (**A**) 2x magnification, scale bar 1 mm. (**B, C, D, G**) 20x magnification, scale bar 100 µm. (**E, F**) 60x magnification, scale bar 50 µm. (**H**) 100x magnification, scale bar 10 µm. N=3.

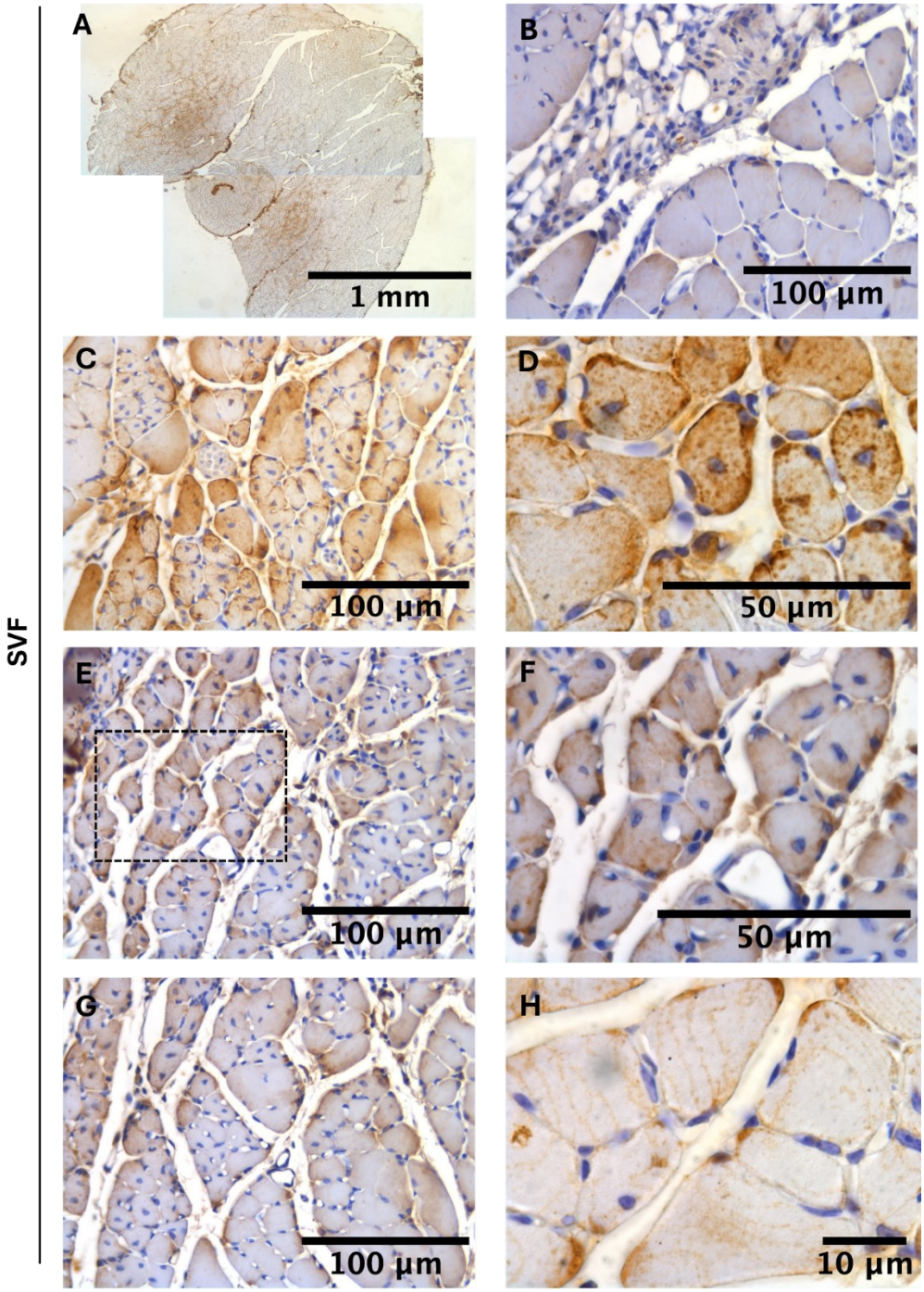

Figure 40. Immunohistochemistry with desmin antibody of the gastrocnemius muscle 18 dpi of SVF groups. (**A**) 2x magnification, scale bar 1 mm. (**B, C, E, G**) 20x magnification, scale bar 100 µm. (**D, F**) 60x magnification, scale bar 50 µm. (**H**) 100x magnification, scale bar 10 µm. N=3.

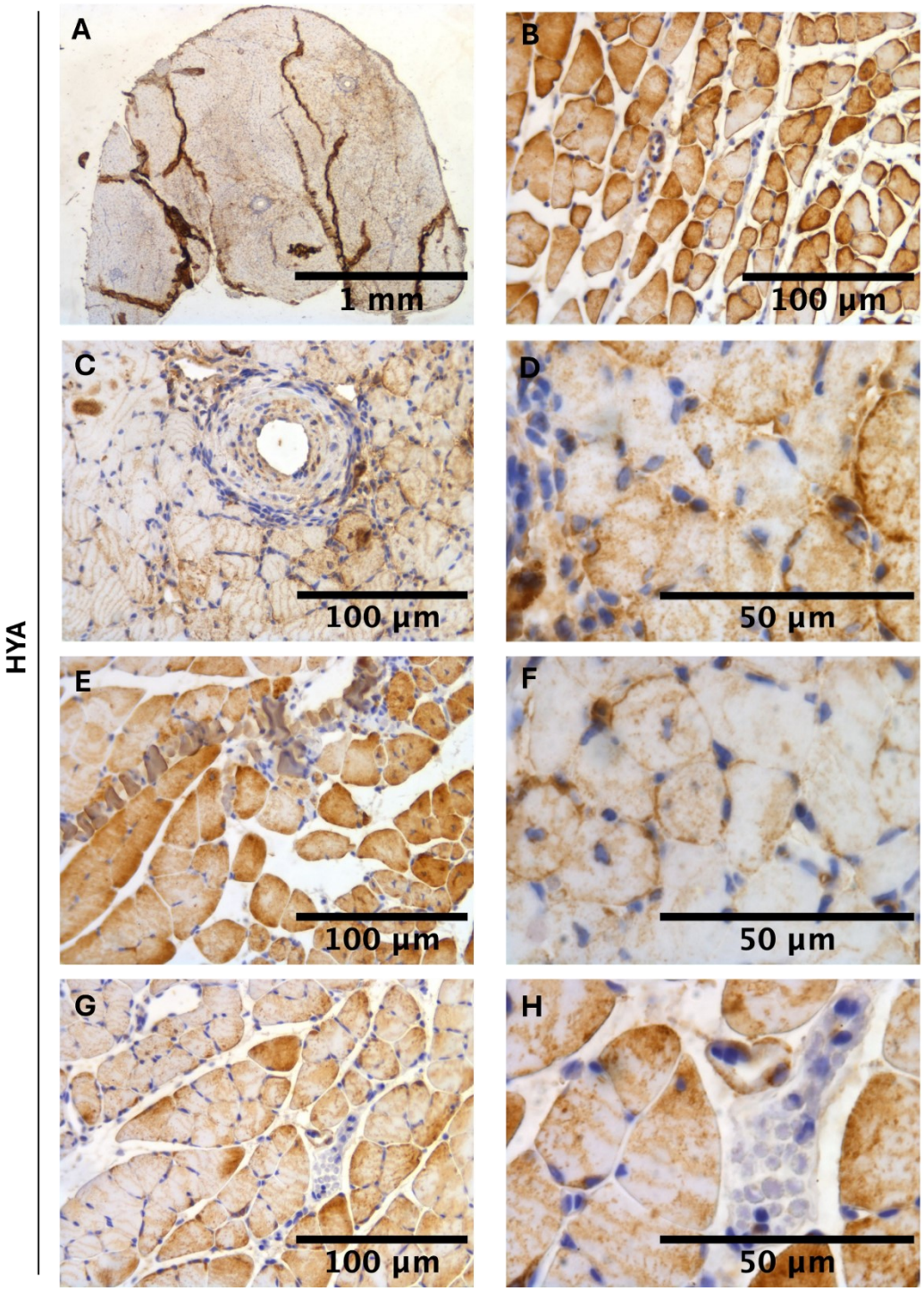

Figure 41. Immunohistochemistry with desmin antibody of the gastrocnemius muscle 18 dpi of HyA groups. (**A**) 2x magnification, scale bar 1 mm. (**B, C, E, G**) 20x magnification, scale bar 100 µm. (**D, F, H**) 60x magnification, scale bar 50 µm. N=3.

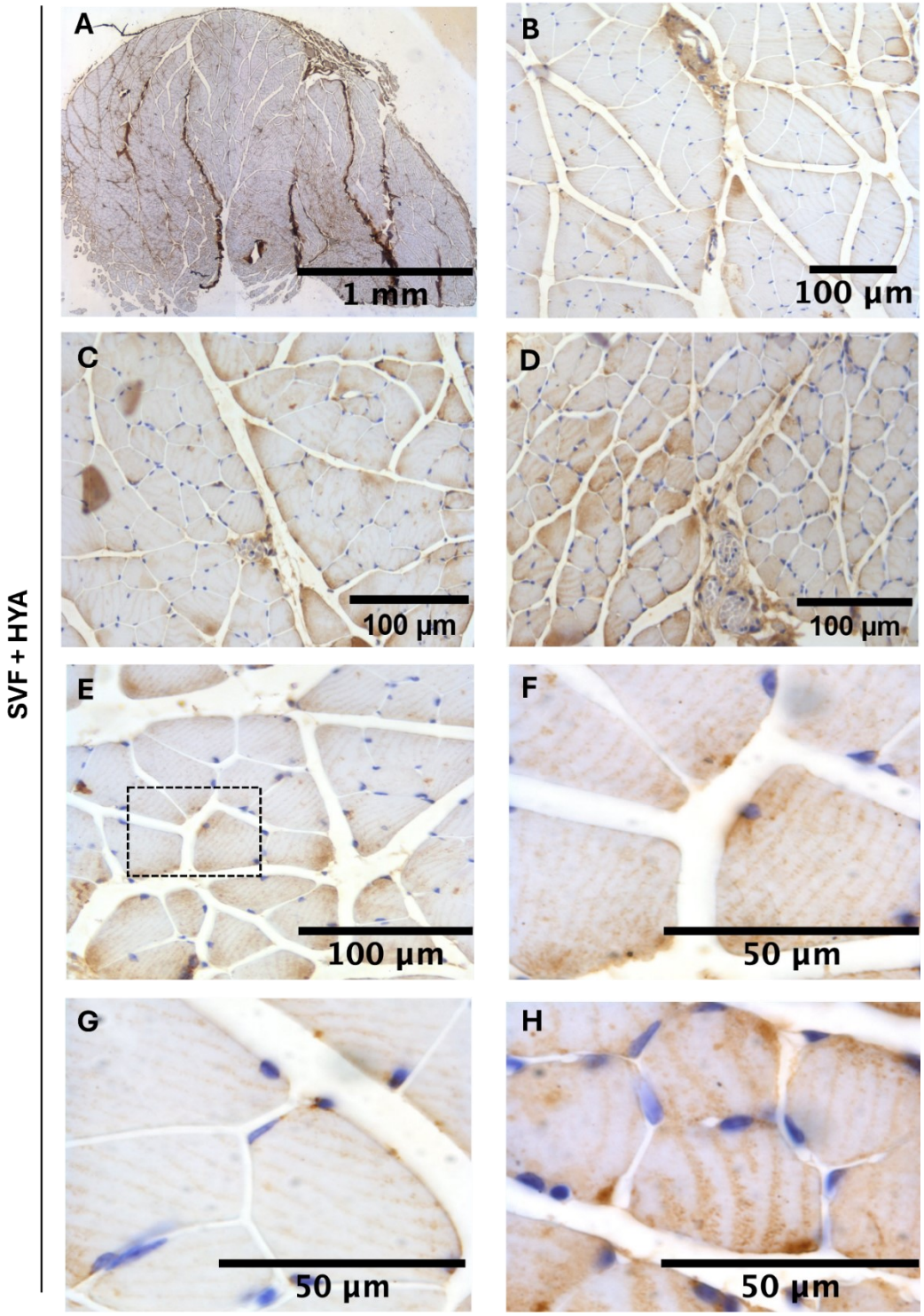

Figure 42. Immunohistochemistry with desmin antibody of the gastrocnemius muscle 18 dpi of SVF+HyA groups. (**A**) 2x magnification, scale bar 1 mm. (**B, C, D, E**) 20x magnification, scale bar 100 µm. (**F, G, H**) 60x magnification, scale bar 50 µm. N=3.

4.5.6.3 Pax 7

The expression of Pax7 in gastrocnemius from CTRL group was detected in cells localized closely to the blood vessels (Figure 43A). No Pax7 immunoreactivity was found near the basal lamina of the muscle fibers.

Conversely, in I/R injury animals treated with saline, numerous Pax7-positive cells were observed in specific areas of the muscle, mainly in the regenerative ones, characterized by immature fibers with central nuclei, and in those with necrotic fibers where Pax7 immunoreactive cells were arranged around to the clear spaces resulting from phagocytosis (Figure 43B, C). Furthermore, Pax7-positive cells were observed adherent to the endothelium of vessels located within or adjacent to areas with necrotic fibers, indicating possible recruitment and transport of satellite cells via the bloodstream to the injury site (Figure 43D).

In samples from SVF- and HyA-treated animals, Pax7 immunoreactivity was detected in the regenerative areas of MG and LG and expressed in numerous cells located in proximity to blood vessels or in the basal lamina of myofibers (Figure 44A, C). Clusters of numerous Pax7 immunoreactive cells were observed in the areas of necrotic fibers and/or in the connective tissue, likely representing proliferating satellite cells (Figure 44B, D).

In samples from animals treated with SVF+HyA, Pax7-positive cells were still present, not concentrated in specific areas but scattered throughout the muscle and adjacent to myofibers or vessels (Figure 45A-D). Sections used as negative control lacked Pax7 or CCL5 expression (Figure 45H).

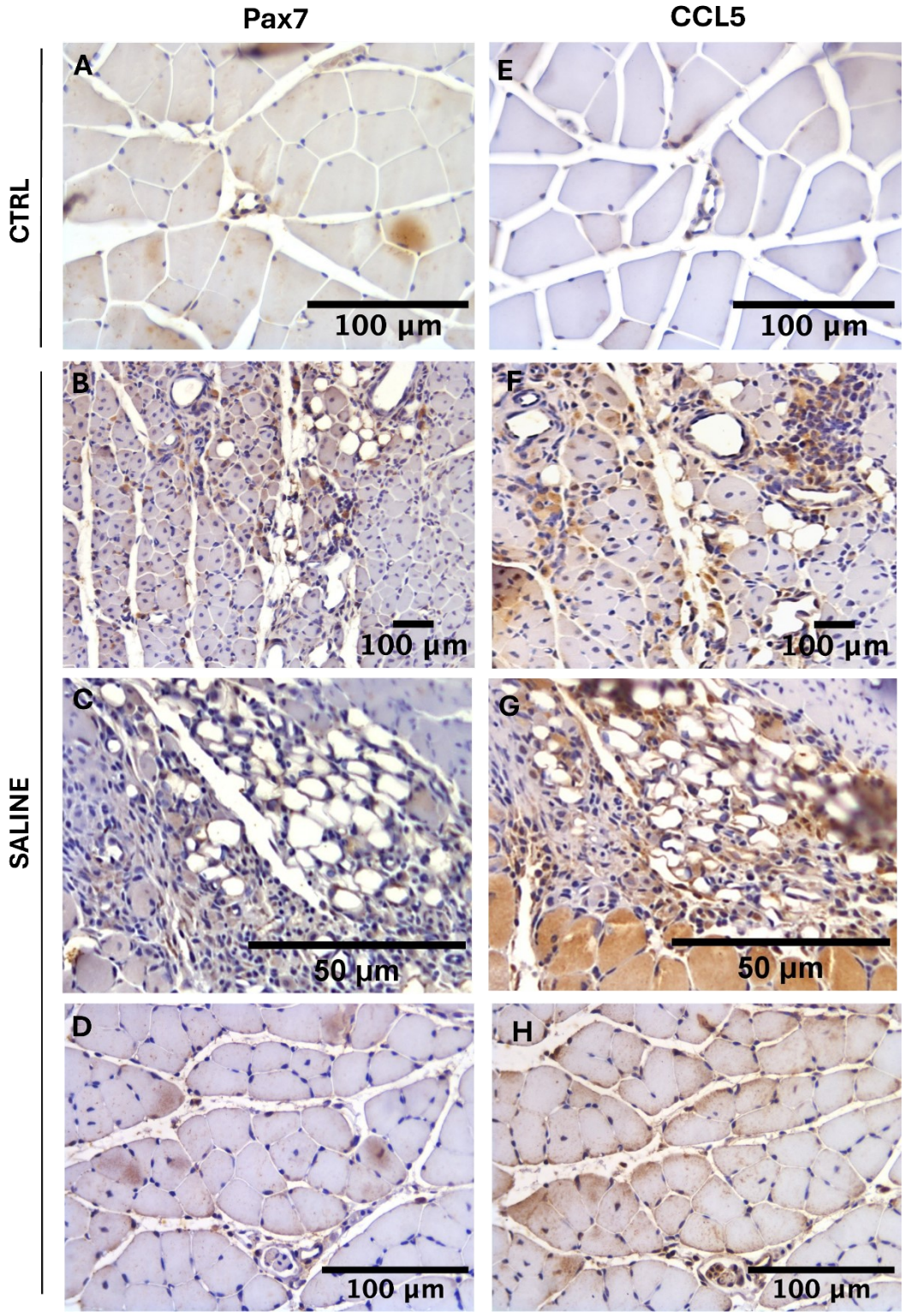

Figure 43. Immunohistochemistry with Pax7 and CCL5 antibodies in adjacent cross-section of the gastrocnemius muscle 18 dpi of CTRL and saline groups. (**A, C, D, E, H**) 20x magnification, scale bar 100 µm. (**C, G**) 40x magnification, scale bar 50 µm. For each condition, N=3.

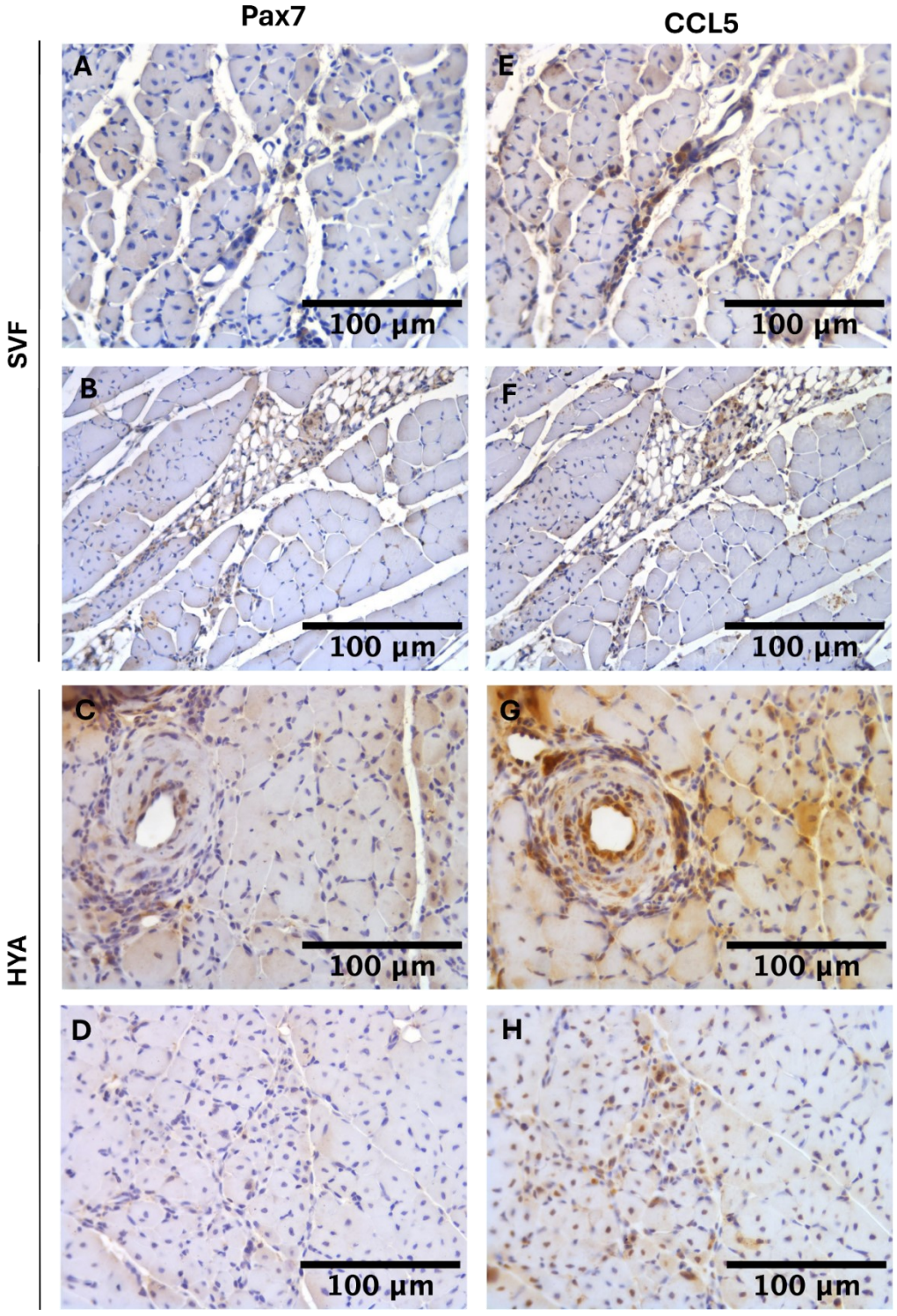

Figure 44. Immunohistochemistry with Pax7 and CCL5 antibodies in adjacent cross-section of the gastrocnemius muscle 18 dpi of SVF and HyA groups. (**A-H**) 20x magnification, scale bar 100 µm. For each condition, N=3.

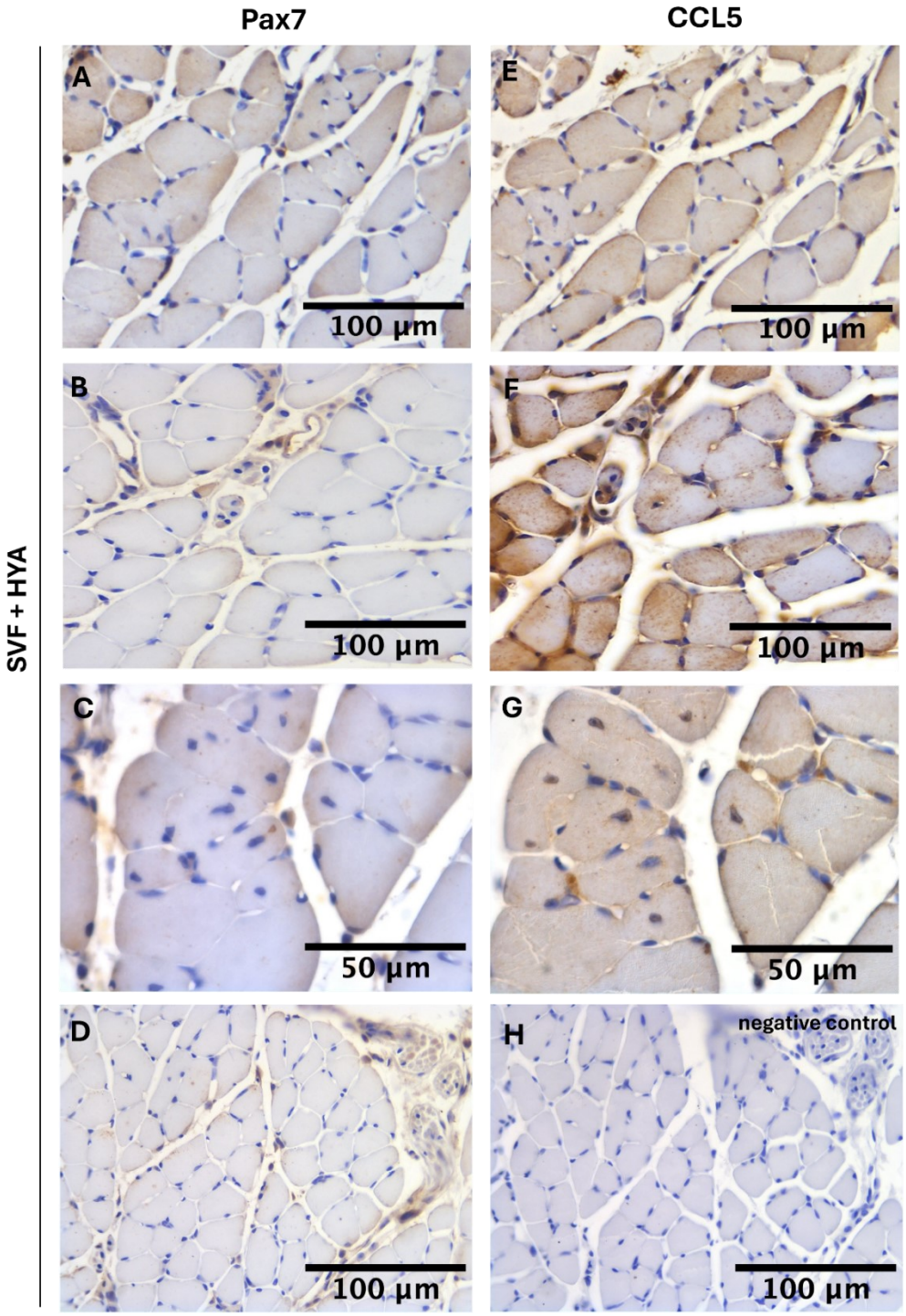

Figure 45. Immunohistochemistry with Pax7 and CCL5 antibodies in adjacent cross-section of the gastrocnemius muscle 18 dpi of SVF+HyA groups. (**H**) Negative control. (**A, B, D, E, F, H**) 20x magnification, scale bar 100 µm. (**C, G**) 40x magnification, scale bar 100 µm. For each condition, N=3.

4.5.6.4 CCL5

Cross-sectioned muscles from CTRL showed a few CCL5-immunoreactive cells localized near the sarcolemma of some fibers or near blood vessels (Figure 43E).

The I/R injured saline-treated animals showed a pronounced expression of CCL5 in the gastrocnemius muscle. Immunolabeled cells were distributed throughout the connective tissue between muscle fibers or in close apposition to the surface of immature fibers or in proximity to blood vessels (Figure 43F-H). A comparison of Pax7 and CCL5 immunostaining in adjacent sections revealed that Pax7-positive cells were present in the same areas with CCL5 immunoreactivity, which was more evident than Pax-7 (Figure 43A-D and E-H, respectively).

A similar distribution and expression pattern of CCL5 was also evident in the muscle sections of animals treated with SVF and HyA, with a consistent presence of CCL5-positive cells in the connective tissue between the regenerating fibers and around the vessels (Figure 44E, F and G, H, respectively). In adjacent sections CCL5 immunostaining appeared more evident than Pax7.

Samples from SVF+HyA-treated animals showed a CCL5 labeling pattern similar to that observed in CTRL. Its expression appeared to be in close proximity to vessels or close apposition to the surface of a few muscle fibers (Figure 45E-G).

4.6 Characterization of human adipose tissue supernatant obtained by Stromal Vascular Fraction

4.6.1 NTA analysis

The supernatant phase of the human adipose tissue, obtained after mechanical fragmentation and used for I/R injury experiments, was analysed to understand the content in terms of extracellular vesicles (EVs). The NTA data provided an EVs concentration average of $2.34 \times 10^{11} \pm 3.69 \times 10^{11}$ particles/ml, with an average size of 132.25 ± 15.38 nm (Figure 46A, B).

The TEM images confirmed the presence of a population of vesicles in the supernatant phase of the mechanically fragmented human adipose tissue (Figure

46C, D, E). Vesicles were characterized by an external membrane composed of a lipid bilayer, with a size variable from 50 to 700 nm.

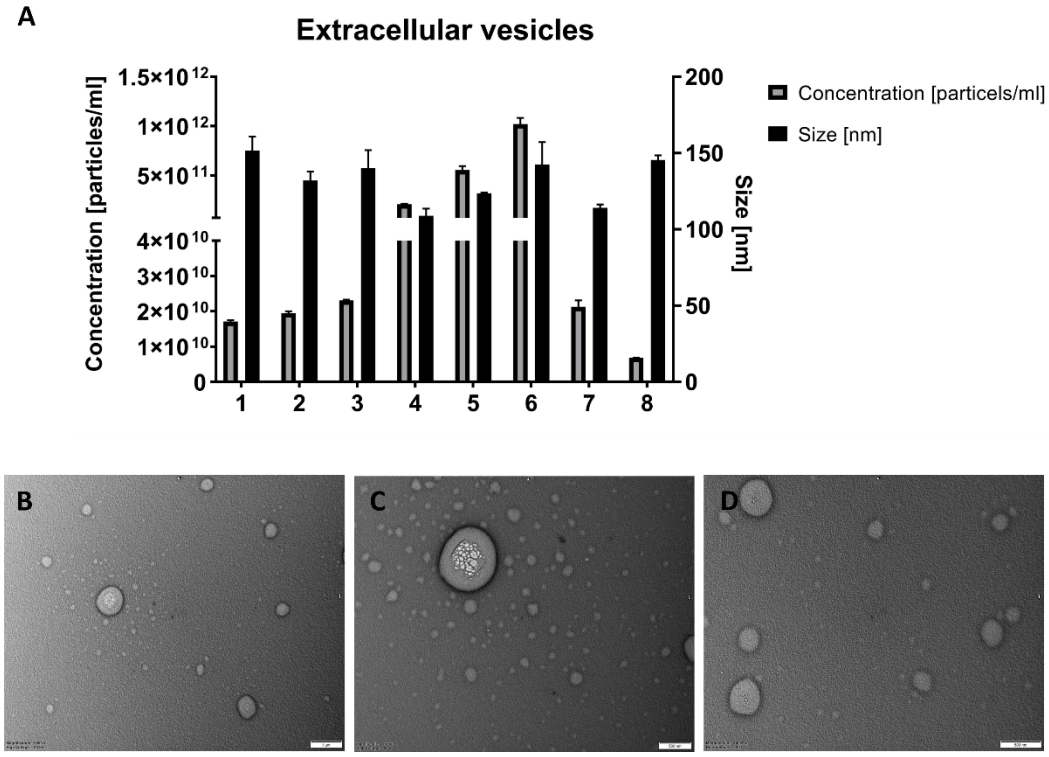

Figure 46. Extracellular vesicles from the supernatant phase of the human adipose tissue after mechanical fragmentation with HT-SVF kit. (**A**) NTA analysis showed a EVs concentration and size of 8 samples (in x axis). (**B, C, D**) TEM images stained with lead citrate confirmed the presence of EVs ranging from 50 to 700 nm. Scale bar 1µm (C), 500nm (D, E). N=8.

4.6.2 Western blot

Human adipose tissue supernatants were collected, and small EVs were enriched using an exosome isolation kit. To analyse supernatant content and confirm EVs isolation and purity, western blot analysis of specific EVs protein markers was performed. Figure 47 reported key proteins commonly found in exosomes like tetraspanins (e.g., CD9, CD63, and CD81), heat shock proteins (HSP70), cell surface adhesion protein (CD62L), and components associated with the endosomal sorting complexes required for transport (ESCRT) such as Alix and TSG101. GM130 and Calnexin were used to exclude potential contaminants originating from the Golgi apparatus or endoplasmic reticulum during the EVs enrichment process.

These findings indicate that the supernatants obtained through mechanical micro-fragmentation with SVF Hy-Tissue contain a distinct population of extracellular vesicles released by the cells within the stromal vascular fraction.

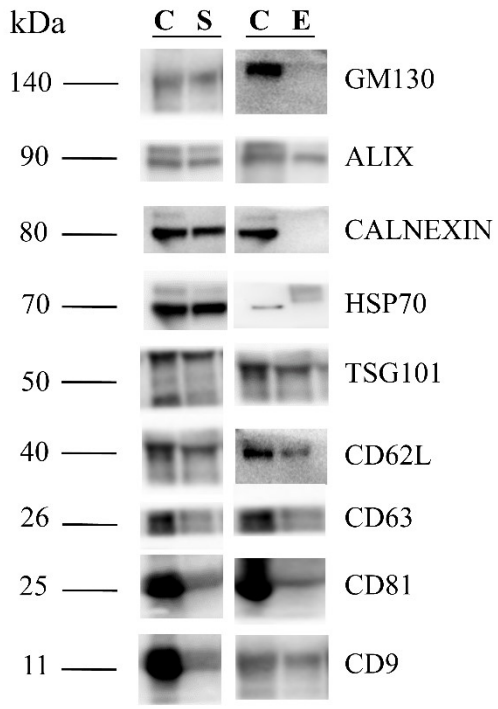

Figure 47. Western blot analysis of specific EVs protein markers. The column on the left is a representative image of the markers used to characterize the supernatant obtained from mechanical micro-fragmentation with SVF Hy-Tissue. The column on the right is a representative image of the markers used to characterize the extracellular vesicles present in the supernatants obtained through mechanical micro-fragmentation with SVF Hy-Tissue. C= cells (human adipose mesenchymal stem cells, positive control); S= supernatant; E= extracellular vesicles. N=8.

4.6.3 Transmission electron microscopy of SVF pellet

Ultrastructural analysis of the SVF pellet revealed the presence of cells characterized by an electron-dense cytoplasm, a large nucleus, and numerous small mitochondria (Figure 48A; 49A, D). The plasma membrane was irregular, with numerous protrusions that increased its surface area. The cytoplasm contained numerous electron-dense lysosomes filled homogeneously with very tiny granules (Figure 48A, E; 49A, B, D).

Single membrane-bound vesicles with the characteristic appearance of multivesicular bodies (MVBs) were scattered in the cytoplasm, and intensely labeled vesicles were clearly visible within them (Figure 48A, E, F; 49A-D). Membrane-bound vesicles, round and approximately 50-70 nm in diameter were present in clusters of three to four units on the outer surface of the plasma membrane (Figure 48 A-D; 49D-F). Due to their appearance and size, they have been identified as exosomes.

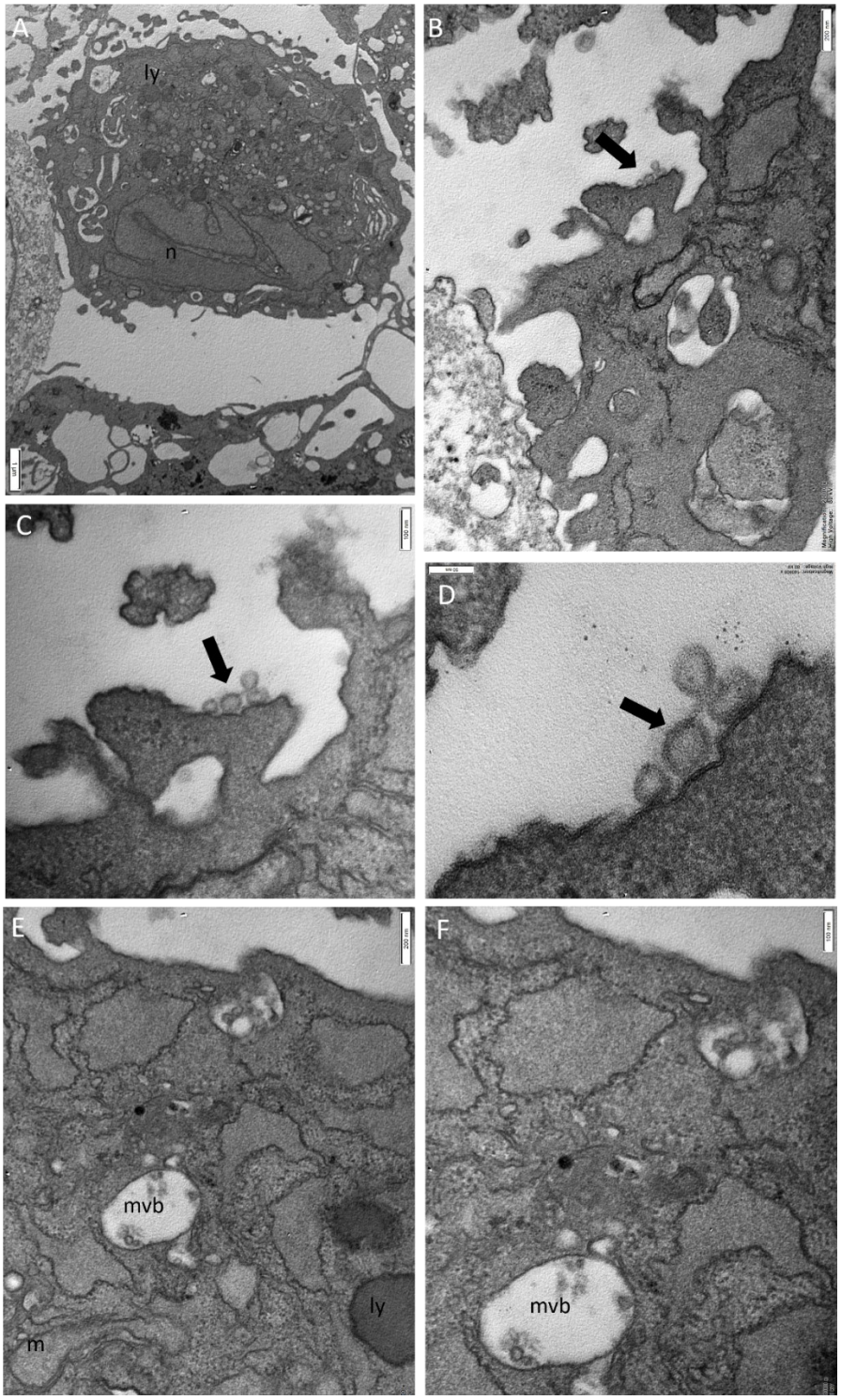

Figure 48. Transmission electron microscopy of the SVF pellet shows multivesicular bodies (MVB) in the cytoplasm and exosomes. Ap. Ly: lysosome, n: nucleus, m: mitochondria, arrow: exosomes, mvb: multivesicular body. Scale bar 1 μm (**A**), 200 nm (**B, E**), 100 nm (**C, F**), 50 nm (**D**).

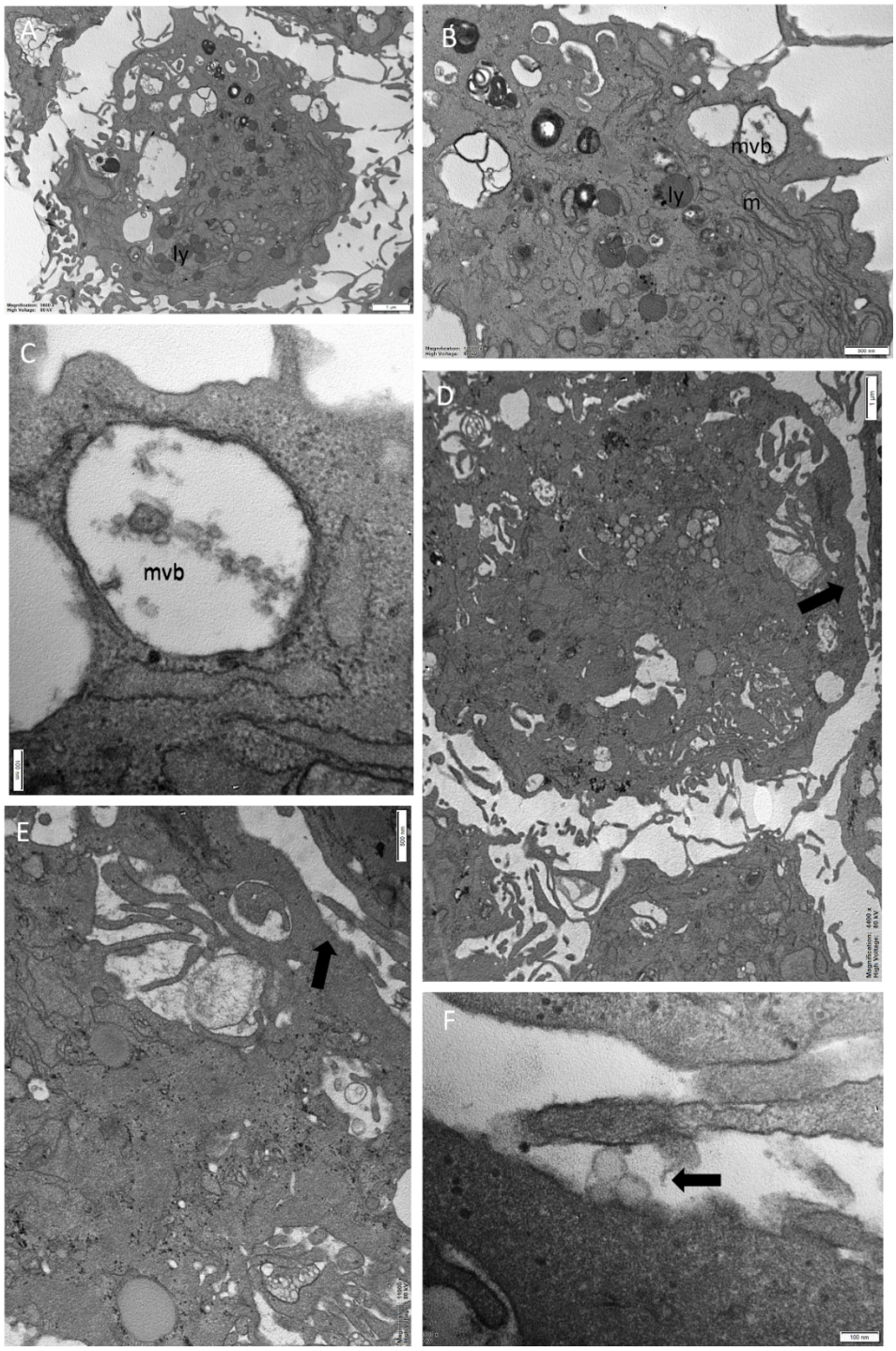

Figure 49. Transmission electron microscopy of the SVF pellet shows multivesicular bodies (MVB) in the cytoplasm and exosomes. Ap. Ly: lysosome, n: nucleus, m: mitochondria, arrow: exosomes, mvb: multivesicular body. Scale bar 1 μm (**A, D**), 500 nm (**B, E**), 100 nm (**C, F**).

5 DISCUSSION

5.1 Characterization of the Stromal Vascular Fraction

The mechanical technique evaluated was simple, providing SVF through free cells and micro-fragmented. Compared to the enzymatic procedures, the Hy-Tissue SVF kit is easier and faster, with a time consumption of 15 minutes, and without problems with the collagenase residual enzymatic activity after the injection. Furthermore, adipose tissue exposed to collagenase has been considered more than "minimally manipulated," defined by the Food and Drug Administration guidance documents as "processing that does not alter the original relevant biological characteristics of cells"[145]. Indeed, enzymatic digestion can result in more cell damage, adversely affecting cell survival and the expression of surface antigens[146]. In addition, the enzymatic isolation standard protocol involves the possibility of introducing xenogeneic components that may pose certain risks and safety issues, such as exposure to infectious agents and immune reactions[147]. To ensure the highest possible patient safety, the Hy-Tissue SVF kit is a closed system that separates the cell from the external environment and reduces the opportunity for error and contamination.

As indicated in other studies, the reported results confirm that the cellular yield of mechanically treated adipose tissue is lower compared to the tissue treated with collagenase (respectively 4.1 x 10^4 cells/ml fat and 5 x 10^5 cells/ml fat). Nevertheless, the Hy-Tissue SVF system allowed recovery of up to 25% of the total SVF, suggesting a high separate efficiency from this methodology. As confirmed by histological and ultrastructural analyses, the statistical difference in cellular yield is caused by intact micro-fragments of connective tissue that include a heterogeneous pool of cells within them. Other mechanical methods produce similar or less nucleated cell yield than Hy-Tissue SVF. For instance, Markarian et al. examined a non-enzymatic procedure with centrifugation that recovered nearly 1 x 10^4 cells/ml of lipoaspirate[148].

The results showed that the mean CFU-F yield of mechanical-treated SVF was lower than the CFU-F yield obtained by the enzymatic digestion of adipose tissue.

This difference could be caused by a partial release of the cellular population within the lipoaspirate (as for the cellular yield) and subsequent maintenance in clusters of some cells with adhesion capabilities, such as AD-MSCs and fibroblasts. However, this result does not imply an inferior potential of mechanical SVF for therapeutic purposes. Indeed, preserving micro-fragment with a cellular pool recreates the physiological stem niche, inducing a high regenerative potential.
As reported in the morphological and flow cytometry analysis, the mechanical disaggregation of adipose tissue allowed the isolation of micro-fragments of connective tissue that include a pool of cells with different phenotypes, such as preserved microvascular elements, endothelial cells, perivascular cells, immune system cells, extra-cellular matrix (ECM) cells, and AD-MSC, consistent with the literature data[149]. These preserved components may have regenerative potential because they recreate an original part of the physiological stem niche together. Indeed, the ECM component is essential to maintain the structure and organization of all the cell components close for the activation and cross-talking process, creating a complex and dynamic entity, as reported by Jones and Wagers[82]. For this reason, micro-fragments could have a superior therapeutic potential for tissue repair and regeneration compared to extracted AD-MSC. Also, AD-MSC expansion is time-consuming, expensive, and poorly controllable, although their use for regenerative methods is widely recognized[150]. Moreover, the AD-MSC inside their preserved staminal niche may prolong their long-term survival and communicate with their original nearby cells. These dynamic complexes can induce proliferative, proangiogenic, anti-apoptotic, and anti-inflammatory effects through paracrine mechanisms and cell-cell contact[151]. For example, it is reported that the cross-talking between AD-MSC and endothelial progenitor cells can induce angiogenesis signaling[152]. Furthermore, the immune components contained in SVF, such as macrophage type 2 and T-regulatory cells, can produce an anti-inflammatory action[153]. The efficacy of SVF application for injury regeneration is already evidenced in the literature. Indeed, in a randomized clinical trial, SVF obtained with a Hy-tissue SVF kit showed improved clinical symptoms and tendon thickness in patients with Achilles tendinopathy[154]. Such evidence confirms the potential regenerative effect of SVF and suggests other possible therapeutic applications.

5.2 Hyaluronic Acid *in vitro* response

The action of hyaluronic acid could modulate the regenerative potential of the SVF. As reported in the literature, HyA is a promising candidate for the tissue regeneration process[155]. Indeed, it can interact with different cell types and pathways and stimulate cellular migration, adhesion, and proliferation.

The HyA can also influence the cell fate determination of MSC[156]. As a reported result, the expanded SVF cells can multilineage differentiate into adipocytes, chondrocytes, or osteocytes. The following experiments showed that expanded SVF cells cultured with hyaluronic acids (HyA1, HyA2, HyA3) differentiated into adipocytes. The maximum non-toxic HyA concentration was chosen for the adipogenesis assay, in which the lipid droplets (LD) accumulation was evaluated with Oil Red O staining (ORO). Quantitative analysis showed that all three HyA stimulated the number of LDs formations, reaching a maximum peach at 21 dpi. Likely, the binding between HyA and CD44 on the cell surface of expanded SVF cells triggers the activation of the adipogenic pathway[157], subsequently forming LDs. The differences observed in the number of LDs formations may be linked to the different chemical compositions of the tested HyA.

Indeed, as reported in the literature, the different molecular weights of hyaluronic acid can impact physicochemical and biological functions[158]. Self-crosslinking HyA (Ial-system ACP, HyA3) induced the highest stimulation of LDs number.

After reaching the peak (21 days), the lipid droplets gradually decrease until the last time point. Simultaneously, between day 21 and day 28, a progressive increase in the area of the LDs was observed. This can be attributed to the normal physiological process of white adipocyte maturation. Indeed, the neoformation of adipocyte phenotype is characterized by an initial progressive triglyceride accumulation in tiny LDs embedded in the cytoplasm, fusing to form larger ones[159, 160]. This physiological process could be stimulated and reinforced by HyA interacting with the surface receptors of the cells.

Respectively, Nadra et al. found that cross-linked HyA in contact with pre-adipocytes significantly increased the number of differentiated cells and led to a

better evolution of lipolysis during prolonged cell cultured[161]. Also, Stellavato et al. reported an enhancement of adipogenic differentiation of AD-MSCs in contact with HyA [162, 163]. A hyaluronan hybrid cooperative complex significantly influences AD-MSC differentiation by up-regulating adipogenic genes and related proteins. Histological analysis confirmed a high presence of LDs.

The stimulation of new adipose tissue formation by HyA may benefit numerous applications. For example, aesthetic medicine promotes facial rejuvenation and wrinkles corrects facial lipoatrophy and augments soft tissue. The capacity of preadipocytes to differentiate and accumulate lipids deteriorates with aging, and HyA can be helpful as a stimulator[164].

Another possible application is injection into joints to prevent the loss of articular fat pads (AFPs). For example, the Hoffa fat pad is an active compound of the joint organ with multifunctional roles in maintaining joint homeostasis[165]. Loss of HFP in the knee can cause pathological joint states, such as anterior knee pain and osteoarthritis. Local injection of hyaluronic acid could promote stimulation, proliferation, and adipogenic phenotypic shift of stem cell niches[165].

5.3 *In vivo* regenerative potential of Hyaluronic Acids and Stromal Vascular Fraction

Nowadays, autologous stromal vascular fraction transplantation can be considered a source of regenerative potential. Indeed, thanks to its preserved composition, it could be a complex and dynamic entity that recreates the physiological stem niche. The SVF heterogeneity generated paracrine crosstalk with each other and the surrounding environment, which could trigger the regenerative potential (see the characterization of SVF in Chapter 1). In addition, autologous transplantation of SVF can bypass the legal issues of expansion of AD-MSC and reduce the risks and inconveniences associated with cell cultures and multiple passages[166]. The principal limit of the SVF application can be the locus maintenance of the cellular product. To overcome this problem, hyaluronic acid could be used. HyA is an essential component of the ECM, and it provides excellent biocompatibility and is a nonimmunogenic agent. Literature also reported that HyA participates in multiple

biological functions, such as lubrification, hydration, and ECM structure, and interacts with different cell pathways, stimulating proliferation, differentiation, and migration[155]. Indeed, in Chapter 2, it was described that the three HyA products in contact with the adherent SVF cells could stimulate adipogenic differentiation. After the *in vitro* characterization of human SVF and adipogenic stimulation between hyaluronic acids and SVF, an *in vivo* test was performed.

In this second chapter, nude mice were subcutaneously injected with the human mechanical extracted SVF with the three hyaluronic acids to understand their possible regenerative potential. Regenerative capacity was evaluated regarding the ability to form new adipose tissue. The results showed that all the SVF and HyA injected sides were characterized by a neoformation of adipose tissue. The principal differences consisted of different time points for the neoformation of adipose tissue. Mice injected with SVF mixed with HyA3 showed adipogenic stimulation starting from 7 dpi, faster than the SVF mixed with HyA1 or HyA2 (respectively 14 and 30 dpi). These data were supported by the MRI acquisition, in which T2-w fat suppression on and off imagines defined the presence of well-structured adipose tissue. The H-NMR spectroscopy also confirmed the new fat formation, which identified the typical chemical spectrum of adipose tissue. Microscopical examination supported the MRI results but showed the presence of adipose tissue with different morphology. Indeed, examined tissue stimulated by HyA1 or HyA3 mixed with SVF was characterized by a small size of adipocytes supported by defined ECM septa and with micro-vessels useful for tissue maintenance. Differently, the HyA2 with SVF formed large adipocytes interposed by fibrotic and inflamed connective tissue. The chemical composition of HyA could induce different modulations, causing differences in the temporal evolution and morphology of adipose tissue neoformation. On the contrary, no adipose tissue neoformation was observed in all contralateral sides injected with only respective HyA.

Differently, the majority of literature reports on the *in vivo* capacity for neoformation of adipose tissue mixing a hyaluronic acid with AD-MSC. Huang et al., after a subcutaneous injection of human AD-MSC with a HyA gel, showed a complete proliferation and differentiation of adipose tissue with histological Oil-

Red O stain[167]. Also, Karsten et al. observed islets of mature adipocytes and vessels embedded in fat tissue after injecting AD-MSC with HYADD4 gels[168]. The effects of the regenerative potential of SVF with a hyaluronic acid were evaluated in osteochondral defects. Abdullah et al. observed an improvement in osteochondral regeneration with accelerated cartilage regeneration in rabbit femoral microfracture[169].

An immunofluorescent assay with human leukocyte antigen (HLA) antibody was performed to understand the mechanism of action of SVF mixed with HyA. The analysis showed a slight no positive fluorescent signal from 30dpi in all treated animals. These results suggested that the injected human SVF mixed with HyA stimulated the physiological mouse stem niche to differentiate into adipose tissue. Human SVF can have a positive modulation, releasing molecules and factors that activate the mice stem niche. Thanks to the porosity structure of the HyA, the paracrine effect of SVF can interact with the microenvironment. Cross-taking stimulation signaling could be associated with the release of extracellular vesicles from SVF. Indeed, EVs can include paracrine mediators, such as proteins, nucleic acids, and enzymes that stimulate the proliferation and differentiation of physiological stem niches[169]. Chen et al. demonstrated that exosomes extracted from AD-MSC exerted a pro-adipogenic effect and increased collagen synthesis levels in mice[170].

Based on the results, HyA engineering with SVF can be a great candidate for regenerative medicine application. HyA3 can be a great candidate for increasing the regenerative potential of SVF, providing a microenvironment suitable for recreating the physiological stem niche.

5.4 Metabolic activity, DNA content, and migration evaluation of Stomal Vascular Fraction and Hyaluronic Acid 3

Several groups have developed strategies to enhance the therapeutic impact of transplanted cells, in this case, SVF, and the capability to migrate, localize, and be retained at the site of injury, to improve their therapeutic efficiency[171]. HyA is a

promising candidate due to its ability to promote cellular proliferation, migration, and intracellular signaling[155]. For example, MSC cultured with HyA enhanced chemotactic potential in glycerol-induced acute renal failure[172] and in a rat chronic renal failure model[173]. Hyaluronic acid effectively activated the CD44 receptor, essential for migrating MSCs to the wound site. Corradetti et al. demonstrated a two-fold increase in the migratory potential of HyA-treated MSC compared to untreated[174].

Following selecting the best hyaluronic acid-based scaffold to support SVF, additional *in vitro* tests were performed to assess the impact of HyA3 on metabolic activity, proliferative capacity, and cell migration within the SVF. Similarly to the studies reported above, HyA3 induced cellular migration. Specifically, findings reveal a significant increase in migration of SVF-expanded cells compared to the control at 24- and 36-hours post-contact. During the first 24 hours of contact, HyA3 may have stimulated the expression of molecules and ligands, such as CD44, on the cells surface, promoting their homing potential. This hypothesis was confirmed by Corradetti et al., demonstrating that the enhanced migratory capacity of MSCs in contact with HyA is correlated with an overexpression of CD44[175]. HyA is able to promote cellular migration in a damage tissue, thereby facilitating tissue regeneration.

In addition, HyA3 positively stimulated cellular metabolic activity. These findings could be consistent with those observed in Chapter 5.2, "Hyaluronic Acid *in vitro* Response." The significant increase in cellular metabolic activity corresponds with the biogenesis of lipid droplets induced following stimulation with HyA[176]. Concurrently, the absence of a significant increase in cellular proliferation following contact with HyA3 may be attributable to a prioritized allocation of cellular energy resources towards the neoformation of lipid droplet.

This result highlights the favourable ability of HyA3 to facilitate the homing of SVF cellular constituents and their paracrine factors within a site of injury.

5.5 *In vivo* pathological regenerative potential in a muscle ischemic reperfusion model

Peripheral artery disease (PAD) is a significant clinical problem because it causes 12 to 15% of deaths in Europe. The composition of blood flow causes skeletal muscle ischemia and reperfusion injury that occurs when blood flow is temporarily restricted and restored. The primary emergency is represented by critical and acute limb ischemia (ALI/CLI) characterized by intractable pain, ulcers, and gangrene, which require prompt treatment[177]. Indeed, up to a third of patients are not amenable to conventional intervention, such as angioplasty and surgical bypass, and also those who benefit from successful revascularization suffer from high rates of recurrent symptoms or revision surgery, and many require progressive amputation[178]. Given the morbidity, mortality, and costs, the need for optimal treatment to enhance limb preservation, prevent mortality, and improve functional capacity in these patients remains unmet[179]. Since current therapeutic options are still ineffective, new therapeutic strategies to improve patient outcomes are required.

In this context, after assessing the regenerative potential of human SVF combined with HyA3, a model of skeletal muscle ischemic reperfusion (I/R) injury was employed to evaluate its regenerative efficacy within a pathological context.

Peripheral application of a tourniquet was used to recreate the ischemic reperfusion injury in nude mice. At four day post injury (dpi), the T2-weighted (T2-w) MRI analysis revealed a hyperintense contrast in all I/R injured hindlimbs, indicating a higher presence of water in tissues due to edematous and inflammatory overflow following an ischemic lesion. By 7 dpi, animals treated with SVF combined with HyA displayed a T2-w contrast similar to that of CTRL, suggesting reduced edematous overflow and swelling. These observations were also confirmed by quantitative T2 relaxation time (T2-rt) analysis. At four dpi, muscle T2-rt increased significantly after the ischemic reperfusion injury compared to CTRL, suggesting that all experimental groups exhibited tissue damage. Starting for 7 dpi, animals treated with a combination of SVF and HyA exhibited muscle relaxation times (T2-rt) comparable to the CNTR groups (T2-rt close to 30 ms). Conversely, the SVF,

HyA, and saline groups consistently demonstrated a significant increase in T2-rt until 18 dpi. Notably, mice receiving saline sustained this significant increase even at 18 days. These results suggest that following tourniquet ligation, subsequent limb reperfusion led to a significant influx of blood through the venous circulation, as reflected by the T2-rt parameter. Indeed, a pronounced increase in T2-rt is commonly regarded as an MRI indication of muscle damage, reflecting substantial alterations in muscle architecture due to necrosis, edema, and inflammation[180, 181]. Disturbances in intracellular ion concentration and the accumulation of waste products likely induced significant homeostatic water shifts. Some authors, such as Zaccagnini et al., observed a positive correlation between T2-rt and ischemic damage[181]. They noted an immediate increase in muscle T2-rt following injury induction, which gradually declined, returning almost to basal levels in the later phases of the regenerative process (28 days).

In this study was observed that in remarkably brief timeframe (7 dpi), treatment with SVF in conjunction with HyA effectively restores muscle T2-rt to a physiological condition. The treatment has facilitated a significant reduction in the volume of fluid accumulation within the muscle tissue induced by the reperfusion phase. SVF and HyA treatments exhibited a more prolonged maintenance of high T2-rt, confirming that their separate action results in a slower reduction of edema accumulation. The results obtained through MRI analyses with T2-weighted and T2 multi-slice multi-echo (MSME) sequences were not confirmed by diffusion-weighted imaging analysis. The apparent diffusion coefficient (ADC) represents the diffusivity of water molecules in tissue and can be affected by factors such as the viscosity of extracellular water and cell membrane permeability. The parameter can be correlated to a condition of muscle edema or myonecrosis[182]. No significant differences were observed in the ADC values compared to the treatments. This could be caused by a lack of a pronounced modification in the muscle microarchitecture visible through such analysis.

Dynamic contrast-enhanced MRI (DCE-MRI) was used to examine vessel perfusion using an intravenous bolus injection of gadolinium contrast medium. The results showed that at four dpi, all treated I/R injured hindlimbs exhibited nearly twofold higher contrast agent signal over time than the CTRL. This result detected

damage to the microvascular structure (e.g., increased permeability) and function. The ischemic injury may have induced an elevation in pressure, resulting in permeability disbalance and rupture of blood vessels. From 18 dpi, no significant differences in the signal intensity were observed in the experimental group, probably due to a blood vessel regeneration. This result was in accordance with Zaccagnini et al., which showed a progressive restoration of the blood flow due to the regeneration of vessels and capillary networks[181]. Also, Tameshwar et al. described a significant increase in K trans in injury hindlimb from the control only during the acute phase (3dpi)[183]. The subsequent reduction in K trans is attributed to vessel healing and normalization of permeability.

The motor functional recovery was evaluated with a Rotarod test[184]. Over time, a progressive increase in motor performance was observed in animals treated with SVF combined with HyA from 4 dpi. The performance was similar in animals treated with SVF, while HyA-injected exhibited a decline in motor performance. The findings suggest that the heterogeneous SVF cellular mixture may have a fundamental role in the functional recovery of the ischemic hindlimb. It was impossible to compare with the literature as no published work considers this test with muscle I/R injury.

The analysis of muscle I/R injured cross-sections showed heterogeneity in fiber response to both ischemic and reperfusion injury, as well as treatments. In all examined groups, microscopic cross-sections consistently revealed the presence of histologically normal muscle fibers closely interspersed with fibers that exhibited different alterations. In general, it was observed that the superior gastrocnemius regions were less susceptible to I/R injury compared to the inferior regions, both in the LG and MG parts. This observation was also confirmed by the quantitative analysis of the average fiber area, in which animals treated with saline, SVF, and HyA showed a reduction in the average fiber area of the inferior region compared to the corresponding groups of the superior region. Conversely, the fiber area of the CNTR and SVF+HyA groups was similar in both inferior and superior muscle regions. This finding confirmed previous observations from other experimental I/R models, indicating that a possible explanation for the different patterns of fiber damage may depend on the type of gastrocnemius fibers. This muscle is

predominantly composed of MyHC2B type fibers, which are non-uniformly distributed and more abundantly in the superior regions than the inferior ones, where MyHC2X fibers are also present[185]. In the inferior regions adjacent to both soleus and plantar, all three isoforms of type II myosin (MyHC2A, 2B, 2X) are present in addition to type I myosin (MyHC1)[80]. Type I fiber is also known as slow myosin fiber, while type II as fast myosin fiber. In this study, the examined muscle cross-sections revealed heterogeneity of both MyoF and MyoS fibers, particularly in the inferior regions adjacent to both soleus and plantar, confirming previous findings.

Previous studies have demonstrated that:

- type II fibers are more involved in inflammatory damage than type I ones;
- muscles containing a similar quantity of fast-twitch fibers exhibit significantly increased necrosis compared to those predominantly composed of slow-twitch fibers[185];
- fast-twitch fibers demonstrate greater resistance to ischemic insults[186];
- fast-twitch fibers exhibit a greater degree of injury but are still functional following reperfusion.

These observations suggest that type II fibers have a greater involvement in I/R events compared to type I. It may depend on their higher metabolic rate which appears them intrinsically more susceptible to substrate loss through ischemia[185]. It has been observed that among fast-twitch fibers, the phenotype characterized by lower myosin content is particularly implicated in ischemia-reperfusion injury. The current study investigated the expression of specific markers to evaluate the regenerative aspects of the muscle after the injection of different treatments.

Desmin, an intermediate filament protein, is the major cytoskeletal protein present in adult skeletal muscle[187]. It plays a crucial role in the organization of the extra-sarcomeric cytoskeleton of muscle fibers by linking adjacent myofibers at the Z-discs and linking peripheral myofibers to the sarcolemma and the nuclear membrane[188]. The immunohistochemistry data revealed that desmin was present in small-diameter immature cells with centrally located nuclei with a disorganized expression pattern in saline or, SVF, or HyA-treated animals. However, in the

saline-treated animals, the disorganized desmin expression was localized in a larger area than that observed in SVF and HyA groups, distributed mainly in the inferior MG and LG regions. On the contrary, in the CTRL and SVF+HyA-treated animals, the desmin was expressed with a normal striated pattern inside the fibers. These results suggest that the abnormal and disorganized desmin expression may be correlated to the myofiber morphology. Similarly, Koutakis et al. demonstrate that myofibers from PAD patients showed desmin aggregates with an irregular honeycomb pattern and intense immunolabeling[189]. Furthermore, they reveal a clear correlation between the abnormal accumulation of desmin and the reduction in diameter, area, solidity, and density of myofibers. Similar evidence is reported in desminopathies, a subgroup of myofibrillar myopathies characterized by increased content of desmin in the myofibers, disorganization of the desmin filament network, accumulation of insoluble desmin containing aggregates and disruption of the sarcomere of striated muscle[190]. It is well known that the re-oxygenation of blood into ischemic tissue produces toxic ROS by mitochondrial enzymes, such as NADPH oxidase and xanthine oxidase[191]. The ROS production can directly damage desmin, leading to the inactivation and misfolding of the protein and exposing hydrophobic surfaces for protein-protein interaction, which promotes aggregation[192]. In this study it may be possible to suppose that the desmin disorganization is correlated with ROS production in saline, SVF, and HyA groups. While in the SVF+HyA group the re-establishment of the desmin organized expression may be due to the synergistic effect of the treatment that may facilitate the recovery of normal mitochondrial function, reducing ROS production.

It was observed that MyoF was distributed in a disorganized pattern in myofibers with small diameter and central nuclei, while those with normal polygonal shapes and lateral nuclei showed a normal expression pattern. Based on this different distribution, it can be assumed that MyoF expression is stickily related to fiber morphology and different degrees of differentiation. Furthermore, strong MyoF immunoreactivity was evident across the entire muscle surface of samples treated with saline, SVF, and HyA. These positive immunolabelling may represent tubular aggregates (TA) of tightly packed parallel arrays of single- or double-walled cylinders in the sarcoplasm[193] or amorphous materials. The formation of TA is

usually associated with a clinically heterogeneous group of disorders named tubular aggregate myopathies (TAM)[194, 195]. TA inclusion was usually found in type II muscle fibers, and many studies reported strong positives for severe markers, such as nicotinamide adenine dinucleotide tetrazolium reductase (NADH-TR) and myoadenylate deaminase (MAD)[196]. Schiaffino et al. reported the formation of TA aggregation in isolated rat muscle fibers kept in a hypoxic medium[197], suggesting that TA are sites of calcium accumulation. The increase of intracellular calcium is a consequence of alterations in the lysosomal membrane permeability, cytoskeleton configuration, and inhibition of the sodium-potassium pump[191]. Subsequently, calcium overload triggers the production of mitochondrial ROS production. The TA detection in saline, SVF, and HyA-treated animals can be hypothesized that the SVF+HyA treatment has a protective effect on aging all factors that trigger muscle injury.

There are now evidences that duration and intensity of inflammatory responses following the muscle injury and regeneration impact the outcome of muscle repair. An essential role in this regenerative process is attributed to satellite cells (SC) [198]. They are a pool of stem cells located beneath the basal lamina surrounding each fibre[199]. Quiescent SC expresses the transcription factor Pax7[200] and, when activated, co-express Pax7 with MyoD[201]. Most activated SC then proliferate, downregulate Pax7, and differentiate. By contrast, other proliferating cells maintain Pax7 but lose MyoD and return to a state resembling quiescence[202]. In this study, a greater Pax-7 immunoreactivity was observed in saline, SVF, and HyA-treated myofibers than in CTRL and SVF+HyA groups. Pax-7-positive cells were mainly detected in regenerative areas, in those adjacent to necrotic fibers, and around spaces resulting from phagocytosis of necrotic fibers. These later observations support the SC's use of pre-existing basement membranes of necrotic fibers to ensure a similar position to that of the newly formed myofibes[203]. Furthermore, Pax7-positive cells were observed adherent to the endothelium of vessels, indicating possible recruitment and transport of SC via the bloodstream to the regeneration site. In addition, in the present study it was found that numerous cells containing lipid droplets, labelled with Oil Red O (ORO) staining, had a distribution that was consistent with that of Pax7-positive cells. They were particularly

numerous in the regenerative areas. Quantitative analysis of area covered by ORO staining revealed that the percentage of ORO-covered area was significantly higher in saline treated animals compared to all other groups. Recently, Jue et al. exposed the possible role of LP in SC, demonstrating that committed SC accumulates abundant LD during cell division compared to self-renewal SC that exhibited a poor scant[144]. Based on this finding, it's possible consider that the ORO-positive cells presented in muscle cross-section regenerative areas are SC activate and committed to differentiation. Overall, in this study, the SVF+HyA treated group showed a lower Pax-7 and ORO positivity compared to the other treated groups, which correlated with the normal fiber morphology observed in this group and may demonstrate an earlier capacity to respond to muscle damage. On the other hand, in the SVF+HyA muscular sections, necrotic tissue was never noted, as observed in the groups treated with saline and SVF. It may depend on more immediate SC activation and proliferation and/or transient increase in collagen deposition, which is essential for a progressive recovery of normal tissue[203].

After ischemia-reperfusion injury, the initiation of inflammatory signals triggers the activation and recruitment of monocytes and neutrophils, responsible for the phagocytosis of debris and necrotic fibres[204]. Cytokines, such as CCL5, play a fundamental role by acting as pro-inflammatory recruiting factors. Indeed, in this study, it has been observed that the muscle cross-section of saline, SVF, and HyA-treated animals was characterized by a strong CCL5 expression, mainly observed near the necrotic fibers and within or adjacent areas of the endothelium of vessels. In addition, it was observed that a marked CCL5 expression was present in the same regions with Pax-7 positivity. This finding can explain that pro-inflammatory cytokines promote a promyogenic signaling cascade directing the migration, activation, proliferation, and differentiation of SC, which are necessary to regenerate muscle fibres[205, 206]. It may be a combination of amplifying the signals at the site of injury that recruit and activate proinflammatory immune cells and autocrine signals, promoting the rapid expansion of the SC before differentiation into muscle fibers. Alexander et al. detected CCL5-positive SC in cardiotoxin-injured muscle, suggesting that cytokine expression by these cells has a direct function in muscular repair[207]. In this regard, in this study it was observed that

SVF+HyA treated samples exhibited lower CCL5 and Pax7 expression compared to those treated with saline, SVF, HyA. This finding is probably related to a complete regenerative process observed in the myofibers with this treatment.

The results obtained suggest that the SVF, in combination with low molecular weight hyaluronic acid, promotes muscle regeneration following ischemia-reperfusion injury. Indeed, the synergistic treatment, compared to treatment with saline, SVF, and HyA, exhibits an early and enhanced capacity to respond to injury, accelerating the regenerative process.

As previously described in the preceding chapters, the cellular population of the SVF encapsulated within preserved micro-fragments of connective tissue may recreate the physiological stem niche. The synergistic interaction with an HyA may potentiate regeneration by reproducing the physiological cellular microenvironment, preserving SVF localization, and stimulating cellular and/or paracrine factors migration.

5.6 Characterization of human adipose tissue supernatant obtained by Stromal Vascular Fraction

In previous chapters, following confirmation of the potential regenerative capabilities of SVF encapsulated with HyA3, it was evaluated in a pathological model of skeletal muscle ischemia-reperfusion injury. The treatment demonstrated a beneficial effect in accelerating muscle tissue regeneration, rapidly reducing edema and inflammatory infiltration, and reinstating physiological motor functionality. Based on the reported data, it was hypothesized that the regenerative potential could primarily be attributed to the paracrine factors released by the heterogeneous cellular components of SVF.

To validate this hypothesis, an *in vitro* analysis of extracellular vesicles (EVs) secreted by the cellular component of SVF was performed.

The NTA analysis confirmed the presence of EVs in the supernatant phase of micro-fragmented SVF, with an average concentration of $2.34 \times 10^{11} \pm 3.69 \times 10^{11}$ particles/ml and an average size of 132.25 ± 15.38 nm. Transmission electron microscopy analysis revealed the presence of EVs within the cellular supernatants.

Additionally, EVs were detected in the SVF supernatant analysed via western blot, exhibiting positive immunolabeling for essential EV proteins, including tetraspanins, heat shock proteins, cell surface adhesion proteins, and components associated with the endosomal sorting complexes required for transport.

These results are in line with the guidelines used for the characterization of extracellular vesicles, confirming that SVF is capable of producing such factors [208].

Furthermore, ultrastructural analysis of the pellets reveals that some SVF cells exhibited multivesicular bodies (MBV) within the cytoplasm. Additionally, vesicles with a diameter of 50-70 nm were observed external to the cytoplasmic membrane, potentially indicative of recent release via MVB exocytosis. These observations are consistent with the pathway of exosome formation and release described in the literature[209, 210].

In scientific literature, it is extensively documented that the lipid membrane structure of EVs can contain paracrine mediators, including proteins, nucleic acids, and enzymes. These mediators have been shown to play a role in tissue regeneration by regulating cellular biological behaviours, such as angiogenesis, anti-apoptotic, immune modulation, proliferation, and migration [151, 211]. Some studies also report the effectiveness of EVs in regeneration following I/R. For example, Fagliolini et al. demonstrated that AD-MSC-EVs exert a protective effect on ischemic muscle damage by acting both on tissue microvessels and muscle cells[212]. Indeed, in the histological muscle sections, they showed in AD-MSC-EV treated animals an increase in capillary density and a reduction in the percentage of apoptotic cells and muscle damage. Transcriptomic analysis demonstrated that AD-MSC-EV treatment induced the expression of genes associated with myoblast proliferation.

These results, along with the comparison with literature studies, contribute to the increasing credibility of the hypothesized theory, attributing significant regenerative power to the secretome released by SVF in muscle ischemia-reperfusion injury.

6 CONCLUSION

In summary, the SVF obtained following mechanical fragmentation of adipose tissue was first *in vitro* characterized. This is comprised of connective tissue micro-fragments enclosing a heterogeneous pool of cells.

Subsequently, both *in vitro* and *in vivo* regenerative potential of SVF in contact with three hyaluronic acid, each with different chemical characteristics, was investigated. It was revealed that hyaluronic acid with low molecular weight and 2% auto-crosslinking (HyA3) conjugated with SVF stimulates adipose tissue formation from 7 days post-injection.

Finally, the regenerative potential of SVF conjugated with HyA3 was tested in a pathological model of muscle ischemia-reperfusion. It was demonstrated that treatment with SVF conjugated with HyA3 can repair the damage caused by ischemia-reperfusion in shorter timeframes compared to controls of SVF, HyA3, and saline.

These results demonstrate that the synergistic effect of SVF and HyA3 can be an effective treatment for muscle ischemia and reperfusion damage. It is hypothesized that the extracellular vesicles released by SVF, conjugated with the favourable microenvironment recreated by HyA3, stimulate muscle regeneration. Additional studies will be required to elucidate the molecular mechanisms of this hypothesis.

7 FUTURE PROSPECTIVE

Following this thesis project, it would be interesting to investigate which pathways are triggered by the synergistic action between SVF and HyA3. Identifying the pathways at the onset of the regenerative cascade could be useful for optimizing the regenerative treatment. Molecular biology techniques, transcriptomics, and proteomics could be useful for this purpose.

Furthermore, it would be interesting to verify the regenerative hypothesis of the extracellular vesicles released by the SVF cell pool. For this purpose, it would be necessary to test their efficacy using *in vitro* and *in vivo* ischemia and reperfusion

injury model. Additionally, it would be interesting to study the contents of the extracellular vesicles released by the SVF to a better understanding of their mechanism of action on recipient cells in view of a possible their therapeutic use.

8 REFERENCES

(1) Rojewski, M. T.; Weber, B. M.; Schrezenmeier, H. Phenotypic Characterization of Mesenchymal Stem Cells from Various Tissues. *Transfus Med Hemother* **2008**, *35* (3), 168-184. DOI: 10.1159/000129013 From NLM.
(2) Zuk, P. Adipose-derived stem cells in tissue regeneration: a review. *International Scholarly Research Notices* **2013**, *2013*.
(3) Strioga, M.; Viswanathan, S.; Darinskas, A.; Slaby, O.; Michalek, J. Same or not the same? Comparison of adipose tissue-derived versus bone marrow-derived mesenchymal stem and stromal cells. *Stem Cells Dev* **2012**, *21* (14), 2724-2752. DOI: 10.1089/scd.2011.0722 From NLM.
(4) Kuçi, S.; Kuçi, Z.; Latifi-Pupovci, H.; Niethammer, D.; Handgretinger, R.; Schumm, M.; Bruchelt, G.; Bader, P.; Klingebiel, T. Adult stem cells as an alternative source of multipotential (pluripotential) cells in regenerative medicine. *Curr Stem Cell Res Ther* **2009**, *4* (2), 107-117. DOI: 10.2174/157488809788167427 From NLM.
(5) Tsuji, W.; Rubin, J. P.; Marra, K. G. Adipose-derived stem cells: Implications in tissue regeneration. *World J Stem Cells* **2014**, *6* (3), 312-321. DOI: 10.4252/wjsc.v6.i3.312 From NLM.
(6) Busato, A.; De Francesco, F.; Biswas, R.; Mannucci, S.; Conti, G.; Fracasso, G.; Conti, A.; Riccio, V.; Riccio, M.; Sbarbati, A. Simple and Rapid Non-Enzymatic Procedure Allows the Isolation of Structurally Preserved Connective Tissue Micro-Fragments Enriched with SVF. *Cells* **2020**, *10* (1). DOI: 10.3390/cells10010036 From NLM.
(7) Jones, D. L.; Wagers, A. J. No place like home: anatomy and function of the stem cell niche. *Nat Rev Mol Cell Biol* **2008**, *9* (1), 11-21. DOI: 10.1038/nrm2319 From NLM.
(8) Condé-Green, A.; Kotamarti, V. S.; Sherman, L. S.; Keith, J. D.; Lee, E. S.; Granick, M. S.; Rameshwar, P. Shift toward Mechanical Isolation of Adipose-derived Stromal Vascular Fraction: Review of Upcoming Techniques. *Plast Reconstr Surg Glob Open* **2016**, *4* (9), e1017. DOI: 10.1097/gox.0000000000001017 From NLM.
(9) van Dongen, J. A.; Tuin, A. J.; Spiekman, M.; Jansma, J.; van der Lei, B.; Harmsen, M. C. Comparison of intraoperative procedures for isolation of clinical grade stromal vascular fraction for regenerative purposes: a systematic review. *J Tissue Eng Regen Med* **2018**, *12* (1), e261-e274. DOI: 10.1002/term.2407 From NLM.
(10) Oberbauer, E.; Steffenhagen, C.; Wurzer, C.; Gabriel, C.; Redl, H.; Wolbank, S. Enzymatic and non-enzymatic isolation systems for adipose tissue-derived cells: current state of the art. *Cell Regen* **2015**, *4*, 7. DOI: 10.1186/s13619-015-0020-0 From NLM.
(11) van Dongen, J. A.; Stevens, H. P.; Harmsen, M. C.; van der Lei, B. Mechanical Micronization of Lipoaspirates: Squeeze and Emulsification Techniques. *Plast Reconstr Surg* **2017**, *139* (6), 1369e-1370e. DOI: 10.1097/prs.0000000000003372 From NLM.
(12) van Dongen, J. A.; Stevens, H. P.; Parvizi, M.; van der Lei, B.; Harmsen, M. C. The fractionation of adipose tissue procedure to obtain stromal vascular fractions for regenerative purposes. *Wound Repair Regen* **2016**, *24* (6), 994-1003. DOI: 10.1111/wrr.12482 From NLM.
(13) Guo, J.; Nguyen, A.; Banyard, D. A.; Fadavi, D.; Toranto, J. D.; Wirth, G. A.; Paydar, K. Z.; Evans, G. R.; Widgerow, A. D. Stromal vascular fraction: A regenerative reality? Part 2:

Mechanisms of regenerative action. *J Plast Reconstr Aesthet Surg* **2016**, *69* (2), 180-188. DOI: 10.1016/j.bjps.2015.10.014 From NLM.
(14) Lu, H.; Wang, F.; Mei, H.; Wang, S.; Cheng, L. Human Adipose Mesenchymal Stem Cells Show More Efficient Angiogenesis Promotion on Endothelial Colony-Forming Cells than Umbilical Cord and Endometrium. *Stem Cells Int* **2018**, *2018*, 7537589. DOI: 10.1155/2018/7537589 From NLM.
(15) Freiman, A.; Shandalov, Y.; Rozenfeld, D.; Shor, E.; Segal, S.; Ben-David, D.; Meretzki, S.; Egozi, D.; Levenberg, S. Adipose-derived endothelial and mesenchymal stem cells enhance vascular network formation on three-dimensional constructs in vitro. *Stem Cell Res Ther* **2016**, *7*, 5. DOI: 10.1186/s13287-015-0251-6 From NLM.
(16) Rehman, J.; Traktuev, D.; Li, J.; Merfeld-Clauss, S.; Temm-Grove, C. J.; Bovenkerk, J. E.; Pell, C. L.; Johnstone, B. H.; Considine, R. V.; March, K. L. Secretion of angiogenic and antiapoptotic factors by human adipose stromal cells. *Circulation* **2004**, *109* (10), 1292-1298. DOI: 10.1161/01.Cir.0000121425.42966.F1 From NLM.
(17) Premaratne, G. U.; Ma, L. P.; Fujita, M.; Lin, X.; Bollano, E.; Fu, M. Stromal vascular fraction transplantation as an alternative therapy for ischemic heart failure: anti-inflammatory role. *J Cardiothorac Surg* **2011**, *6*, 43. DOI: 10.1186/1749-8090-6-43 From NLM.
(18) Tiemessen, M. M.; Jagger, A. L.; Evans, H. G.; van Herwijnen, M. J.; John, S.; Taams, L. S. CD4+CD25+Foxp3+ regulatory T cells induce alternative activation of human monocytes/macrophages. *Proc Natl Acad Sci U S A* **2007**, *104* (49), 19446-19451. DOI: 10.1073/pnas.0706832104 From NLM.
(19) Semon, J. A.; Zhang, X.; Pandey, A. C.; Alandete, S. M.; Maness, C.; Zhang, S.; Scruggs, B. A.; Strong, A. L.; Sharkey, S. A.; Beuttler, M. M.; et al. Administration of murine stromal vascular fraction ameliorates chronic experimental autoimmune encephalomyelitis. *Stem Cells Transl Med* **2013**, *2* (10), 789-796. DOI: 10.5966/sctm.2013-0032 From NLM.
(20) Badylak, S. F. The extracellular matrix as a scaffold for tissue reconstruction. *Semin Cell Dev Biol* **2002**, *13* (5), 377-383. DOI: 10.1016/s1084952102000940 From NLM.
(21) Sheetz, M. P.; Felsenfeld, D. P.; Galbraith, C. G. Cell migration: regulation of force on extracellular-matrix-integrin complexes. *Trends Cell Biol* **1998**, *8* (2), 51-54. DOI: 10.1016/s0962-8924(98)80005-6 From NLM.
(22) Bauer, A. L.; Jackson, T. L.; Jiang, Y. Topography of extracellular matrix mediates vascular morphogenesis and migration speeds in angiogenesis. *PLoS Comput Biol* **2009**, *5* (7), e1000445. DOI: 10.1371/journal.pcbi.1000445 From NLM.
(23) Blaber, S. P.; Webster, R. A.; Hill, C. J.; Breen, E. J.; Kuah, D.; Vesey, G.; Herbert, B. R. Analysis of in vitro secretion profiles from adipose-derived cell populations. *J Transl Med* **2012**, *10*, 172. DOI: 10.1186/1479-5876-10-172 From NLM.
(24) Xiong, M.; Zhang, Q.; Hu, W.; Zhao, C.; Lv, W.; Yi, Y.; Wu, Y.; Wu, M. Exosomes From Adipose-Derived Stem Cells: The Emerging Roles and Applications in Tissue Regeneration of Plastic and Cosmetic Surgery. *Front Cell Dev Biol* **2020**, *8*, 574223. DOI: 10.3389/fcell.2020.574223 From NLM.
(25) Wang, W. M.; Wu, C.; Jin, H. Z. Exosomes in chronic inflammatory skin diseases and skin tumors. *Exp Dermatol* **2019**, *28* (3), 213-218. DOI: 10.1111/exd.13857 From NLM.
(26) Cocucci, E.; Meldolesi, J. Ectosomes and exosomes: shedding the confusion between extracellular vesicles. *Trends Cell Biol* **2015**, *25* (6), 364-372. DOI: 10.1016/j.tcb.2015.01.004 From NLM.
(27) van Niel, G.; D'Angelo, G.; Raposo, G. Shedding light on the cell biology of extracellular vesicles. *Nat Rev Mol Cell Biol* **2018**, *19* (4), 213-228. DOI: 10.1038/nrm.2017.125 From NLM.

(28) Johnstone, R. M.; Adam, M.; Hammond, J. R.; Orr, L.; Turbide, C. Vesicle formation during reticulocyte maturation. Association of plasma membrane activities with released vesicles (exosomes). *J Biol Chem* **1987**, *262* (19), 9412-9420. From NLM.
(29) Pan, B. T.; Teng, K.; Wu, C.; Adam, M.; Johnstone, R. M. Electron microscopic evidence for externalization of the transferrin receptor in vesicular form in sheep reticulocytes. *J Cell Biol* **1985**, *101* (3), 942-948. DOI: 10.1083/jcb.101.3.942 From NLM.
(30) Tricarico, C.; Clancy, J.; D'Souza-Schorey, C. Biology and biogenesis of shed microvesicles. *Small GTPases* **2017**, *8* (4), 220-232. DOI: 10.1080/21541248.2016.1215283 From NLM.
(31) Battistelli, M.; Falcieri, E. Apoptotic Bodies: Particular Extracellular Vesicles Involved in Intercellular Communication. *Biology (Basel)* **2020**, *9* (1). DOI: 10.3390/biology9010021 From NLM.
(32) Valadi, H.; Ekström, K.; Bossios, A.; Sjöstrand, M.; Lee, J. J.; Lötvall, J. O. Exosome-mediated transfer of mRNAs and microRNAs is a novel mechanism of genetic exchange between cells. *Nat Cell Biol* **2007**, *9* (6), 654-659. DOI: 10.1038/ncb1596 From NLM.
(33) Choi, D. S.; Kim, D. K.; Kim, Y. K.; Gho, Y. S. Proteomics of extracellular vesicles: Exosomes and ectosomes. *Mass Spectrom Rev* **2015**, *34* (4), 474-490. DOI: 10.1002/mas.21420 From NLM.
(34) Georgescu, A.; Simionescu, M. Extracellular Vesicles: Versatile Nanomediators, Potential Biomarkers and Therapeutic Agents in Atherosclerosis and COVID-19-Related Thrombosis. *Int J Mol Sci* **2021**, *22* (11). DOI: 10.3390/ijms22115967 From NLM.
(35) Keshtkar, S.; Azarpira, N.; Ghahremani, M. H. Mesenchymal stem cell-derived extracellular vesicles: novel frontiers in regenerative medicine. *Stem Cell Res Ther* **2018**, *9* (1), 63. DOI: 10.1186/s13287-018-0791-7 From NLM.
(36) Meldolesi, J. Exosomes and Ectosomes in Intercellular Communication. *Curr Biol* **2018**, *28* (8), R435-r444. DOI: 10.1016/j.cub.2018.01.059 From NLM.
(37) Atkins, E. D.; Sheehan, J. K. Structure for hyaluronic acid. *Nat New Biol* **1972**, *235* (60), 253-254. DOI: 10.1038/newbio235253a0 From NLM.
(38) Vasi, A. M.; Popa, M. I.; Butnaru, M.; Dodi, G.; Verestiuc, L. Chemical functionalization of hyaluronic acid for drug delivery applications. *Mater Sci Eng C Mater Biol Appl* **2014**, *38*, 177-185. DOI: 10.1016/j.msec.2014.01.052 From NLM.
(39) Fraser, J. R.; Laurent, T. C.; Laurent, U. B. Hyaluronan: its nature, distribution, functions and turnover. *J Intern Med* **1997**, *242* (1), 27-33. DOI: 10.1046/j.1365-2796.1997.00170.x From NLM.
(40) Toole, B. P. Hyaluronan: from extracellular glue to pericellular cue. *Nat Rev Cancer* **2004**, *4* (7), 528-539. DOI: 10.1038/nrc1391 From NLM.
(41) Marinho, A.; Nunes, C.; Reis, S. Hyaluronic Acid: A Key Ingredient in the Therapy of Inflammation. *Biomolecules* **2021**, *11* (10). DOI: 10.3390/biom11101518 From NLM.
(42) Allison, D. D.; Grande-Allen, K. J. Review. Hyaluronan: a powerful tissue engineering tool. *Tissue Eng* **2006**, *12* (8), 2131-2140. DOI: 10.1089/ten.2006.12.2131 From NLM.
(43) Burdick, J. A.; Prestwich, G. D. Hyaluronic acid hydrogels for biomedical applications. *Adv Mater* **2011**, *23* (12), H41-56. DOI: 10.1002/adma.201003963 From NLM.
(44) Rayahin, J. E.; Buhrman, J. S.; Zhang, Y.; Koh, T. J.; Gemeinhart, R. A. High and low molecular weight hyaluronic acid differentially influence macrophage activation. *ACS Biomater Sci Eng* **2015**, *1* (7), 481-493. DOI: 10.1021/acsbiomaterials.5b00181 From NLM.
(45) Weigel, P. H.; Hascall, V. C.; Tammi, M. Hyaluronan synthases. *J Biol Chem* **1997**, *272* (22), 13997-14000. DOI: 10.1074/jbc.272.22.13997 From NLM.
(46) Itano, N.; Kimata, K. Mammalian hyaluronan synthases. *IUBMB Life* **2002**, *54* (4), 195-199. DOI: 10.1080/15216540214929 From NLM.

(47) Tavianatou, A. G.; Caon, I.; Franchi, M.; Piperigkou, Z.; Galesso, D.; Karamanos, N. K. Hyaluronan: molecular size-dependent signaling and biological functions in inflammation and cancer. *Febs j* **2019**, *286* (15), 2883-2908. DOI: 10.1111/febs.14777 From NLM.
(48) Stern, R.; Asari, A. A.; Sugahara, K. N. Hyaluronan fragments: an information-rich system. *Eur J Cell Biol* **2006**, *85* (8), 699-715. DOI: 10.1016/j.ejcb.2006.05.009 From NLM.
(49) Bastow, E. R.; Byers, S.; Golub, S. B.; Clarkin, C. E.; Pitsillides, A. A.; Fosang, A. J. Hyaluronan synthesis and degradation in cartilage and bone. *Cellular and Molecular Life Sciences* **2008**, *65* (3), 395-413. DOI: 10.1007/s00018-007-7360-z.
(50) Litwiniuk, M.; Krejner, A.; Speyrer, M. S.; Gauto, A. R.; Grzela, T. Hyaluronic Acid in Inflammation and Tissue Regeneration. *Wounds* **2016**, *28* (3), 78-88. From NLM.
(51) Gupta, R. C.; Lall, R.; Srivastava, A.; Sinha, A. Hyaluronic Acid: Molecular Mechanisms and Therapeutic Trajectory. *Front Vet Sci* **2019**, *6*, 192. DOI: 10.3389/fvets.2019.00192 From NLM.
(52) Marcotti, S.; Maki, K.; Reilly, G. C.; Lacroix, D.; Adachi, T. Hyaluronic acid selective anchoring to the cytoskeleton: An atomic force microscopy study. *PLoS One* **2018**, *13* (10), e0206056. DOI: 10.1371/journal.pone.0206056 From NLM.
(53) Fallacara, A.; Baldini, E.; Manfredini, S.; Vertuani, S. Hyaluronic Acid in the Third Millennium. *Polymers (Basel)* **2018**, *10* (7). DOI: 10.3390/polym10070701 From NLM.
(54) Sze, J. H.; Brownlie, J. C.; Love, C. A. Biotechnological production of hyaluronic acid: a mini review. *3 Biotech* **2016**, *6* (1), 67. DOI: 10.1007/s13205-016-0379-9 From NLM.
(55) Stern, R.; Maibach, H. I. Hyaluronan in skin: aspects of aging and its pharmacologic modulation. *Clin Dermatol* **2008**, *26* (2), 106-122. DOI: 10.1016/j.clindermatol.2007.09.013 From NLM.
(56) Passi, A.; Vigetti, D. Hyaluronan as tunable drug delivery system. *Adv Drug Deliv Rev* **2019**, *146*, 83-96. DOI: 10.1016/j.addr.2019.08.006 From NLM.
(57) Dicker, K. T.; Gurski, L. A.; Pradhan-Bhatt, S.; Witt, R. L.; Farach-Carson, M. C.; Jia, X. Hyaluronan: a simple polysaccharide with diverse biological functions. *Acta Biomater* **2014**, *10* (4), 1558-1570. DOI: 10.1016/j.actbio.2013.12.019 From NLM.
(58) Nikitovic, D.; Kouvidi, K.; Kavasi, R. M.; Berdiaki, A.; Tzanakakis, G. N. Hyaluronan/Hyaladherins - a Promising Axis for Targeted Drug Delivery in Cancer. *Curr Drug Deliv* **2016**, *13* (4), 500-511. DOI: 10.2174/1567201813666151109103013 From NLM.
(59) Weindl, G.; Schaller, M.; Schäfer-Korting, M.; Korting, H. C. Hyaluronic acid in the treatment and prevention of skin diseases: molecular biological, pharmaceutical and clinical aspects. *Skin Pharmacol Physiol* **2004**, *17* (5), 207-213. DOI: 10.1159/000080213 From NLM.
(60) Jiang, D.; Liang, J.; Noble, P. W. Hyaluronan in tissue injury and repair. *Annu Rev Cell Dev Biol* **2007**, *23*, 435-461. DOI: 10.1146/annurev.cellbio.23.090506.123337 From NLM.
(61) Nagy, N.; Kuipers, H. F.; Marshall, P. L.; Wang, E.; Kaber, G.; Bollyky, P. L. Hyaluronan in immune dysregulation and autoimmune diseases. *Matrix Biol* **2019**, *78-79*, 292-313. DOI: 10.1016/j.matbio.2018.03.022 From NLM.
(62) Ioannou, S.; Voulgarelis, M. Toll-like receptors, tissue injury, and tumourigenesis. *Mediators Inflamm* **2010**, *2010*. DOI: 10.1155/2010/581837 From NLM.
(63) Prestwich, G. D. Engineering a clinically-useful matrix for cell therapy. *Organogenesis* **2008**, *4* (1), 42-47. DOI: 10.4161/org.6152 From NLM.
(64) Knopf-Marques, H.; Pravda, M.; Wolfova, L.; Velebny, V.; Schaaf, P.; Vrana, N. E.; Lavalle, P. Hyaluronic Acid and Its Derivatives in Coating and Delivery Systems: Applications in Tissue Engineering, Regenerative Medicine and Immunomodulation. *Adv Healthc Mater* **2016**, *5* (22), 2841-2855. DOI: 10.1002/adhm.201600316 From NLM.

(65) Zerbinati, N.; Esposito, C.; Cipolla, G.; Calligaro, A.; Monticelli, D.; Martina, V.; Golubovic, M.; Binic, I.; Sigova, J.; Gallo, A. L.; et al. Chemical and mechanical characterization of hyaluronic acid hydrogel cross-linked with polyethylen glycol and its use in dermatology. *Dermatol Ther* **2020**, *33* (4), e13747. DOI: 10.1111/dth.13747 From NLM.
(66) Maleki, A.; Kjøniksen, A. L.; Nyström, B. Characterization of the chemical degradation of hyaluronic acid during chemical gelation in the presence of different cross-linker agents. *Carbohydr Res* **2007**, *342* (18), 2776-2792. DOI: 10.1016/j.carres.2007.08.021 From NLM.
(67) Vasvani, S.; Kulkarni, P.; Rawtani, D. Hyaluronic acid: A review on its biology, aspects of drug delivery, route of administrations and a special emphasis on its approved marketed products and recent clinical studies. *Int J Biol Macromol* **2020**, *151*, 1012-1029. DOI: 10.1016/j.ijbiomac.2019.11.066 From NLM.
(68) Aya, K. L.; Stern, R. Hyaluronan in wound healing: rediscovering a major player. *Wound Repair Regen* **2014**, *22* (5), 579-593. DOI: 10.1111/wrr.12214 From NLM.
(69) Huang, G.; Huang, H. Application of hyaluronic acid as carriers in drug delivery. *Drug Deliv* **2018**, *25* (1), 766-772. DOI: 10.1080/10717544.2018.1450910 From NLM.
(70) Kim, I. G.; Cho, H.; Shin, J.; Cho, J. H.; Cho, S. W.; Chung, E. J. Regeneration of irradiation-damaged esophagus by local delivery of mesenchymal stem-cell spheroids encapsulated in a hyaluronic-acid-based hydrogel. *Biomater Sci* **2021**, *9* (6), 2197-2208. DOI: 10.1039/d0bm01655a From NLM.
(71) Huynh, A.; Priefer, R. Hyaluronic acid applications in ophthalmology, rheumatology, and dermatology. *Carbohydr Res* **2020**, *489*, 107950. DOI: 10.1016/j.carres.2020.107950 From NLM.
(72) Fakhari, A.; Berkland, C. Applications and emerging trends of hyaluronic acid in tissue engineering, as a dermal filler and in osteoarthritis treatment. *Acta Biomater* **2013**, *9* (7), 7081-7092. DOI: 10.1016/j.actbio.2013.03.005 From NLM.
(73) Carnes, M. E.; Pins, G. D. Skeletal Muscle Tissue Engineering: Biomaterials-Based Strategies for the Treatment of Volumetric Muscle Loss. *Bioengineering (Basel)* **2020**, *7* (3). DOI: 10.3390/bioengineering7030085 From NLM.
(74) Exeter, D.; Connell, D. A. Skeletal muscle: functional anatomy and pathophysiology. In *Seminars in musculoskeletal radiology*, 2010; © Thieme Medical Publishers: Vol. 14, pp 097-105.
(75) Simoneau, J. A.; Bouchard, C. Human variation in skeletal muscle fiber-type proportion and enzyme activities. *Am J Physiol* **1989**, *257* (4 Pt 1), E567-572. DOI: 10.1152/ajpendo.1989.257.4.E567 From NLM.
(76) Zierath, J. R.; Hawley, J. A. Skeletal muscle fiber type: influence on contractile and metabolic properties. *PLoS Biol* **2004**, *2* (10), e348. DOI: 10.1371/journal.pbio.0020348 From NLM.
(77) Schuler, M.; Ali, F.; Chambon, C.; Duteil, D.; Bornert, J. M.; Tardivel, A.; Desvergne, B.; Wahli, W.; Chambon, P.; Metzger, D. PGC1alpha expression is controlled in skeletal muscles by PPARbeta, whose ablation results in fiber-type switching, obesity, and type 2 diabetes. *Cell Metab* **2006**, *4* (5), 407-414. DOI: 10.1016/j.cmet.2006.10.003 From NLM.
(78) Rayment, I. The structural basis of the myosin ATPase activity. *J Biol Chem* **1996**, *271* (27), 15850-15853. DOI: 10.1074/jbc.271.27.15850 From NLM.
(79) Pette, D.; Staron, R. S. Myosin isoforms, muscle fiber types, and transitions. *Microsc Res Tech* **2000**, *50* (6), 500-509. DOI: 10.1002/1097-0029(20000915)50:6<500::Aid-jemt7>3.0.Co;2-7 From NLM.
(80) Sawano, S.; Komiya, Y.; Ichitsubo, R.; Ohkawa, Y.; Nakamura, M.; Tatsumi, R.; Ikeuchi, Y.; Mizunoya, W. A one-step immunostaining method to visualize rodent muscle fiber type within a single specimen. *PLoS One* **2016**, *11* (11), e0166080.

(81) Collins, C. A.; Olsen, I.; Zammit, P. S.; Heslop, L.; Petrie, A.; Partridge, T. A.; Morgan, J. E. Stem cell function, self-renewal, and behavioral heterogeneity of cells from the adult muscle satellite cell niche. *Cell* **2005**, *122* (2), 289-301. DOI: 10.1016/j.cell.2005.05.010 From NLM.
(82) Jones, D. L.; Wagers, A. J. No place like home: anatomy and function of the stem cell niche. *Nature reviews Molecular cell biology* **2008**, *9* (1), 11-21.
(83) Mounier, R.; Chrétien, F.; Chazaud, B. Blood vessels and the satellite cell niche. *Current topics in developmental biology* **2011**, *96*, 121-138.
(84) Pannérec, A.; Marazzi, G.; Sassoon, D. Stem cells in the hood: the skeletal muscle niche. *Trends Mol Med* **2012**, *18* (10), 599-606. DOI: 10.1016/j.molmed.2012.07.004 From NLM.
(85) Yin, H.; Price, F.; Rudnicki, M. A. Satellite cells and the muscle stem cell niche. *Physiological reviews* **2013**, *93* (1), 23-67.
(86) McCullagh, K. J.; Perlingeiro, R. C. Coaxing stem cells for skeletal muscle repair. *Advanced drug delivery reviews* **2015**, *84*, 198-207.
(87) Le Grand, F.; Rudnicki, M. A. Skeletal muscle satellite cells and adult myogenesis. *Current opinion in cell biology* **2007**, *19* (6), 628-633.
(88) Rinaldi, F.; Perlingeiro, R. C. Stem cells for skeletal muscle regeneration: therapeutic potential and roadblocks. *Translational Research* **2014**, *163* (4), 409-417.
(89) Pollot, B. E.; Corona, B. T. Volumetric Muscle Loss. *Methods Mol Biol* **2016**, *1460*, 19-31. DOI: 10.1007/978-1-4939-3810-0_2 From NLM.
(90) Jani-Acsadi, A.; Ounpuu, S.; Pierz, K.; Acsadi, G. Pediatric Charcot-Marie-Tooth disease. *Pediatr Clin North Am* **2015**, *62* (3), 767-786. DOI: 10.1016/j.pcl.2015.03.012 From NLM.
(91) Pansarasa, O.; Rossi, D.; Berardinelli, A.; Cereda, C. Amyotrophic lateral sclerosis and skeletal muscle: an update. *Mol Neurobiol* **2014**, *49* (2), 984-990. DOI: 10.1007/s12035-013-8578-4 From NLM.
(92) Saure, C.; Caminiti, C.; Weglinski, J.; de Castro Perez, F.; Monges, S. Energy expenditure, body composition, and prevalence of metabolic disorders in patients with Duchenne muscular dystrophy. *Diabetes Metab Syndr* **2018**, *12* (2), 81-85. DOI: 10.1016/j.dsx.2017.08.006 From NLM.
(93) Gillani, S.; Cao, J.; Suzuki, T.; Hak, D. J. The effect of ischemia reperfusion injury on skeletal muscle. *Injury* **2012**, *43* (6), 670-675. DOI: 10.1016/j.injury.2011.03.008 From NLM.
(94) Tidball, J. G. Mechanisms of muscle injury, repair, and regeneration. *Compr Physiol* **2011**, *1* (4), 2029-2062. DOI: 10.1002/cphy.c100092 From NLM.
(95) Kalogeris, T.; Baines, C. P.; Krenz, M.; Korthuis, R. J. Cell biology of ischemia/reperfusion injury. *International review of cell and molecular biology* **2012**, *298*, 229-317.
(96) Bulkley, G. Free radical-mediated reperfusion injury: a selective review. *The British journal of cancer. Supplement* **1987**, *8*, 66.
(97) Yellon, D. M.; Hausenloy, D. J. Myocardial reperfusion injury. *New England Journal of Medicine* **2007**, *357* (11), 1121-1135.
(98) Baines, C. P. The mitochondrial permeability transition pore and ischemia-reperfusion injury. *Basic research in cardiology* **2009**, *104*, 181-188.
(99) Sanada, S.; Komuro, I.; Kitakaze, M. Pathophysiology of myocardial reperfusion injury: preconditioning, postconditioning, and translational aspects of protective measures. *American Journal of Physiology-Heart and Circulatory Physiology* **2011**, *301* (5), H1723-H1741.

(100) Szydlowska, K.; Tymianski, M. Calcium, ischemia and excitotoxicity. *Cell Calcium* **2010**, *47* (2), 122-129. DOI: 10.1016/j.ceca.2010.01.003 From NLM.
(101) Collard, C. D.; Gelman, S. Pathophysiology, clinical manifestations, and prevention of ischemia-reperfusion injury. *Anesthesiology* **2001**, *94* (6), 1133-1138. DOI: 10.1097/00000542-200106000-00030 From NLM.
(102) Ma, S.; Wang, Y.; Chen, Y.; Cao, F. The role of the autophagy in myocardial ischemia/reperfusion injury. *Biochim Biophys Acta* **2015**, *1852* (2), 271-276. DOI: 10.1016/j.bbadis.2014.05.010 From NLM.
(103) Toyokuni, S. Reactive oxygen species-induced molecular damage and its application in pathology. *Pathol Int* **1999**, *49* (2), 91-102. DOI: 10.1046/j.1440-1827.1999.00829.x From NLM.
(104) Halladin, N. L. Oxidative and inflammatory biomarkers of ischemia and reperfusion injuries. *Dan Med J* **2015**, *62* (4), B5054. From NLM.
(105) Rao, R. M.; Yang, L.; Garcia-Cardena, G.; Luscinskas, F. W. Endothelial-dependent mechanisms of leukocyte recruitment to the vascular wall. *Circ Res* **2007**, *101* (3), 234-247. DOI: 10.1161/CIRCRESAHA.107.151860b From NLM.
(106) Minamino, T.; Komuro, I.; Kitakaze, M. Endoplasmic reticulum stress as a therapeutic target in cardiovascular disease. *Circ Res* **2010**, *107* (9), 1071-1082. DOI: 10.1161/circresaha.110.227819 From NLM.
(107) Di Lisa, F.; Canton, M.; Menabò, R.; Kaludercic, N.; Bernardi, P. Mitochondria and cardioprotection. *Heart Fail Rev* **2007**, *12* (3-4), 249-260. DOI: 10.1007/s10741-007-9028-z From NLM.
(108) Di Paola, M.; Lorusso, M. Interaction of free fatty acids with mitochondria: coupling, uncoupling and permeability transition. *Biochim Biophys Acta* **2006**, *1757* (9-10), 1330-1337. DOI: 10.1016/j.bbabio.2006.03.024 From NLM.
(109) Ong, S. B.; Gustafsson, A. B. New roles for mitochondria in cell death in the reperfused myocardium. *Cardiovasc Res* **2012**, *94* (2), 190-196. DOI: 10.1093/cvr/cvr312 From NLM.
(110) Galluzzi, L.; Vitale, I.; Aaronson, S. A.; Abrams, J. M.; Adam, D.; Agostinis, P.; Alnemri, E. S.; Altucci, L.; Amelio, I.; Andrews, D. W.; et al. Molecular mechanisms of cell death: recommendations of the Nomenclature Committee on Cell Death 2018. *Cell Death Differ* **2018**, *25* (3), 486-541. DOI: 10.1038/s41418-017-0012-4 From NLM.
(111) He, C.; Klionsky, D. J. Regulation mechanisms and signaling pathways of autophagy. *Annu Rev Genet* **2009**, *43*, 67-93. DOI: 10.1146/annurev-genet-102808-114910 From NLM.
(112) Szabó, C. Mechanisms of cell necrosis. *Crit Care Med* **2005**, *33* (12 Suppl), S530-534. DOI: 10.1097/01.ccm.0000187002.88999.cf From NLM.
(113) Vandenabeele, P.; Declercq, W.; Van Herreweghe, F.; Vanden Berghe, T. The role of the kinases RIP1 and RIP3 in TNF-induced necrosis. *Sci Signal* **2010**, *3* (115), re4. DOI: 10.1126/scisignal.3115re4 From NLM.
(114) Kvietys, P. R.; Granger, D. N. Role of reactive oxygen and nitrogen species in the vascular responses to inflammation. *Free Radic Biol Med* **2012**, *52* (3), 556-592. DOI: 10.1016/j.freeradbiomed.2011.11.002 From NLM.
(115) Granger, D. N. Ischemia-reperfusion: mechanisms of microvascular dysfunction and the influence of risk factors for cardiovascular disease. *Microcirculation* **1999**, *6* (3), 167-178. From NLM.
(116) Olinic, D. M.; Spinu, M.; Olinic, M.; Homorodean, C.; Tataru, D. A.; Liew, A.; Schernthaner, G. H.; Stanek, A.; Fowkes, G.; Catalano, M. Epidemiology of peripheral artery disease in Europe: VAS Educational Paper. *Int Angiol* **2018**, *37* (4), 327-334. DOI: 10.23736/s0392-9590.18.03996-2 From NLM.

(117) Olinic, D. M.; Stanek, A.; Tătaru, D. A.; Homorodean, C.; Olinic, M. Acute Limb Ischemia: An Update on Diagnosis and Management. *J Clin Med* **2019**, *8* (8). DOI: 10.3390/jcm8081215 From NLM.
(118) Creager, M. A.; Kaufman, J. A.; Conte, M. S. Clinical practice. Acute limb ischemia. *N Engl J Med* **2012**, *366* (23), 2198-2206. DOI: 10.1056/NEJMcp1006054 From NLM.
(119) Eliason, J. L.; Wainess, R. M.; Proctor, M. C.; Dimick, J. B.; Cowan, J. A., Jr.; Upchurch, G. R., Jr.; Stanley, J. C.; Henke, P. K. A national and single institutional experience in the contemporary treatment of acute lower extremity ischemia. *Ann Surg* **2003**, *238* (3), 382-389; discussion 389-390. DOI: 10.1097/01.sla.0000086663.49670.d1 From NLM.
(120) Norgren, L.; Hiatt, W. R.; Dormandy, J. A.; Nehler, M. R.; Harris, K. A.; Fowkes, F. G. Inter-Society Consensus for the Management of Peripheral Arterial Disease (TASC II). *J Vasc Surg* **2007**, *45 Suppl S*, S5-67. DOI: 10.1016/j.jvs.2006.12.037 From NLM.
(121) Conte, M. S.; Bradbury, A. W.; Kolh, P.; White, J. V.; Dick, F.; Fitridge, R.; Mills, J. L.; Ricco, J. B.; Suresh, K. R.; Murad, M. H. Global vascular guidelines on the management of chronic limb-threatening ischemia. *J Vasc Surg* **2019**, *69* (6s), 3S-125S.e140. DOI: 10.1016/j.jvs.2019.02.016 From NLM.
(122) Natarajan, B.; Patel, P.; Mukherjee, A. Acute Lower Limb Ischemia-Etiology, Pathology, and Management. *Int J Angiol* **2020**, *29* (3), 168-174. DOI: 10.1055/s-0040-1713769 From NLM.
(123) Criqui, M. H.; Aboyans, V. Epidemiology of peripheral artery disease. *Circ Res* **2015**, *116* (9), 1509-1526. DOI: 10.1161/circresaha.116.303849 From NLM.
(124) Ferdinandy, P.; Schulz, R.; Baxter, G. F. Interaction of cardiovascular risk factors with myocardial ischemia/reperfusion injury, preconditioning, and postconditioning. *Pharmacol Rev* **2007**, *59* (4), 418-458. DOI: 10.1124/pr.107.06002 From NLM.
(125) Pugh, D.; Karabayas, M.; Basu, N.; Cid, M. C.; Goel, R.; Goodyear, C. S.; Grayson, P. C.; McAdoo, S. P.; Mason, J. C.; Owen, C.; et al. Large-vessel vasculitis. *Nat Rev Dis Primers* **2022**, *7* (1), 93. DOI: 10.1038/s41572-021-00327-5 From NLM.
(126) Linkins, L. A.; Dans, A. L.; Moores, L. K.; Bona, R.; Davidson, B. L.; Schulman, S.; Crowther, M. Treatment and prevention of heparin-induced thrombocytopenia: Antithrombotic Therapy and Prevention of Thrombosis, 9th ed: American College of Chest Physicians Evidence-Based Clinical Practice Guidelines. *Chest* **2012**, *141* (2 Suppl), e495S-e530S. DOI: 10.1378/chest.11-2303 From NLM.
(127) Callum, K.; Bradbury, A. ABC of arterial and venous disease: Acute limb ischaemia. *Bmj* **2000**, *320* (7237), 764-767. DOI: 10.1136/bmj.320.7237.764 From NLM.
(128) Dormandy, J.; Heeck, L.; Vig, S. Acute limb ischemia. *Semin Vasc Surg* **1999**, *12* (2), 148-153. From NLM.
(129) Hirsch, A. T.; Haskal, Z. J.; Hertzer, N. R.; Bakal, C. W.; Creager, M. A.; Halperin, J. L.; Hiratzka, L. F.; Murphy, W. R.; Olin, J. W.; Puschett, J. B.; et al. ACC/AHA 2005 Practice Guidelines for the management of patients with peripheral arterial disease (lower extremity, renal, mesenteric, and abdominal aortic): a collaborative report from the American Association for Vascular Surgery/Society for Vascular Surgery, Society for Cardiovascular Angiography and Interventions, Society for Vascular Medicine and Biology, Society of Interventional Radiology, and the ACC/AHA Task Force on Practice Guidelines (Writing Committee to Develop Guidelines for the Management of Patients With Peripheral Arterial Disease): endorsed by the American Association of Cardiovascular and Pulmonary Rehabilitation; National Heart, Lung, and Blood Institute; Society for Vascular Nursing; TransAtlantic Inter-Society Consensus; and Vascular Disease Foundation. *Circulation* **2006**, *113* (11), e463-654. DOI: 10.1161/circulationaha.106.174526 From NLM.

(130) Rutherford, R. B.; Baker, J. D.; Ernst, C.; Johnston, K. W.; Porter, J. M.; Ahn, S.; Jones, D. N. Recommended standards for reports dealing with lower extremity ischemia: revised version. *J Vasc Surg* **1997**, *26* (3), 517-538. DOI: 10.1016/s0741-5214(97)70045-4 From NLM.
(131) Blaisdell, F. W.; Steele, M.; Allen, R. E. Management of acute lower extremity arterial ischemia due to embolism and thrombosis. *Surgery* **1978**, *84* (6), 822-834. From NLM.
(132) Bandyk, D. F.; Chauvapun, J. P. Duplex ultrasound surveillance can be worthwhile after arterial intervention. *Perspect Vasc Surg Endovasc Ther* **2007**, *19* (4), 354-359; discussion 360-351. DOI: 10.1177/1531003507311681 From NLM.
(133) Menke, J.; Larsen, J. Meta-analysis: Accuracy of contrast-enhanced magnetic resonance angiography for assessing steno-occlusions in peripheral arterial disease. *Ann Intern Med* **2010**, *153* (5), 325-334. DOI: 10.7326/0003-4819-153-5-201009070-00007 From NLM.
(134) Kaufman, J. A.; Barnes, G. D.; Chaer, R. A.; Cuschieri, J.; Eberhardt, R. T.; Johnson, M. S.; Kuo, W. T.; Murin, S.; Patel, S.; Rajasekhar, A.; et al. Society of Interventional Radiology Clinical Practice Guideline for Inferior Vena Cava Filters in the Treatment of Patients with Venous Thromboembolic Disease: Developed in collaboration with the American College of Cardiology, American College of Chest Physicians, American College of Surgeons Committee on Trauma, American Heart Association, Society for Vascular Surgery, and Society for Vascular Medicine. *J Vasc Interv Radiol* **2020**, *31* (10), 1529-1544. DOI: 10.1016/j.jvir.2020.06.014 From NLM.
(135) Fluck, F.; Augustin, A. M.; Bley, T.; Kickuth, R. Current Treatment Options in Acute Limb Ischemia. *Rofo* **2020**, *192* (4), 319-326. DOI: 10.1055/a-0998-4204 From NLM.
(136) Karnabatidis, D.; Spiliopoulos, S.; Tsetis, D.; Siablis, D. Quality improvement guidelines for percutaneous catheter-directed intra-arterial thrombolysis and mechanical thrombectomy for acute lower-limb ischemia. *Cardiovasc Intervent Radiol* **2011**, *34* (6), 1123-1136. DOI: 10.1007/s00270-011-0258-z From NLM.
(137) Carden, D. L.; Granger, D. N. Pathophysiology of ischaemia-reperfusion injury. *J Pathol* **2000**, *190* (3), 255-266. DOI: 10.1002/(sici)1096-9896(200002)190:3<255::Aid-path526>3.0.Co;2-6 From NLM.
(138) Aboyans, V.; Ricco, J. B.; Bartelink, M. E. L.; Björck, M.; Brodmann, M.; Cohnert, T.; Collet, J. P.; Czerny, M.; De Carlo, M.; Debus, S.; et al. 2017 ESC Guidelines on the Diagnosis and Treatment of Peripheral Arterial Diseases, in collaboration with the European Society for Vascular Surgery (ESVS): Document covering atherosclerotic disease of extracranial carotid and vertebral, mesenteric, renal, upper and lower extremity arteriesEndorsed by: the European Stroke Organization (ESO)The Task Force for the Diagnosis and Treatment of Peripheral Arterial Diseases of the European Society of Cardiology (ESC) and of the European Society for Vascular Surgery (ESVS). *Eur Heart J* **2018**, *39* (9), 763-816. DOI: 10.1093/eurheartj/ehx095 From NLM.
(139) Dai Prè, E.; Busato, A.; Mannucci, S.; Vurro, F.; De Francesco, F.; Riccio, V.; Solito, S.; Biswas, R.; Bernardi, P.; Riccio, M. In vitro characterization of adipose stem cells non-enzymatically extracted from the thigh and abdomen. *International Journal of Molecular Sciences* **2020**, *21* (9), 3081.
(140) Finelli, I.; Chiessi, E.; Galesso, D.; Renier, D.; Paradossi, G. A new viscosupplement based on partially hydrophobic hyaluronic acid: a comparative study. *Biorheology* **2011**, *48* (5-6), 263-275.
(141) Guidolin, D.; Franceschi, F. Viscosupplementation with high molecular weight native hyaluronan. Focus on a 1500-2000 KDa fraction (Hyalubrix®). *Eur Rev Med Pharmacol Sci* **2014**, *18* (21), 3326-3338.

(142) Mensitieri, M.; Ambrosio, L.; Nicolais, L.; Bellini, D.; O'Regan, M. Viscoelastic properties modulation of a novel autocrosslinked hyaluronic acid polymer. *Journal of Materials Science: Materials in Medicine* **1996**, *7*, 695-698.
(143) La Gatta, A.; Stellavato, A.; Vassallo, V.; Di Meo, C.; Toro, G.; Iolascon, G.; Schiraldi, C. Hyaluronan and derivatives: An in vitro multilevel assessment of their potential in viscosupplementation. *Polymers* **2021**, *13* (19), 3208.
(144) Yue, F.; Oprescu, S. N.; Qiu, J.; Gu, L.; Zhang, L.; Chen, J.; Narayanan, N.; Deng, M.; Kuang, S. Lipid droplet dynamics regulate adult muscle stem cell fate. *Cell reports* **2022**, *38* (3).
(145) Yano, K.; Watanabe, N.; Tsuyuki, K.; Ikawa, T.; Kasanuki, H.; Yamato, M. Regulatory approval for autologous human cells and tissue products in the United States, the European Union, and Japan. *Regenerative Therapy* **2015**, *1*, 45-56.
(146) Hendijani, F. Explant culture: An advantageous method for isolation of mesenchymal stem cells from human tissues. *Cell proliferation* **2017**, *50* (2), e12334.
(147) Chang, H.; Do, B.-R.; Che, J.-H.; Kang, B.-C.; Kim, J.-H.; Kwon, E.; Kim, J.-Y.; Min, K.-H. Safety of adipose-derived stem cells and collagenase in fat tissue preparation. *Aesthetic plastic surgery* **2013**, *37*, 802-808.
(148) Markarian, C. F.; Frey, G. Z.; Silveira, M. D.; Milani, A. R.; Ely, P. B.; Horn, A. P.; Nardi, N. B.; Camassola, M. Isolation of adipose-derived stem cells: a comparison among different methods. *Biotechnology letters* **2014**, *36*, 693-702.
(149) Astori, G.; Vignati, F.; Bardelli, S.; Tubio, M.; Gola, M.; Albertini, V.; Bambi, F.; Scali, G.; Castelli, D.; Rasini, V. " In vitro" and multicolor phenotypic characterization of cell subpopulations identified in fresh human adipose tissue stromal vascular fraction and in the derived mesenchymal stem cells. *Journal of Translational Medicine* **2007**, *5*, 1-10.
(150) Khazaei, S.; Keshavarz, G.; Bozorgi, A.; Nazari, H.; Khazaei, M. Adipose tissue-derived stem cells: A comparative review on isolation, culture, and differentiation methods. *Cell and tissue banking* **2022**, *23* (1), 1-16.
(151) Guo, J.; Nguyen, A.; Banyard, D. A.; Fadavi, D.; Toranto, J. D.; Wirth, G. A.; Paydar, K. Z.; Evans, G. R.; Widgerow, A. D. Stromal vascular fraction: A regenerative reality? Part 2: Mechanisms of regenerative action. *Journal of Plastic, Reconstructive & Aesthetic Surgery* **2016**, *69* (2), 180-188.
(152) Traktuev, D. O.; Prater, D. N.; Merfeld-Clauss, S.; Sanjeevaiah, A. R.; Saadatzadeh, M. R.; Murphy, M.; Johnstone, B. H.; Ingram, D. A.; March, K. L. Robust functional vascular network formation in vivo by cooperation of adipose progenitor and endothelial cells. *Circulation research* **2009**, *104* (12), 1410-1420.
(153) Zeyda, M.; Farmer, D.; Todoric, J.; Aszmann, O.; Speiser, M.; Györi, G.; Zlabinger, G.; Stulnig, T. Human adipose tissue macrophages are of an anti-inflammatory phenotype but capable of excessive pro-inflammatory mediator production. *International journal of obesity* **2007**, *31* (9), 1420-1428.
(154) Usuelli, F. G.; Grassi, M.; Maccario, C.; Vigano', M.; Lanfranchi, L.; Alfieri Montrasio, U.; de Girolamo, L. Intratendinous adipose-derived stromal vascular fraction (SVF) injection provides a safe, efficacious treatment for Achilles tendinopathy: results of a randomized controlled clinical trial at a 6-month follow-up. *Knee Surgery, Sports Traumatology, Arthroscopy* **2018**, *26*, 2000-2010.
(155) Fallacara, A.; Baldini, E.; Manfredini, S.; Vertuani, S. Hyaluronic acid in the third millennium. *Polymers* **2018**, *10* (7), 701.
(156) Knudson, C. B. Hyaluronan and CD44: strategic players for cell–matrix interactions during chondrogenesis and matrix assembly. *Birth Defects Research Part C: Embryo Today: Reviews* **2003**, *69* (2), 174-196.

(157) Tang, Q. Q.; Lane, M. D. Adipogenesis: from stem cell to adipocyte. *Annual review of biochemistry* **2012**, *81*, 715-736.
(158) Snetkov, P.; Zakharova, K.; Morozkina, S.; Olekhnovich, R.; Uspenskaya, M. Hyaluronic acid: The influence of molecular weight on structural, physical, physico-chemical, and degradable properties of biopolymer. *Polymers* **2020**, *12* (8), 1800.
(159) Olzmann, J. A.; Carvalho, P. Dynamics and functions of lipid droplets. *Nature reviews Molecular cell biology* **2019**, *20* (3), 137-155.
(160) Boschi, F.; Rizzatti, V.; Zamboni, M.; Sbarbati, A. Models of lipid droplets growth and fission in adipocyte cells. *Experimental Cell Research* **2015**, *336* (2), 253-262.
(161) Nadra, K.; André, M.; Marchaud, E.; Kestemont, P.; Braccini, F.; Cartier, H.; Kéophiphath, M.; Fanian, F. A hyaluronic acid-based filler reduces lipolysis in human mature adipocytes and maintains adherence and lipid accumulation of long-term differentiated human preadipocytes. *Journal of Cosmetic Dermatology* **2021**, *20* (5), 1474-1482.
(162) Alessio, N.; Stellavato, A.; Squillaro, T.; Del Gaudio, S.; Di Bernardo, G.; Peluso, G.; De Rosa, M.; Schiraldi, C.; Galderisi, U. Hybrid complexes of high and low molecular weight hyaluronan delay in vitro replicative senescence of mesenchymal stromal cells: a pilot study for future therapeutic application. *Aging (Albany NY)* **2018**, *10* (7), 1575.
(163) Stellavato, A.; La Noce, M.; Corsuto, L.; Pirozzi, A. V. A.; De Rosa, M.; Papaccio, G.; Schiraldi, C.; Tirino, V. Hybrid complexes of high and low molecular weight hyaluronans highly enhance HASCs differentiation: implication for facial bioremodelling. *Cellular physiology and biochemistry* **2017**, *44* (3), 1078-1092.
(164) Kirkland, J. L.; Hollenberg, C. H.; Gillon, W. S. Age, anatomic site, and the replication and differentiation of adipocyte precursors. *American Journal of Physiology-Cell Physiology* **1990**, *258* (2), C206-C210.
(165) Labusca, L.; Zugun-Eloae, F. The unexplored role of intra-articular adipose tissue in the homeostasis and pathology of articular joints. *Frontiers in veterinary science* **2018**, *5*, 35.
(166) Andia, I.; Maffulli, N.; Burgos-Alonso, N. Stromal vascular fraction technologies and clinical applications. *Expert opinion on biological therapy* **2019**, *19* (12), 1289-1305.
(167) Huang, S.-H.; Lin, Y.-N.; Lee, S.-S.; Chai, C.-Y.; Chang, H.-W.; Lin, T.-M.; Lai, C.-S.; Lin, S.-D. New adipose tissue formation by human adipose-derived stem cells with hyaluronic acid gel in immunodeficient mice. *International journal of medical sciences* **2015**, *12* (2), 154.
(168) Hemmrich, K.; Van de Sijpe, K.; Rhodes, N. P.; Hunt, J. A.; Di Bartolo, C.; Pallua, N.; Blondeel, P.; Von Heimburg, D. Autologous in vivo adipose tissue engineering in hyaluronan-based gels—a pilot study. *Journal of Surgical Research* **2008**, *144* (1), 82-88.
(169) Şahin, A. A.; Değirmenci, E.; Özturan, K. E.; Fırat, T.; Kükner, A. Effects of adipose tissue-derived stromal vascular fraction on osteochondral defects treated by hyaluronic acid-based scaffold: An experimental study. *Joint diseases and related surgery* **2021**, *32* (2), 347.
(170) Chen, B.; Cai, J.; Wei, Y.; Jiang, Z.; Desjardins, H. E.; Adams, A. E.; Li, S.; Kao, H.-K.; Guo, L. Exosomes are comparable to source adipose stem cells in fat graft retention with up-regulating early inflammation and angiogenesis. *Plastic and reconstructive surgery* **2019**, *144* (5), 816e-827e.
(171) da Silva Meirelles, L.; Fontes, A. M.; Covas, D. T.; Caplan, A. I. Mechanisms involved in the therapeutic properties of mesenchymal stem cells. *Cytokine & growth factor reviews* **2009**, *20* (5-6), 419-427.
(172) Herrera, M.; Bussolati, B.; Bruno, S.; Morando, L.; Mauriello-Romanazzi, G.; Sanavio, F.; Stamenkovic, I.; Biancone, L.; Camussi, G. Exogenous mesenchymal stem cells localize

to the kidney by means of CD44 following acute tubular injury. *Kidney international* **2007**, *72* (4), 430-441.
(173) Bian, X.-H.; Zhou, G.-Y.; Wang, L.-N.; Ma, J.-F.; Fan, Q.-L.; Liu, N.; Bai, Y.; Guo, W.; Wang, Y.-Q.; Sun, G.-P. The role of CD44-hyaluronic acid interaction in exogenous mesenchymal stem cells homing to rat remnant kidney. *Kidney and Blood Pressure Research* **2014**, *38* (1), 11-20.
(174) Corradetti, B.; Taraballi, F.; Martinez, J. O.; Minardi, S.; Basu, N.; Bauza, G.; Evangelopoulos, M.; Powell, S.; Corbo, C.; Tasciotti, E. Hyaluronic acid coatings as a simple and efficient approach to improve MSC homing toward the site of inflammation. *Scientific reports* **2017**, *7* (1), 7991.
(175) Corradetti, B.; Taraballi, F.; Martinez, J. O.; Minardi, S.; Basu, N.; Bauza, G.; Evangelopoulos, M.; Powell, S.; Corbo, C.; Tasciotti, E. Hyaluronic acid coatings as a simple and efficient approach to improve MSC homing toward the site of inflammation. *Sci Rep* **2017**, *7* (1), 7991. DOI: 10.1038/s41598-017-08687-3 From NLM.
(176) Olzmann, J. A.; Carvalho, P. Dynamics and functions of lipid droplets. *Nat Rev Mol Cell Biol* **2019**, *20* (3), 137-155. DOI: 10.1038/s41580-018-0085-z From NLM.
(177) Fowkes, F. G. R.; Aboyans, V.; Fowkes, F. J.; McDermott, M. M.; Sampson, U. K.; Criqui, M. H. Peripheral artery disease: epidemiology and global perspectives. *Nature Reviews Cardiology* **2017**, *14* (3), 156-170.
(178) Behroozian, A.; Beckman, J. A. Microvascular disease increases amputation in patients with peripheral artery disease. *Arteriosclerosis, thrombosis, and vascular biology* **2020**, *40* (3), 534-540.
(179) Olin, J. W.; Sealove, B. A. Peripheral artery disease: current insight into the disease and its diagnosis and management. In *Mayo Clinic Proceedings*, 2010; Elsevier: Vol. 85, pp 678-692.
(180) Esposito, A.; Campana, L.; Palmisano, A.; De Cobelli, F.; Canu, T.; Santarella, F.; Colantoni, C.; Monno, A.; Vezzoli, M.; Pezzetti, G. Magnetic resonance imaging at 7T reveals common events in age-related sarcopenia and in the homeostatic response to muscle sterile injury. *PloS one* **2013**, *8* (3), e59308.
(181) Zaccagnini, G.; Palmisano, A.; Canu, T.; Maimone, B.; Lo Russo, F. M.; Ambrogi, F.; Gaetano, C.; De Cobelli, F.; Del Maschio, A.; Esposito, A. Magnetic resonance imaging allows the evaluation of tissue damage and regeneration in a mouse model of critical limb ischemia. *PloS one* **2015**, *10* (11), e0142111.
(182) Zaraiskaya, T.; Kumbhare, D.; Noseworthy, M. D. Diffusion tensor imaging in evaluation of human skeletal muscle injury. *Journal of Magnetic Resonance Imaging: An Official Journal of the International Society for Magnetic Resonance in Medicine* **2006**, *24* (2), 402-408.
(183) Ganesh, T.; Zakher, E.; Estrada, M.; Cheng, H. L. M. Assessment of microvascular dysfunction in acute limb ischemia-reperfusion injury. *Journal of magnetic resonance imaging* **2019**, *49* (4), 1174-1185.
(184) Deacon, R. M. Measuring motor coordination in mice. *JoVE (Journal of Visualized Experiments)* **2013**, (75), e2609.
(185) Chan, R. K.; Austen Jr, W. G.; Ibrahim, S.; Ding, G. Y.; Verna, N.; Hechtman, H. B.; Moore Jr, F. D. Reperfusion injury to skeletal muscle affects primarily type II muscle fibers1. *Journal of Surgical Research* **2004**, *122* (1), 54-60.
(186) Gürke, L.; Marx, A.; Sutter, P.-M.; Stierli, P.; Harder, F.; Heberer, M. Function of fast- and slow-twitch rat skeletal muscle following ischemia and reperfusion at different intramuscular temperatures. *European surgical research* **2000**, *32* (3), 135-141.
(187) Szeverenyi, I.; Cassidy, A. J.; Chung, C. W.; Lee, B. T.; Common, J. E.; Ogg, S. C.; Chen, H.; Sim, S. Y.; Goh, W. L.; Ng, K. W. The Human Intermediate Filament Database:

comprehensive information on a gene family involved in many human diseases. *Human mutation* **2008**, *29* (3), 351-360.
(188) Fuchs, E.; Weber, K. Intermediate filaments: structure, dynamics, function and disease. *Annual review of biochemistry* **1994**, *63* (1), 345-382.
(189) Koutakis, P.; Miserlis, D.; Myers, S. A.; Kim, J. K.-S.; Zhu, Z.; Papoutsi, E.; Swanson, S. A.; Haynatzki, G.; Ha, D. M.; Carpenter, L. A. Abnormal accumulation of desmin in gastrocnemius myofibers of patients with peripheral artery disease: associations with altered myofiber morphology and density, mitochondrial dysfunction and impaired limb function. *Journal of Histochemistry & Cytochemistry* **2015**, *63* (4), 256-269.
(190) Goldfarb, L.; Vicart, P.; Goebel, H.; Dalakas, M. Desmin myopathy. *Brain* **2004**, *127* (4), 723-734.
(191) Zhang, W.; Wang, W.; Yu, D. X.; Xiao, Z.; He, Z. Application of nanodiagnostics and nanotherapy to CNS diseases. *Nanomedicine* **2018**, *13* (18), 2341-2371.
(192) Janué, A.; Odena, M. A.; Oliveira, E.; Olivé, M.; Ferrer, I. Desmin is oxidized and nitrated in affected muscles in myotilinopathies and desminopathies. *J Neuropathol Exp Neurol* **2007**, *66* (8), 711-723. DOI: 10.1097/nen.0b013e3181256b4c From NLM.
(193) Engel, W. K.; Bishop, D. W.; Cunningham, G. G. Tubular aggregates in type II muscle fibers: ultrastructural and histochemical correlation. *J Ultrastruct Res* **1970**, *31* (5-6), 507-525. DOI: 10.1016/s0022-5320(70)90166-8 From NLM.
(194) Guergueltcheva, V.; Müller, J. S.; Dusl, M.; Senderek, J.; Oldfors, A.; Lindbergh, C.; Maxwell, S.; Colomer, J.; Mallebrera, C. J.; Nascimento, A.; et al. Congenital myasthenic syndrome with tubular aggregates caused by GFPT1 mutations. *J Neurol* **2012**, *259* (5), 838-850. DOI: 10.1007/s00415-011-6262-z From NLM.
(195) Finlayson, S.; Palace, J.; Belaya, K.; Walls, T. J.; Norwood, F.; Burke, G.; Holton, J. L.; Pascual-Pascual, S. I.; Cossins, J.; Beeson, D. Clinical features of congenital myasthenic syndrome due to mutations in DPAGT1. *J Neurol Neurosurg Psychiatry* **2013**, *84* (10), 1119-1125. DOI: 10.1136/jnnp-2012-304716 From NLM.
(196) Brady, S.; Healy, E. G.; Gang, Q.; Parton, M.; Quinlivan, R.; Jacob, S.; Curtis, E.; Al-Sarraj, S.; Sewry, C. A.; Hanna, M. G.; et al. Tubular Aggregates and Cylindrical Spirals Have Distinct Immunohistochemical Signatures. *J Neuropathol Exp Neurol* **2016**, *75* (12), 1171-1178. DOI: 10.1093/jnen/nlw096 From NLM.
(197) Schiaffino, S.; Severin, E.; Cantini, M.; Sartore, S. Tubular aggregates induced by anoxia in isolated rat skeletal muscle. *Lab Invest* **1977**, *37* (3), 223-228. From NLM.
(198) Mauro, A. Satellite cell of skeletal muscle fibers. *The Journal of biophysical and biochemical cytology* **1961**, *9* (2), 493.
(199) Zammit, P. S.; Beauchamp, J. R. The skeletal muscle satellite cell: stem cell or son of stem cell? *Differentiation* **2001**, *68* (4-5), 193-204.
(200) Seale, P.; Sabourin, L. A.; Girgis-Gabardo, A.; Mansouri, A.; Gruss, P.; Rudnicki, M. A. Pax7 is required for the specification of myogenic satellite cells. *Cell* **2000**, *102* (6), 777-786.
(201) Zammit, P. S.; Heslop, L.; Hudon, V.; Rosenblatt, J. D.; Tajbakhsh, S.; Buckingham, M. E.; Beauchamp, J. R.; Partridge, T. A. Kinetics of myoblast proliferation show that resident satellite cells are competent to fully regenerate skeletal muscle fibers. *Experimental cell research* **2002**, *281* (1), 39-49.
(202) Zammit, P. S.; Relaix, F.; Nagata, Y.; Ruiz, A. P.; Collins, C. A.; Partridge, T. A.; Beauchamp, J. R. Pax7 and myogenic progression in skeletal muscle satellite cells. *Journal of cell science* **2006**, *119* (9), 1824-1832.
(203) Mann, C. J.; Perdiguero, E.; Kharraz, Y.; Aguilar, S.; Pessina, P.; Serrano, A. L.; Muñoz-Cánoves, P. Aberrant repair and fibrosis development in skeletal muscle. *Skeletal muscle* **2011**, *1*, 1-20.

(204) Tidball, J. G. Regulation of muscle growth and regeneration by the immune system. *Nature Reviews Immunology* **2017**, *17* (3), 165-178.
(205) Griffin, C. A.; Apponi, L. H.; Long, K. K.; Pavlath, G. K. Chemokine expression and control of muscle cell migration during myogenesis. *Journal of cell science* **2010**, *123* (18), 3052-3060.
(206) Hogan, K. A.; Cho, D. S.; Arneson, P. C.; Samani, A.; Palines, P.; Yang, Y.; Doles, J. D. Tumor-derived cytokines impair myogenesis and alter the skeletal muscle immune microenvironment. *Cytokine* **2018**, *107*, 9-17.
(207) Andre, A. B.; Rees, K. P.; O'Connor, S.; Severson, G. W.; Newbern, J. M.; Wilson-Rawls, J.; Plaisier, C. L.; Rawls, A. Single cell analysis reveals satellite cell heterogeneity for proinflammatory chemokine expression. *Frontiers in Cell and Developmental Biology* **2023**, *11*, 1084068.
(208) Coumans, F. A.; Brisson, A. R.; Buzas, E. I.; Dignat-George, F.; Drees, E. E.; El-Andaloussi, S.; Emanueli, C.; Gasecka, A.; Hendrix, A.; Hill, A. F. Methodological guidelines to study extracellular vesicles. *Circulation research* **2017**, *120* (10), 1632-1648.
(209) Cocucci, E.; Meldolesi, J. Ectosomes and exosomes: shedding the confusion between extracellular vesicles. *Trends in cell biology* **2015**, *25* (6), 364-372.
(210) Van Niel, G.; d'Angelo, G.; Raposo, G. Shedding light on the cell biology of extracellular vesicles. *Nature reviews Molecular cell biology* **2018**, *19* (4), 213-228.
(211) Xiong, M.; Zhang, Q.; Hu, W.; Zhao, C.; Lv, W.; Yi, Y.; Wu, Y.; Wu, M. Exosomes from adipose-derived stem cells: the emerging roles and applications in tissue regeneration of plastic and cosmetic surgery. *Frontiers in Cell and Developmental Biology* **2020**, *8*, 574223.
(212) Figliolini, F.; Ranghino, A.; Grange, C.; Cedrino, M.; Tapparo, M.; Cavallari, C.; Rossi, A.; Togliatto, G.; Femminò, S.; Gugliuzza, M. V. Extracellular vesicles from adipose stem cells prevent muscle damage and inflammation in a mouse model of hind limb ischemia: role of neuregulin-1. *Arteriosclerosis, Thrombosis, and Vascular Biology* **2020**, *40* (1), 239-254.